

# Fibre laser based broadband THz imaging systems

**Eichhorn, Finn**

*Publication date:*
2010

*Document Version*
Publisher's PDF, also known as Version of record

# Fiber laser based broadband THz imaging systems

**Finn Eichhorn**

**Ph.D. Thesis**

**October 31, 2009**

**Technical University of Denmark**
**DTU Fotonik, Department of Photonics Engineering**

***Supervisors:***
**Professor Peter Uhd Jepsen, DTU Fotonik**
**Dr. Jens Engholm Pedersen, NKT Photonics A/S, Denmark**

# Abstract

The aim of this thesis is to investigate how state-of-the-art optical fiber technology can contribute towards multi-element broadband terahertz imaging systems. Classical table-top terahertz imaging systems are generally limited to a single emitter/receiver pair, which basically constrains the application to raster scanning imaging techniques. This thesis will exhibit that fiber technology can improve the robustness and the flexibility of terahertz imaging systems both by the application of fiber-optic light sources and by optical fibers as distribution medium for multi-element systems.

A two-color, polarization-maintaining distributed feedback fiber laser system for continuous wave terahertz generation by photomixing is presented. The laser system generates output powers up to several hundred mW, has 25 kHz linewidth and a polarization extinction ratio of better than 20 dB. The narrow linewidth and a simple amplification scheme makes this laser interesting for spectroscopic detection of narrow absorption linewidths and in multi-element emitter/detector arrays, respectively.

We further present the use of a fiber-coupled multi-element terahertz time-domain spectroscopy system to measure the scattering of terahertz radiation from films of multi-walled carbon nanotubes. The fiber-coupled multi-element spectrocopy system enables measurements only possible under time consuming realignment procedures with a classical terahertz time-domain spectroscopy system.

The status of the research and the development of an active multichannel terahertz imaging system, named the 'THz camera', is also presented in the scope of this thesis. This multi-element imaging system makes use of

a femtosecond fiber laser, a novel fiber-based sub-100 fs pulse distribution link with incorporated all-fiber dispersion control and a total of 64 ultra compact terahertz emitter and receiver heads.

# Resumé

**Dansk titel: Fiberlaser baserede bredbåndede THz billeddannelsessystemer**

Formålet med denne afhandling er at undersøge, hvordan state-of-the-art optisk fiber-teknologi kan bidrage til multi-element bredbånds Terahertz billeddannelse systemer. Klassiske table-top Terahertz billeddannelsessystemer er generelt begrænset til et enkelt sender / modtager-par, som begrænser anvendelsen til tidskrævende raster scanning billeddannelseteknikker. Denne afhandling viser, at fiber teknologi kan forbedre robustheden og fleksibiliteten i Terahertz billeddannelse, både ved anvendelse af fiberoptiske lyskilder og optiske fibre som distribution medium.

Et to-farvet, polariserings-vedligeholdende distribueret feedback fiber laser system til kontinuert bølge Terahertz generation ved photomixing præsenteres. Lasersystemet genererer output effekter op til flere hundrede mW, har 25 kHz liniebredde og et polariseringsforhold bedre end 20 dB. Den smalle liniebredde og et simpelt scalerbart forstærkningskoncept gør denne laser interessant for hhv. spektroskopisk påvisning af smalle Terahertz absorptions liniebredder og multi-element emitter / detektorsystemer.

Vi præsenterer yderligere brugen af et fiber-koblet multi-element Terahertz tidsdomæne spektroskopisystem til at måle spredningen af terahertzstråling fra film af multi-walled kulstofnanorør.

Desuden præsenteres forskningen og udviklingen af et aktivt multikanals Terahertz billeddannelsessystem, navngivet 'THz-kamera'. Dette multi-element billeddannelsessystem gør brug af en femtosekund fiber laser,

et fiberbaseret ultrakort puls distribution link med indbygget fiber dispersionskontrol og i alt 64 ultra kompakte Terahertz sender og modtager hoveder.

# Contents

# Preface

This Ph.D thesis is the summary of the work conducted during my employment as Ph.D. scholar at the Technical University of Denmark in the period August 2006 until October 2009. During this period I spend 4 months at the Wright State University, Dayton, OH, USA visiting Dr. Jason Deibel´s Terahertz and Ultrafast Photonics Research Group.

The thesis is organized in the following way:

- Chapter 1 will introduce to terahertz (THz) radiation and the utilization of THz waves for imaging.
- Chapter 2 contains the work on a dual-color DFB fiber laser which can be seen as a promising candidate as laser source for CW THz generation and detection. The laser source has exciting features for the use in multi-element imaging arrays due to its scalability. The work was done in close collaboration with the fiber laser company Koheras A/S, Denmark (now NKT Photonics). This work resulted in numerous conference contributions.
- Chapter 3 is a theory chapter introducing the basic concepts of pulsed THz sources, detectors, spectrometers and imaging techniques to introduce the theory and the challenges of the work presented in chapter 4 & 5.
- The work presented in chapter 4 is mainly on the scattering of carbon nanotubes and has been conducted during the stay in Dr. Deibel´s

group at Wright State University. The samples carbon nanotube samples under investigation are provided by Dr. Krzysztof K.K. Koziol from the Department of Materials Science and Metallurgy, University of Cambridge, UK. The work resulted until today in two conference publications, one NSF grant application and one newly started ph.d. project.

- The work presented in chapter 5 has been conducted as part of an large European Space Agency (ESA) initiated project, ESA Contract No. 21155/07/NL/ST, "Terahertz Camera for Remote Detection of Material Defects and Biological and Chemical Substances". The part of the project presented here is work done at DTU Fotonik and represents the status of the project at the time the author is writing this thesis. The project extend the period of the ph.d. work presented here. The project work was documented in numerous ESA-internal reports and presentations and for the time being 1 conference contribution and one submitted journal paper.

This Ph.D. fellowship was financed by a scholarship in the regime of the Photonics Academy Denmark and sponsored in equal parts by NKT Photonics A/S, the Technical University of Denmark and the Danish Ministry of Science, Technology and Innovation. A major source for financing equipment used for the work presented in chapter 5 was the ESA Contract No. 21155/07/NL/ST. I would also like to express my gratitude to OFS Fitel Denmark ApS for supplying us with the DCF fiber modules.

A publication list is included in Appendix A.

Kongens Lyngby,
October 31st, 2009

Finn Eichhorn

# Chapter 1

# Terahertz radiation & imaging

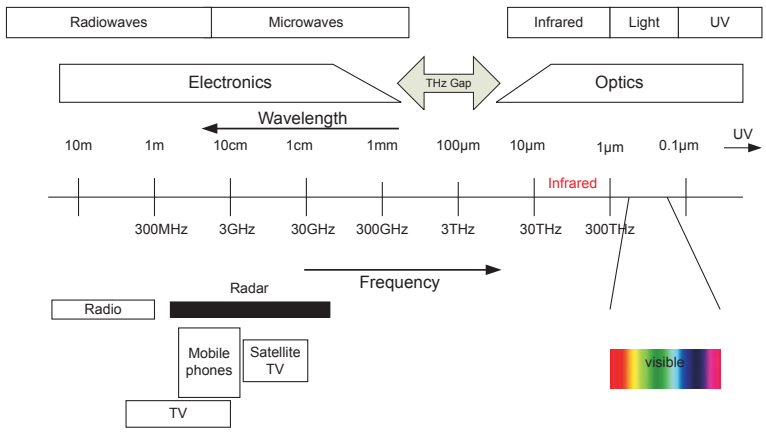


Figure 1.1: The electromagnetic spectrum from RF to UV

The word *imaging* can basically be defined as a visualization or reproduction of an object's form from the outside of the object itself. An

image can be acquired using many different techniques, but common for all techniques is the detection of electromagnetic radiation reflected from or emitted by the object. Optical imaging techniques use visible, ultraviolet or infrared light but imaging can as well be using by X-rays, microwaves and radio-waves, thus all builds on the same physical phenomena. Changing the wavelength of the detected radiation will change the way *we will see things*. A medium can be described by its physical properties like volume and mass etc., but also by its interaction with or radiation off electromagnetic radiation. Matter has different properties dependent on the wavelength we are looking at like opacity, density, absorption, conductivity, dispersion etc.

The modern human is today surrounded by imaging technologies which can be found everywhere in all our everyday lives. High definition television, computer screens and high resolution digital cameras employing the Nobel prize honored CCD technology are everywhere. Radar images are determining the weather forecast while X-ray, magnetic resonance and ultrasound imaging are vital tools in clinical imaging for medical doctors.

This thesis will address components, sources, detectors and propose a multi-element array imaging system working in the terahertz frequency range. The terahertz-region is the designation for the part of the electromagnetic spectrum which loosely is defined as the frequency range from 300 GHz to 30 THz. The terahertz range has previously often been viewed as the most scientifically useful yet least explored region of the electromagnetic spectrum. From a scientific viewpoint THz waves are very interesting because they for instance directly interact with charge carriers in semiconductors, phonon modes in crystals and intermolecular bonds in biological material. Further have THz waves the very interesting feature that although they 'behave' like light waves and they can penetrate for instance clothing, packing materials etc. which make the terahertz region extremely interesting also for non-scientific application.

Over the last two decades the terahertz-region has been explored intensively and the field has transformed into an very active research area. Many new research groups with background from various different scientific fields have moved into the field and this is resulted in an exponential growth of scientific publications over the last years. This has led to a vast of new tech-

niques for generation and detection of THz radiation and even more new applications areas as for instance advanced imaging techniques. All of this is helping rapidly in the exploration of the 'THz Gap' and to finally close it.

Various units are used to describe electromagnetic radiation dependent on the scientific community. The frequency of 1 THz corresponds to

$$1 \text{ THz} \sim 1 \cdot 10^{12} \text{ Hz} \sim 300 \ \mu\text{m} \sim 33.3 \text{ cm}^{-1} \sim 4.14 \text{ meV} \sim 47.6 \text{ K}.$$

### THz sources

The list of sources emitting THz radiation is during the recent years grown quite long, starting with the expensive and bulky devices making use of undulated electron beams like synchrotrons [1, 2], free-electron lasers[3, 4] and backward-wave oscillators[5].

THz emitters can also be realized using microwave technology based on Gunn [6], Impatt[7] or resonant tunneling diodes[8]. The fundamental emission frequency in these electronics devices is multiplied in specially designed mixer stages to access the frequencies in the lower THz region. The highest output frequency and the average output power has over the last years increased substantially, though is the technology still struggling with low conversion efficiencies by going towards higher and higher frequencies, especially for frequencies above 1 THz. Electronic-based THz sources can be very compact, but also relative costly due the highly specialized and miniaturized mechanical and electronic design.

Another source for THz radiation are molecular gas lasers, which rely on transitions between different rotational levels of molecular species. These lasers offer output powers of several mW but have only discrete wavelengths depending on the gas (e.g., 118.83 mm for a $CO_2$ pumped $CH_3OH$ laser)[9]. These laser are pumped with a carbon dioxide laser system which makes the whole system very complex and cumbersome to operate.

Direct optoelectronic-based THz sources can be more compact and the quantum cascade lasers (QCLs) are a very promising candidate with this respect. These devices rely on emission from a transition between the

subbands in a quantum well semiconductor structure. QCL's were in the beginning designed for emission in the mid-infrared, but the fields focus moved towards the far-infrared and THz region, where Tredicucci *et al.* in 2002 presented a QCL working at 4.4 THz[10]. Since then the lowest possible operation frequency moved closer towards 1 THz [11], but the technique is still requiring operation at cryogenic temperatures.

The next two indirect optoelectronic THz sources working at room temperature will be addressed the main focus in this text.

The first technique is maybe one of the most prominent in the THz community and relies on the advent of a modelocked Ti:sapphire laser was making its way into the optical laboratories in the early 1990. This technique uses various schemes were femtosecond laser pulses generate and detect THz pulses via an optical gating technique. For generation the most used techniques are the photoconductive antennas and the optical rectification scheme.

THz sources based on traditional Ti:sapphire femtosecond lasers are still bulky but price reductions and the upcoming of the femtosecond fiber lasers and ultra compact Ti:sapphire laser make this technique very attractive. This, combined with the possibility to control the dispersion of ultra-short pulsed in optical fibers which allows to couple the femtosecond pulse train directly to special designed THz sensor heads, pushed the technology towards a compact table-top or even handheld THz emitter. The principles of the photoconductive antennas will be described in detail in chapter 3.

The second technique is the photomixer THz generation scheme which is a cost effective alternative to the pulsed femtosecond laser system based setup. The femtosecond laser is here replaced by two single-mode single frequency lasers with a slightly different emission frequency. The emission of the two lasers is superimposed onto a semiconductor antenna resulting in a beat signal which is converted into an oscillating current in the antenna. The oscillating current is then source for a monocromatic THz wave radiating from the antenna. This technique is addressed in chapter 2.

## THz detectors

Coherent optoelectronic techniques like the photoconductive antennas are capable of detecting both continuous wave and pulsed THz radiation and are addressed in greater detail in chapter 2 and 3. Another popular coherent detection technique is the electro-optic detector. Here the THz pulse induces a birefringence in a crystal which is read out by the linearly polarized laser pulse.

Thermal detectors generally detect THz radiation in an radiation absorber attached to a heat sink. The radiation energy is absorbed and converted into heat. A very sensitive thermometer then measures the increase in heat induced by the radiation. The difference between various schemes of thermal detector is in the way the heat sink and the thermometer works. Compared to the techniques above are thermal detector only detecting the intensity of the THz radiation loosing the phase information of the detected signal which is extremely valuable in spectroscopic application.

Electronic detectors like hot electron bolometers (HEB) [12] and superconducting SIS mixers [13] have been proven to be very robust and reliable. These have been used in radiometers and in instruments both on ESA and NASA initiated space missions like Spitzer, Herschel, Planck and can basically cover the whole THz range. The downside of these detectors is the cryogenic working temperature and that the phase information of the detected signal is lost.

## Introduction to THz imaging

Imaging with electromagnetic radiation in the THz range has been addressed an increasing amount of attention during the last two decades. THz imaging systems have a vast range of potential application areas such as in security screening, medical diagnostics and non-destructive testing. THz waves can easily propagate through most nonpolar, nonmetallic materials such as common packaging material, corrugated cardboard, clothing, shoes and plastic bags. Numerous materials of interest for security or sensing applications such as explosives and chemical and biological agents provide

spectroscopic information about the materials and can potentially be identified by their spectral finger print in the THz range. The prospective to combine these two characteristic features of the THz technology in a THz imaging device offers an enormous amount of potential application areas and makes the area an extremely interesting for transferring well established laboratory experiments into real world industrial applications.

Imaging in the terahertz range using optoelectronic techniques has been approached by different techniques, mostly borrowed from other well established fields like X-ray, computer tomography (CT) or synthetic aperture radar. Optical terahertz imaging systems have predominantly been employing time-of-flight measurements by raster scanning the imaging object. Recently, also more advanced proposals for terahertz CT [14–16], synthetic aperture [17–19] and interferometric imaging [19] methods have been approached by several groups and published both in the scientific literature and filed as patents. Extensive work has also been done in the field of near-field imaging [20, 21] going beyond the wavelength limited resolution of the other techniques. A comprehensive review of the imaging with THz radiation has recently been published in [22].

Imaging techniques from time-of-flight measurements involves typically only one single transmitter and receiver, both at a fixed location. By having more than one transmitter and/or receiver at a multiple of different positions enables the illumination of the object from more than one location or to detect the scattered field at multiple locations. This is the basic idea behind tomography measurements. In practice, until today most proposed techniques only make use of one transmitter-receiver pair by moving the transmitter and/or receiver around the imaging object, acquiring data from various positions and subsequently reconstructing an image out of the data. The advent of the fiber coupled photoconductive emitters/receivers made this a viable method, since it then was possible to move the sensor heads around the object without loosing the optical alignment and delay of the THz setup [23–25]. This thesis will among other also contribute to the demonstration of one possible implementation of a multi channel imaging system using fiber coupled sensor heads (chapter 5).

Several research groups have explored the analogy of X-ray CT with

terahertz radiation. The work on THz CT was pioneered by Zhang and co-workers [14]. In contrast to X-ray CT terahertz CT resolves both the amplitude and the phase information of the scattering object. As a consequence the THz CT image contains more information than the X-ray CT about the target such as the frequency resolved refractive index. The wide-aperture reflection tomography allows the tomographic reconstruction of a series of slices measured at different view angles [16]. This technique works best with strong reflectors such as metals since it is a reflection setup. The algorithms used for the reconstruction of the images are in general filtered back-projection algorithms.

Active THz imaging can basically be done either by pulsed THz time-domain measurements or by continuous wave (CW) terahertz measurements. These techniques are compared in [26]. The first imaging system was based on pulsed THz time-domain measurements presented by Nuss *et al.* [27]. Pulsed THz imaging systems are based on generation and detection of single-cycle pulses by excitation of photoconductive antennas with femtosecond laser pulses [28]. Cost, size, and complexity of the femtosecond laser system has so far limited the spread of this otherwise very versatile technology.

This thesis will limit itself to only consider active imaging systems although commercial passive imaging systems detecting the black body radiation emitted from an object are available today.

# Chapter 2

# Novel fiber laser source for continuous wave THz imaging systems

The following chapter will present a novel fiber laser based optical source with potential use in generation and detection schemes of continuous wave (CW) terahertz radiation. Optically driven CW THz systems can offer a compact and inexpensive alternative to pulsed THz systems. One can for instance imagine specialized sensing, non-destructive testing or imaging applications where the identification of a single or a few well defined narrow absorption lines in the THz spectrum combined with the possibility of scanning these single lines can give sufficient information compared to the broadband pulsed THz system which still is based on rather expensive pulsed femtosecond solid state or fiber lasers. Although the price tag of pulsed laser systems has been reduced dramatically over the recent years, has CW THz system eventually a large potential to be the mass produced, ultra-compact and robust handheld or tabletop system of the future at a more affordable price than the pulsed laser systems.

The developed laser source consists of two by approximately 1 THz detuned unlocked distributed feedback (DFB) fiber laser oscillators and a

number of cascaded fiber amplifier stages. The novel feature of this source is a narrow and ultra-stable laser linewidth and the possibility of scaling the laser output with respect to output power. Further is the output wavelength of the laser oscillator tuneable without mode-hopping over several THz. The wavelength of the two fiber laser oscillators used in the following is around 1048 nm, making use of the rare-earth dopant Ytterbium (Yb) as gain medium. By combining the output of two oscillators followed by an amplification stage, we developed a two-color laser source for the use with CW THz generation and detection principles by photomixing, a heterodyne downconversion technique.

Employing laser sources above 800 nm brings up the need for direct bandgap photoconductive material with a bandgap smaller than the traditional photoconducting materials used in the field like Gallium Arsenide (GaAs) and Silicon-on-Sapphire (SOS). At the point in time where this two-color laser was developed no such material was available in our labs and thus does this chapter concentrates on the development and characterization of the laser source only.

The distinct features of a fiber laser source at 1048 nm, like simple optical amplification schemes and fiber distribution via optical splitters, opens up for the possibility of employing the laser in a multi-element CW THz imaging array with possible tunability over the THz frequency range. The inherent narrow linewidth (<25 kHz) of our DFB fiber laser also opens up for the detection of very narrow spectral absorbtion lines, as required for instance for gas sensing. The tuneability was shown to be around 1 THz in difference frequency, enabling broadband scans with extremely narrow linewidth.

## 2.1 CW THz generation by photomixing

Photomixing of two CW laser beams is an alternative to the pulsed THz generation and detection concept without giving up the advantages of the coherent detection scheme, e.g. the capability to measure both amplitude and phase of the THz signal. CW semiconductor and fiber lasers are much

more compact and inexpensive than Ti:Sapphire femtosecond lasers which still are the heart of the majority of THz systems. CW lasers offers high average output power, stable mono-mode operation, a variety of choices in laser wavelength and linewidths. CW THz generation and detection by the mixing of two semiconductor diode laser has been demonstrated in [29, 30] and the first implementation of a coherent all-optical THz measurement system was demonstrated in 1998 by Verghese *et al.* [31] who employed the optical beat signal from two CW Ti:sapphire lasers operating at different wavelength to generate and detect the THz signal using photoconductive antennas of low-temperature grown GaAs.

The first CW THz image was demonstrated by Kleine-Ostmann *et al.* [32] and based on a external cavity coupled laser diode (ETACAL) as two-color light source and was using a bolometer as detector. The first opto-electronic coherent homodyne CW THz imaging system has though been demonstrated by Siebert *et al.* in 2002 showing a THz image of a biological sample using photoconductive switches at 1 THz with a SNR of 1:100 and a diffraction limited resolution [33].

An approach using photomixer technology compatible with common fiber-optic wavelength by using a low temperature grown InGaAs (LT-InGaAs) for both emitter and coherent homodyne detector was first presented by Baker *et al.*[34]. They proposed the use of LT-InGaAs for wavelengths longer than 1 $\mu$m. The performance of the LT-InGaAs photomixer was though suffering from a higher dark current compared to LT-GaAs photomixers. A high dark current is problematic for both THz emitters and THz detectors. In the emitter the dark current results in additional heating due to a background current that constantly flows when a bias voltage is applied to the antenna. In the THz detector the dark current results in additional noise.

Very recently a group from the Fraunhofer Heinrich Hertz Institute (HHI) presented a fiberbased coherent CW system operating at 1.5 $\mu$m that employed photoconductive antennas based on a LT-InGaAs/InAlAs multilayer structure that addressed the high dark conductivity issues of LT-InGaAs by inserting multilayers of InAlAs to capture residual electrons resulting in an improved resistivity [35].

## Generation

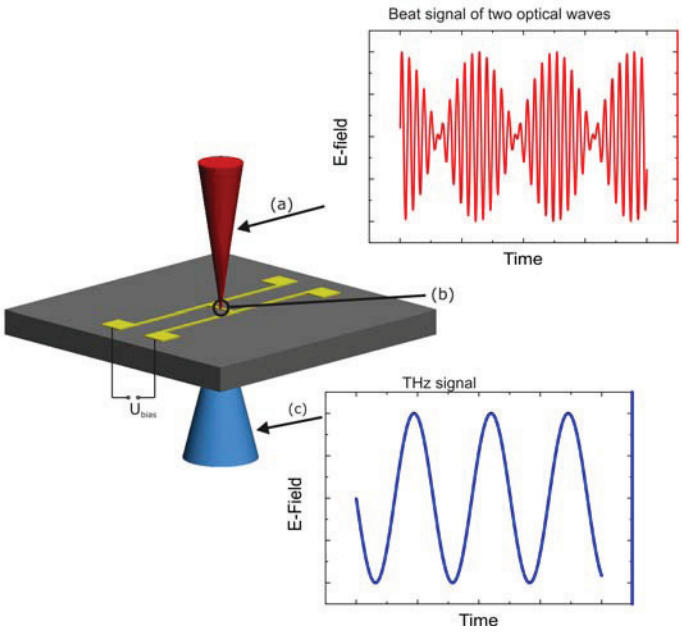


Figure 2.1: CW THz emitter with H-structure dipole metal structure on a semiconductor substrate. THz radiation is generated by photomixing of two slightly detuned laser beams. (a) Beat signal of $\omega_1$ and $\omega_2$ with difference frequency of $\omega_{THz}$. (b) The generated photocurrent is proportional to the optical input power, $I_{ph} \propto P_{opt} \sin(\omega_{THz} t)$. (c) The radiated THz power is proportional to the photocurrent squared, $P_{THz} \propto I_{ph}^2$.

Photomixing means the periodic generation of carriers in a photoconductor by a modulated laser beam in an semiconductor (Fig. 2.1). The superposition of two, in frequency slightly detuned laser-beams, leads to a beat signal with the difference frequency ($\omega_{THz} = \omega_1 - \omega_2$). The modulated laser beam generates periodically electrons and holes in a photoconductive

gap. The carriers are then separated by an electric field applied to an antenna structure metalized onto the semiconductor surface. This is resulting in a THz-modulated time dependent current that is fed into an resonant or broadbanded antenna, which emits CW THz radiation [29, 30]. The basic equation for the THz output power from photomixing assuming the antenna is perfectly matched to the device can be written as (adapted from [36]):

$$P_{THz}(\omega_{THz}) = \tfrac{1}{2} I_{ph}^2 R_A \frac{1}{1 + (\frac{\omega_{THz}}{\omega_{RC}})^2} \cdot \frac{1}{1 + (\frac{\omega_{THz}}{\omega_{tr}})^2} \tag{2.1}$$

where $I_{ph}$ is the generated AC-photocurrent, $R_A$ the antenna-resistance, $\omega_{RC}$ the RC-frequency of the photomixer and $\omega_{tr}$ the transit-time-frequency of the carriers, depending of their drift-velocity and distance they have to travel to get to the contacts. The fundamental mechanism is that $P_{opt} \sim I_{photo}^2$, where in this ideal case no further harmonics are generated. If one of the two beating lasers is tunable, an ultra wide tunability in frequency can be obtained. An upper limitation on the tuning range is set by the $\omega_{RC}$ and $\omega_{tr}$ in equation 2.1. The generated time varying current is

$$I(t) = I_0[1 + \cos 2\pi\nu_{THz}t] \tag{2.2}$$

where $I_0 = \eta_{ph} q P_L/(h\nu_0)$. $P_L$ is the laser power and $\eta_{ph}$ is the fraction of the incident photons absorbed in the active region of the mixer. The generated THz-photocurrent I(t) in 2.2 can now provide the input signal to an antenna structure that can radiate the generated power.

### Detection

The generated THz signal is detected in the receiver by coherent homedyne detection. The THz induced photocurrent $I_{det}$ in the detector antenna is

$$I_{det} \propto P_{opt} E_{THz} cos\left(\frac{\omega_{THz}}{c}\Delta d\right) \tag{2.3}$$

where $P_{opt}$ is the optical power incident on the photodetector, $E_{THz}$ is the amplitude of the incident THz wave at a frequency of $\omega_{THz}$ and

$\Delta d$ the relative path length difference the emitter and detection arm. Fig. 2.2 shows a sketch of a typical experimental photomixing setup. The two-colored beam is slitted into two beam paths, one feeding the emitter photomixer and the other gating the detector photomixer. In the detector beam path a optical delay stage is used to change the path length difference between the two arms.

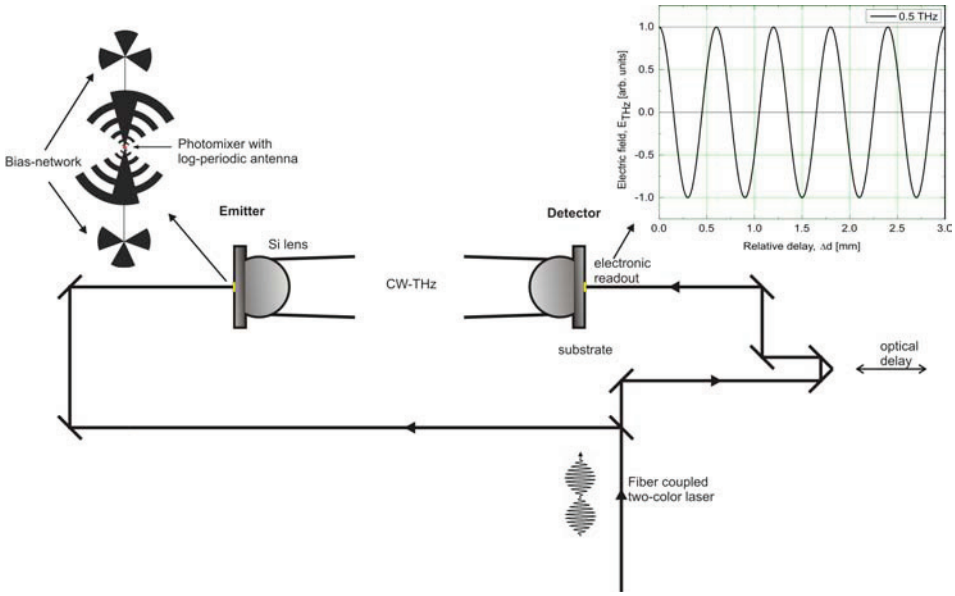


Figure 2.2: Sketch of a CW THz photomixing setup.

The homedyne DC output signal at the receiver can be detected in a lock-in amplifier referenced to a modulation of the emitter bias modulation. A time delay stage is used to change the path length between the emitter and detector arm, which introduces a phase delay between both the optical beat and the THz signal at the detector. Since the detected DC signal is maximized when both optical beat and THz signal arrive in-phase, one can now by changing the time delay map out an interferogram from which both THz amplitude and phase can be determined[31].

### Photoconductive mixers and photodiodes

Some of the first semiconductor based CW THz sources made use of the optical beating of two detuned laser pulses in photoconductive mixers [31].Photoconductive mixers consists typically of interdigitated-finger electrodes placed on semiconductor material with a short recombination lifetime as e.g. LT-GaAs or ErAs:GaAs [36, 37]. In the gaps between the fingers, seen on fig. 2.3, are carriers generated and afterwards separated by an applied electric field, which the structure is biased with.

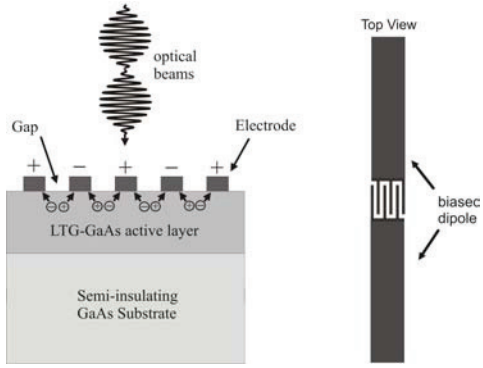


Figure 2.3: Sketch a LT-GaAs photomixer

The reason why the recombination lifetimes need to be short, is to ensure that photo-carrier generated in the previous period are recombined until the next period starts (0.2 – 1 ps). The devices have small distances of about 1 $\mu$m between the fingers [36], so the transit-time $\tau_{tr}$ will be in the area of 10 ps, when assuming the carriers are moving at their saturation drift velocity of $v_{sat} \approx 10^7$cm/s. The saturation drift velocity of $v_{sat} \approx 10^7$cm/s is reached when high electric fields are applied to the photoconductor. Another limitation factor is the recombination time $\tau_{rec}$ of the generated carriers since these have to arrive at the contacts before again recombining. Hence a trade-off between the transit time and the recom-

bination time exist where the frequency dependence of the device can be improved by reducing the recombination time or the transit time. This then in turn results in a reduced output power since not all generated carriers arrive at the contacts[36].

Thus the main limitation of the photoconductive antenna concept is on one hand the capacitive roll-off and the other the low photoconductive gain $g = \tau_{rec}/\tau_{tr}$. The photoconductive gain is given by the recombination lifetime $\tau_{rec}$ of the LT-GaAs and the transit-time $\tau_{tr}$ of the carriers until they reach the contacts.

Therefore are photomixers often based on interdigitated electrode structures on fast semiconductor material feeding either a broadband or resonant antenna. The output power of a ErAs:GaAs based photomixer has a best reported output power of 2 $\mu$ $W$ at 1 THz and 12 $\mu$W around 90 GHz with a two decade tunability[37].

One more successful approach reducing the intrinsic limitations of the conventional photomixer is the uni-traveling carrier (UTC) diode that utilizes only the faster electrons as the active carriers. The optical absorption and the electron transport regions are separated and can be optimized independently. This concept is one way to achieve higher output power at THz frequencies as the conventional photomixer. The device is still both transit-time and RC time limited and thus the output power also drops like for conventional photomixer with $\omega^{-4}$. However, maximum CW output powers of 20 mW and 10 $\mu$W have been achieved at 100 GHz and 1 THz, respectively, using UTC's operating at 1.55 $\mu$m[38].

## 2.2 DFB fiber lasers & fiber amplifiers

The following will give a short introduction to the employed DFB fiber lasers and introduce the most important components used for the two-color fiber laser system. The fiber laser consists of two main components the distributed feedback fiber laser oscillator and the fiber amplifier stage. Further does the systems include several standard polarization maintaining (PM) and non-polarization maintaining (non-PM) fiber components as splitters,

combiners and wavelength division multiplexers. These components are not addressed in detail to keep the focus of this text.

### Distributed feedback fiber lasers

The laser oscillators chosen for the two-color laser system is a single-mode distributed feedback (DFB) fiber laser from the fiber laser company Koheras A/S, Denmark. The fiber laser consists of a Bragg-grating UV-written into an actively doped piece of silica fiber (see Fig. 2.4). The periodic Bragg-grating structure in DFB fiber lasers acts as a resonator which works as a distributed reflector for the designed laser wavelength. The laser gain contained in the structure is achieved by using silica fiber doped with rare earth ions such as Erbium, Ytterbium Thulium, Neodymium etc. The oscillator has multiple axial resonator modes, but there is typically one mode which is favored in terms of losses. Typically, the periodic structure is made with a phase shift in its middle to ensure the single-mode operation. The more detailed fundamentals of DFB gratings generally and DFB fiber lasers specially can be found in refs. [39, 40] and [41–43], respectively.

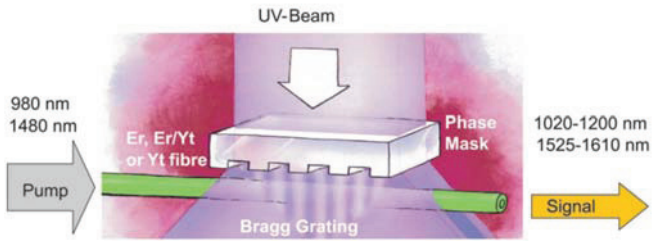


Figure 2.4: Distributed feedback fiber laser consisting of a Bragg grating UV written in actively doped fiber and pumped at 980 nm of 1480 nm. Courtesy of NKT Photonics A/S.

The linewidth of a DFB fiber laser can be as low as 10 kHz for a coherence length of 100 meters. Comparing this number to typical semiconductor DFB laser one can see a linewidth in the MHz range. Since

the linewidth typically scales with the laser cavity length (e.g. resonator bandwidth)[44] and the standard DFB fiber laser typically has a resonator length of around 50 mm they can obtain a superior linewidth compared to a DFB semiconductor lasers (hundreds of $\mu$m)[45]. Due to the basic principles of photomixing (section 2.1) the laser linewidth, the phase-noise and intensity noise directly do transfer into the linewidth of the CW THz signal. This feature is the origin of the ultra narrow linewidth of the laser.

Fig. 2.5 is showing a typical DFB fiber laser coupling. The fiber laser is pumped with 978 nm light from a fiber coupled single-mode laser diode. The fiber laser consists of an approx. 50 mm doped silica fiber (gain medium) and an UV-written distributed Bragg reflector defining the resonator. The typical output power of an in the following employed fiber laser is 12 mW at a oscillator wavelength of 1042.6 nm when pumping with 300 mW of 978 nm of pump power.

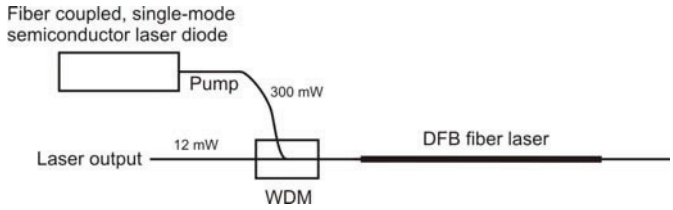


Figure 2.5: Sketch of fiber laser setup. The fiber laser is pumped with 978 nm light from a fiber coupled laser diode by using a WDM component. The fiber laser consists of an approx. 50 mm doped silica fiber (gain medium) and an UV written distributed Bragg reflector defining the resonator.

### Ytterbium-fiber amplifiers

Fiber amplifiers are optically based amplifiers with the optical fiber as gain medium. The gain medium is a silica fiber doped with rare earth ions such as Erbium, Ytterbium, Thulium, Neodymium etc. The dopants are pumped with light typically from a fiber coupled diode laser. The signal

to be amplified and the pump propagate together through the medium and the energy is transferred between the two [46].

The the invention of the Erbium-doped fiber amplifier with its major commercial application in the telecom industry was the breakthrough for the fields of rare earth doped fiber amplifiers, making a very large wavelength range easily accessible due to the number of available rare earth dopants. The EDFA work was pioneered by David N. Payne, R. Mears, and L. Reekie, from the University of Southampton [47] and a group from AT&T Bell Laboratories, E. Desurvire, P. Becker, and J. Simpson.[48]. A straight forward amplification scheme and the success in the telecom industry made that the EDFA not only stayed confined to the telecommunication industry but spurred a steadily growing interest in other areas.

Ytterbium-doped fiber amplifiers (YDFA´s) offers amplification over a large wavelength band from about 975 nm up to 1200 nm. Especially when pumping the YDFA with 975 nm, this will give access to the wavelength range between 1000 nm and 1150 nm with low amplified stimulated emission (ASE) and high gain. The Yb gain spectrum is depicted in Fig. 2.6. Ytterbium amplifiers can be made with extremely high output power (tens of kilowatts). This feature makes a CW THz source based on YDFA´s highly scalable with respect to output power and therefore very interesting as source in multi-element systems.

For single-frequency operation, stimulated Brillouin scattering (SBS) is the most important nonlinear phenomena which limits operation power and addressed later in this chapter.

Ytterbium-doped glass exhibits pronounced three-level characteristics for wavelengths below $\sim$ 1040 nm. For operation at such wavelengths, a large inversion density is required for overcoming the reabsorption loss. For longer wavelengths, as sometimes used in fiber lasers, there is hardly any reabsorption, and in a long fiber only a very low excitation density may be required to obtain sufficient gain.

Ytterbium gain spectrum can from the absorption and emission cross-section in Fig. 2.6 be written as:

$$G(\omega) = N_{\frac{5}{2}}\sigma_e(\omega) + N_{\frac{7}{2}}\sigma_a(\omega) \tag{2.4}$$

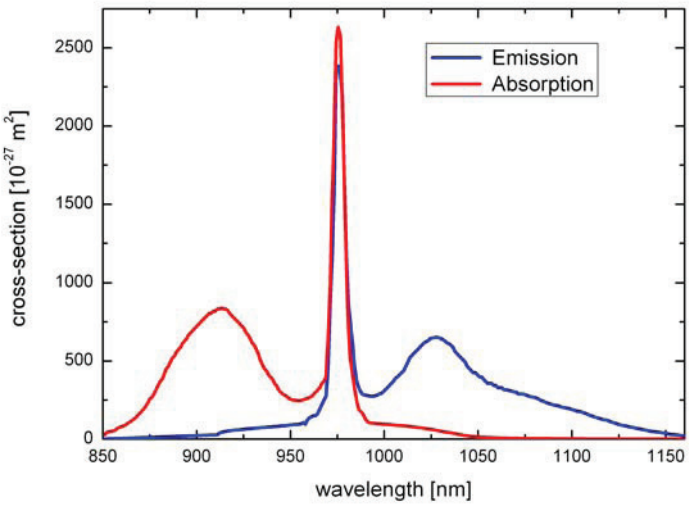


Figure 2.6: Absorption and emission cross section of Yb in germanosilicate glass. [49]

Where $\sigma_e$ is the emission cross-section, $\sigma_a$ the absorption cross-section and $N_{\frac{5}{2}} + N_{\frac{7}{2}} = N_{Yb}$.

A standard fiber amplifier setup is shown in Fig. 2.7. The amplifier includes an optical pump, typically a fiber-coupled single-mode semiconductor laser diode with output wavelength of 978 nm and an output power ranging up to 1 W. A fiber-based WDM component combines pump and signal wavelength before propagation into the Yb-doped fiber. The length of the doped fiber can vary in length dependent on the doping level and the pump power. To avoid damage of the diode laser end-facet due to back-reflections from the amplifier output typically an optical isolator is placed for protection.

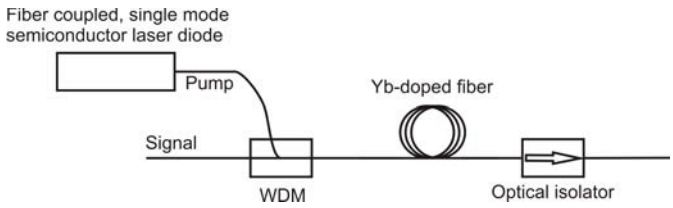


Figure 2.7: Sketch of a standard Ytterbium fiber amplifier setup. The amplifier is pumped by a fiber coupled diode laser. A WDM is combining pump and signal into the doped fiber. An optical isolator is placed to protect the laser from backreflections from the output.

## 2.3 Characteristics & results of two-color fiber laser

During the development process of the two-color fiber laser system several lasers were build varying e.g. the pump diodes and oscillator wavelength and finally we changed from a non-polarization maintaining (non-PM) to a fully polarization maintaining (PM) system.

The first approach did not include PM components due to the thought that fiber polarization controllers could tune the two initially different laser polarizations into the same polarization axis at the end of the laser source. The polarization of the two oscillators need to overlap to generate the beat signal at the photomixer. The non-PM version revealed stability issues introduced by heat, stress and vibration induced additional birefringence in the fiber resulting in a low polarization extinction ratio (PER) between the two oscillator wavelength. This resulted basically in the design of a completely new laser by shifting all the non-PM components to PM components.

### Non-polarization maintaining

Fig. 2.8 shows a sketch of the first two-color fiber laser system developed, which consists of two fiber lasers with an oscillation wavelength of 1042.3

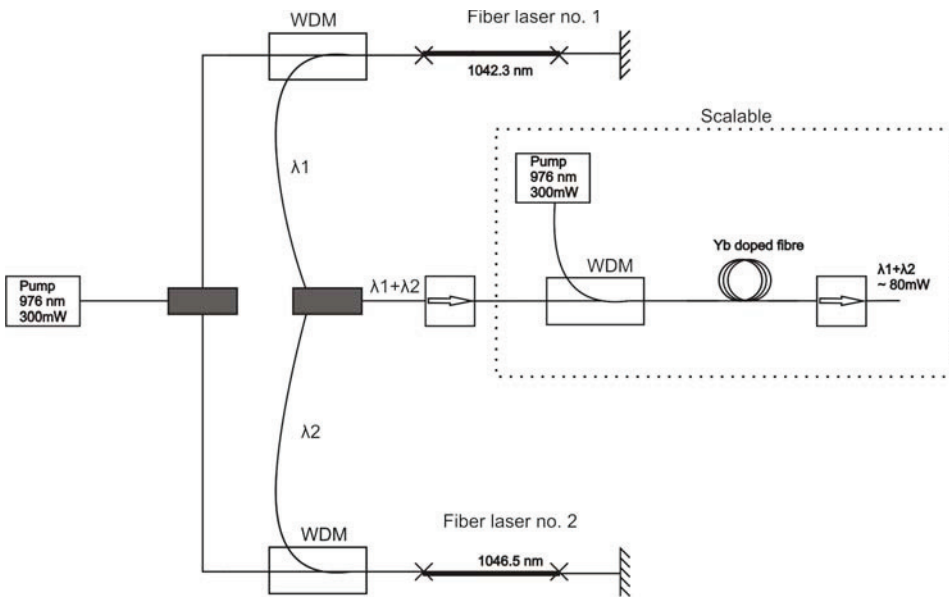


Figure 2.8: Sketch of the first principle of the two-color laser. The two oscillators are followed by an amplifier stage combining and amplifying the oscillator signal.

nm and 1046.5 nm, respectively. The two lasers share one single 976 nm, 300 mW pump diode. The signal from the two oscillators are combined in an fiber-optic combiner and amplified in a preamplifier stage consisting of 2 m of active Yb-doped fiber. The pre-amplifier is pumped with 300 mW. The output power is scalable in the sense that it is possible to further amplify the output signal in another or several cascaded amplifier stages. The output spectrum is measured with a optical spectrum analyzer and shown in Fig.2.9. The output power of the two combined oscillators amplified in the pre-amplifier is 80 mW, sufficient to drive several photoconductive antennas. The ASE noise floor is first seen at $> 50$ dB. The frequency spacing between the two oscillator wavelengths is around 4.2 nm or 1.15 THz.

Since the spectral resolution of the spectrum analyzer used to obtain

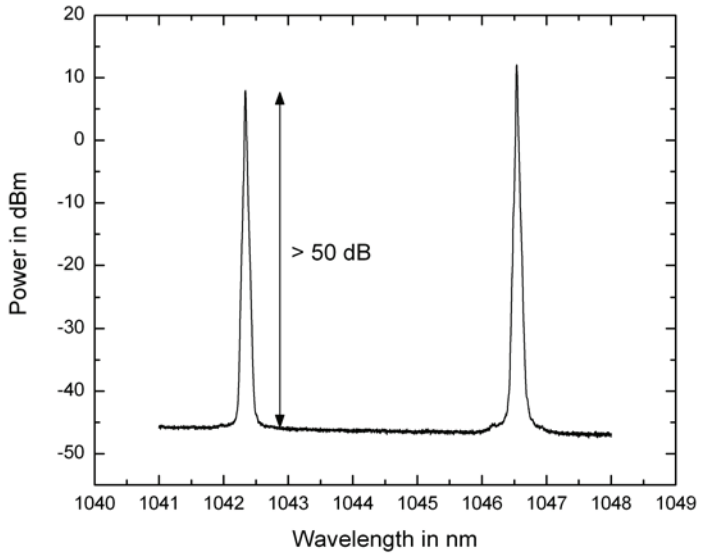


Figure 2.9: Output spectrum of two-color laser shown in Figure 2.8. The ASE noise floor is seen >50 dB. The unequal height of the peak in the spectrum is due to the Yb-gain spectrum (see Fig. 2.6).

the data in Fig. 2.9 is limited to 2 GHz and the linewidth of typical fiber lasers is in the kHz range, so we need to apply a self-heterodyne linewidth measurement technique [50, 51]. This measurement shows a linewidth of 24 kHz measured over 120 $\mu$s (Fig. 2.10).

The total output power at the output of the amplification stage shown in Figure 2.8 is currently 80 mW, limited by severe losses in the output isolator (we obtain more than 250 mW total power before the isolator). In Fig. 2.9 the power in the laser lines is not equally distributed, due to the gain profile in Yb-doped fiber and the off-center wavelength of the standard 1064-nm components used in this first version of the laser. The power distribution

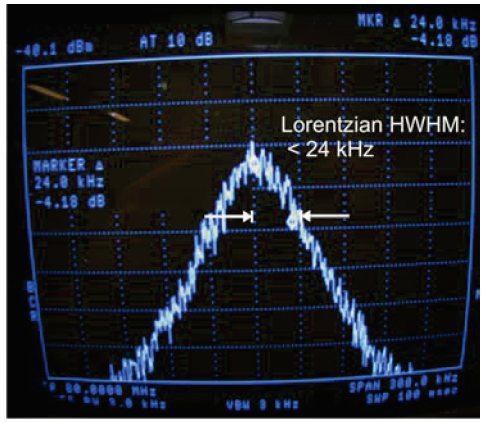


Figure 2.10: Self-heterodyne linewidth measurement, which shows a linewidth of the two-color laser of below 24 kHz.

between the two colors would be controllable by separate pumps on each DFB laser. This was then implemented in the next laser version.

The tunability of the laser system is illustrated in Fig. 2.11, where the laser cavities are mechanically stretched one at a time and hereby red shifted compared to their inherent relaxed oscillation wavelength. The difference frequency can easily be tuned over 1 THz by stretching the fibers. A more daring experiment should give a tuning range of more than 2 THz before reaching the elasticity limits of the fibers.

Considering the noise characteristics of the laser it can on Fig. 2.9 be seen that the ASE noise floor is suppressed by 55 dB. Furthermore a measurement of the relative intensity noise (RIN) using a HP Lightwave Analyzer gives a laser RIN of -151 dBc/Hz for frequencies above 10 MHz. The relative intensity noise describes amplitude fluctuations in the optical field and is caused by optical interference between the laser signal and spontaneous emission in the cavity. RIN is defined as

$$RIN = \frac{\Delta P^2}{P_{avg}^2} \tag{2.5}$$

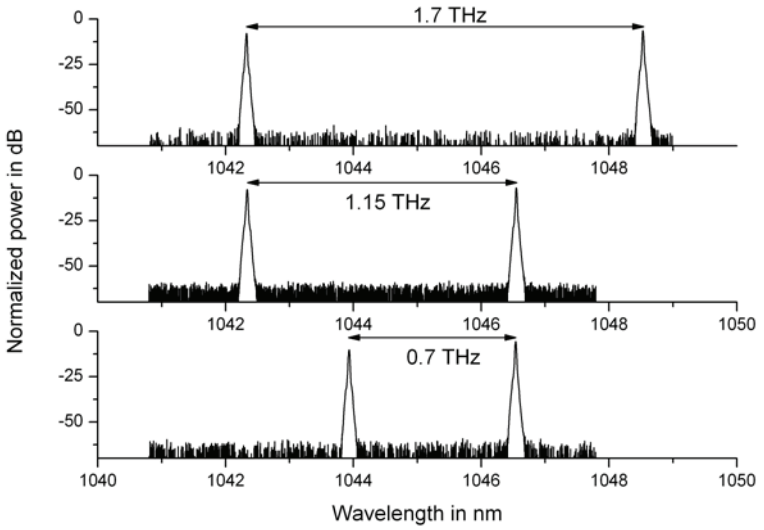


Figure 2.11: Wavelength tuning of the two-color laser by mechanically stretching of the laser cavities.

where $\Delta P^2$ is the mean square intensity fluctuation spectral density of the optical signal and $P_{avg}$ is the average output power. These two numbers show a good noise performance of the laser system compared to other high performance single frequency DFB fiber laser sources [52].

### Polarization maintaining laser

The laser in this section is build exclusively out of polarization maintaining fiber components and the fiber used is the polarization maintaining PANDA fiber, which is a fiber with high internal birefringence that can maintain linear polarization against external perturbations as e.g. bending and vibrations. Another novelty compared to the laser characterized in the previous section is that the oscillators are pumped individually to avoid

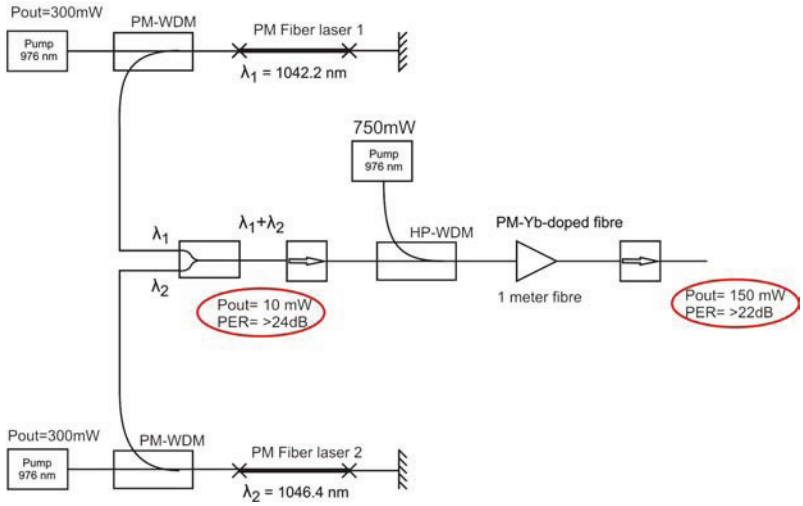


Figure 2.12: Sketch of a polarization maintaining two-color fiber laser setup with individual pumps for each oscillator followed by an Yb-doped fiber amplifier pumped with 750 mW.

unequal amplitudes of the two wavelengths originating from the Yb-gain spectrum. Furthermore the pump diode of the preamplifier is increased from 300 mW to 750 mW. Fig. 2.12 shows a sketch of the new version and the spectrum is found in Fig. 2.13. A measurement of the output spectrum vs. pump power is shown in Fig. 2.14. The output power of the PM laser is 150 mW and the polarization extinction ratio (PER) is measured with a PER meter to 22 dB.

Fig. 2.15 shows a measurement of the PER over 30 minutes. The improved PER stability resulted from the PM components used and this directly translated into an improved stability of the laser output. By insuring a stable overlap of the two laser polarizations throughout the entire laser system enables the laser to be employed as source for photomixing.

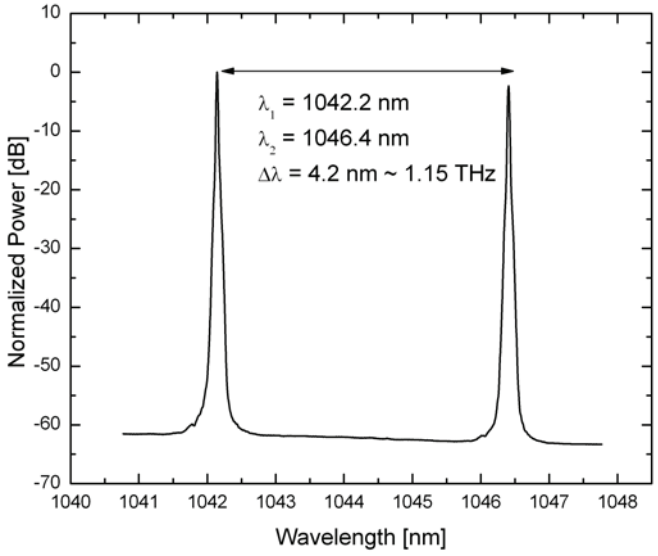


Figure 2.13: Power spectrum of an all polarization maintaining dual-color fiber laser version.

### High power multi-mode fiber amplifiers

Although the lasers showed in this chapter already had several hundreds of mW output power, even more output power going towards several Watt´s is achievable by using active large mode area (LMA) or photonic crystal fibers (PCF). Fig. 2.16 show an idea of a system configuration containing high power fiber amplifiers. The amplifier system employs an active LMA power combiner which is pumped with several multi-moded high power diode lasers. The signal path through the power combiner is kept in single-mode polarization maintaining fiber. Output power of several kW's have been shown recently for single wavelengths systems[53].

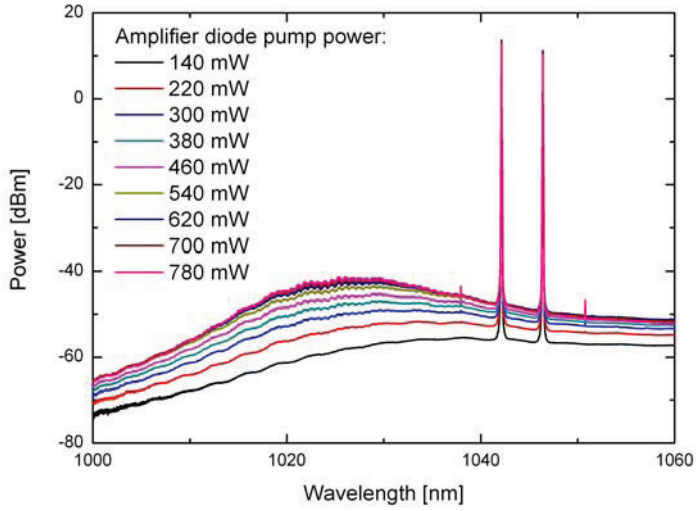


Figure 2.14: Figure depicts the enhancement of amplified stimulated emission(ASE) when increasing the pump power to the amplifier stage.

### Discussion of Brillouin scattering and Four-wave mixing

The output spectrum of the PM laser version (Fig. 2.12) is showing the advent of the $\chi^{(3)}$ nonlinearity four-wave mixing (FWM). FWM is a type of optical Kerr effect, and occurs when light of two or more different wavelengths are launched into a fiber. The the two narrow linewidths in the fiber laser give rise to degenerate FWM of the two wavelengths. In Fig. 2.17 one can clearly see the dependence of increased pump power. The frequency mixing components that are appearing in Fig. 2.17 are: $\lambda_3 = \lambda_1 + \lambda_1 - \lambda_2$ and $\lambda_4 = \lambda_2 + \lambda_2 - \lambda_1$. At full pump power (750 mW at 978 nm) are the FWM components still suppressed by 50 dB.

Another effect that can decrease the performance of a CW fiber laser substantially is stimulated Brillouin scattering [54]. This scattering effect

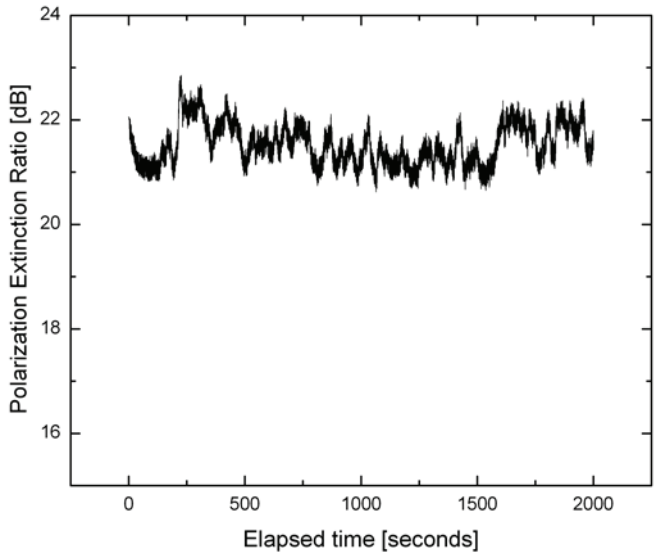


Figure 2.15: Measurement of the polarization extinction ratio over 30 minutes.

is a $\chi^{(3)}$ nonlinearity and related to the acoustic phonons in a medium. The incident photons can be converted into a scattered photons of slightly lower energy and the generated phonons are usually propagating in the backward direction. This can even at low optical power become a very strong effect. Above a certain threshold the stimulated Brillouin scattering can reflect most of the power of an incident beam. SBS can be seen when narrow-band optical signals (e.g. from a single-frequency laser) are amplified in a fiber amplifier, or just propagated through a passive fiber. While the material nonlinearity of e.g. silica is not very high, the typically small effective mode area and the long propagation length strongly enhances this nonlinear effect. Brillouin scattering in fibers is treated in ref. [55] and methods to

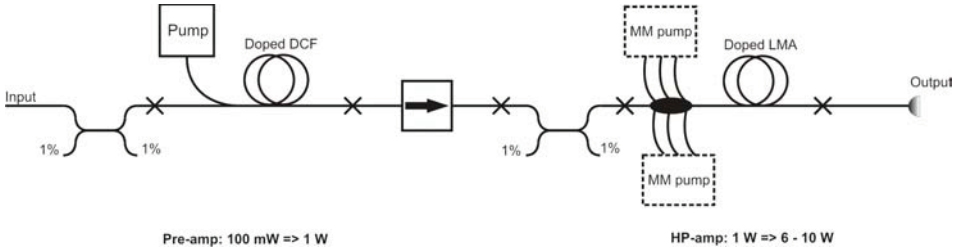


Figure 2.16: Fiber amplifier for high power amplification employing high power multimode pumps and active large mode area fiber. The LMA fiber amplifier can be pumped with several high power pump diodes.

suppress the SBS treshold to several hundred Watts are reported by Kovalev et al. in [56]. Measurements of the output spectrums of our laser systems above are not showing the event of Brillouin scattering despite the narrow linewidth and the amplification of the two colors laser setups.

## 2.4 Summary

This chapter shows results on a novel fiber laser system for CW THz generation. The laser system is tuneable over more than 1 THz, and the difference frequency has a linewidth of below 25 kHz. The system is fully scalable with respect to power and can be distributed along optical fibers to a multi-element array of THz emitters and detectors. The nonlinear effect from four-wave-mixing where suppressed 50 dB and no indications of SBS was observed.

### Future work

In the future this laser for THz generation and detection needs to be tested with an appropriate photomixing material. In chapter 5 we will describe a potential candidate for working around 1$\mu$m wavelength. Another possible material candidate for difference frequency generation at 1$\mu$m is the crys-

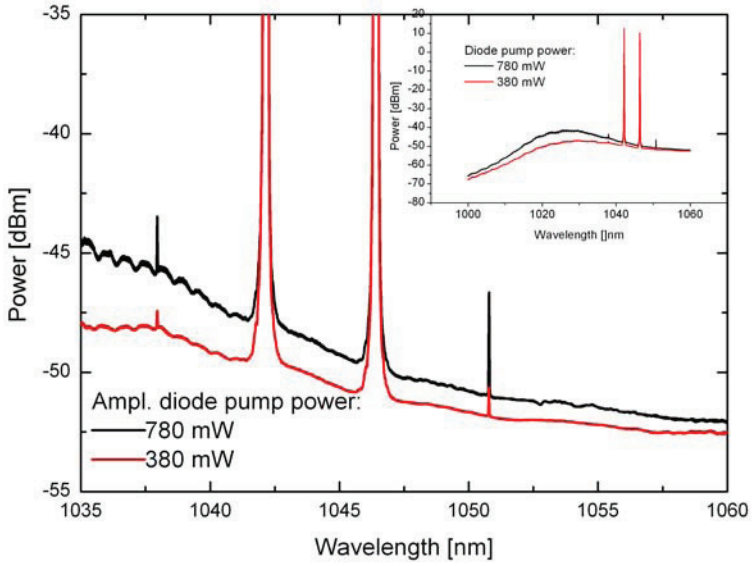


Figure 2.17: Power spectrum measurement and the appearance of four-wave-mixing components by increased pump power. The FWM components are still suppressed by more than 50 dB at a pump diode power of 750 mW.

talline salt diethylaminosulfurtetrafluoride (DAST) which possesses very high nonlinear susceptibilities and electro-optic coefficients [57–60].

At the time of writing this thesis we had photoconductive antennas based on LT InGaAs/InAlAs multi-layer structures from HHI Berlin available in the lab for testing. The HHI group very recently published their latest results on a CW THz photomixing source operated at 1.5 $\mu$m [35] using the LT InGaAs/InAlAs multi-layer structures as detector and a novel InP-based waveguide-integrated photodetector as emitter [61].

# Chapter 3

# Pulsed broadband terahertz imaging

This chapter will present the major photonic based terahertz generation and detection schemes used and review the concepts of the state-of-the-art THz imaging systems.

Generation and detection of a THz pulse generally occurs through the nonlinear interaction of a driving optical pulse with a material with a fast response.

One big class of generation and detection techniques makes use of the photoconductive switch. THz generation occurs in the photoconductive switch when an ultra fast optical excitation induces conductivity changes in a semiconductor. The process builds on a resonant interaction as absorbtion of photons through a interband transition. The photoconductive detection process relies also on conductivity changes in a gated antenna structure as the generation of THz pulses.

The second major class of THz emitters generates THz radiation by a non-resonant interaction of short optical transients with nonlinear medium like the ZnTe-crystal and employs the $\chi^2$-process of different frequency generation or optical rectification.

A widely used detection scheme also making use of a non-resonant interaction in a nonlinear medium, namely the electro-optic effect (or Pockels effect). The electro-optic effect changes the refractive index of a inversion asymmetric medium linearly proportional to the incoming electric field.

Both types generation and detection methods are employed in the reported THz imaging systems, though one needs to keep in mind that the optical rectification process requires much higher pulse energies than the photoconductive generation process. This results in larger requirements for the ultra-fast laser source.

## 3.1 Electromagnetic radiation

The following derivation will give the fundamental background for understanding the processes giving rise to THz radiation used in this work, namely the two source terms the first derivative of a conduction current, $\partial \vec{J}_{cond}/\partial t$ and the second derivative of a polarization, $\partial^2 \vec{P}/\partial t^2$.

Maxwell's equations can be used to completely describe the generation of electromagnetic radiation in a medium and are as follows:

$$\nabla \times \vec{E} + \frac{\partial \vec{B}}{\partial t} = 0 \tag{3.1}$$

$$\nabla \cdot \vec{B} = 0 \tag{3.2}$$

$$\nabla \times \vec{H} = \frac{\partial \vec{D}}{\partial t} + \vec{J} \tag{3.3}$$

$$\nabla \cdot \vec{D} = \rho \tag{3.4}$$

where $\vec{D} = \epsilon \vec{E}$, with $\epsilon$ being the dielectric constant, $\vec{B} = \mu \vec{H}$, with $\mu$ being the magnetic moment of the material, and $\vec{J}$ is the current density. Combining Eq. 3.1 with Eq. 3.4 using the vector identity $\nabla \times (\nabla \times \vec{A}) = -\nabla^2 \vec{A} + \nabla(\nabla \cdot \vec{A})$ gives

$$\frac{\partial}{\partial t}(\nabla \times \vec{B}) = \nabla^2 \vec{E} - \frac{1}{\epsilon}\nabla \rho \tag{3.5}$$

by combining this result with Ampère's law in equation 3.3, and by assuming that there are no free charges ($\rho$=0) this result in the wave equation

$$\nabla^2\vec{E} - \epsilon\mu\frac{\partial^2\vec{E}}{\partial t^2} = \mu\frac{\partial\vec{J}}{\partial t} \tag{3.6}$$

The right hand side of the wave equation is the fundamental source of radiation, more precisely the non-uniform motion of charge. By making a distinction between free and bound charges we can split the right hand side of equation 3.6 even further up. Since the current $\vec{J}$ in general consists of both conduction $\vec{J}_{cond}$ and bound $\vec{J}_{bound}$ contributions, with $\vec{J}_{bound} = \frac{\partial\vec{P}}{\partial t}$ we are finally arriving at the expression

$$\nabla^2\vec{E} - \epsilon\mu\frac{\partial^2\vec{E}}{\partial t^2} = \mu\left(\frac{\partial\vec{J}_{cond}}{\partial t} + \frac{\partial^2\vec{P}}{\partial t^2}\right) \tag{3.7}$$

which is recognized as a wave equation with two source terms, the first derivative of a conduction current, $\partial\vec{J}_{cond}/\partial t$ , and the second derivative of a polarization, $\partial^2\vec{P}/\partial t^2$. With derivation of the two source terms we have the fundamental background for the used THz generation techniques used in the following.

## 3.2 THz sources

### Photoconductive antennas

A photoconductive switch was one of the first methods generating pulsed THz radiation. This technique was pioneered by D. H. Auston [62] and further improved later in [63–68]. Today is the photoconductive antenna design (Fig. 3.1) making use of the basic principles of the first photoconductive switch and is one of the most used optoelectronic THz generation principles in terahertz-time-domain spectrometers (THz-TDS's). An optical femtosecond laser pulse is focussed into a small gap between two metallic striplines typically separated by $30 - 60$ $\mu$m and deposited on a direct-gap semiconductor material. An above bandgap laser excitation of the semiconductor is creating carriers which are accelerated by a DC-field applied

to the striplines. The resulting time-varying current burst is giving rise to a freely propagating sub-picosecond transient or THz pulse which in the far-field is given by $E \propto \partial\vec{J}/\partial t$.

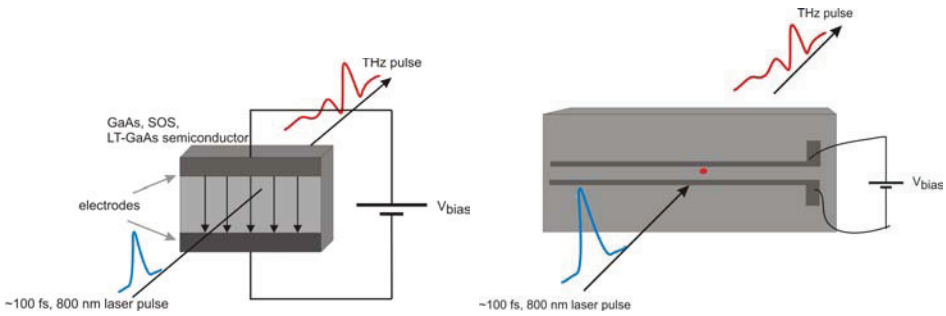


Figure 3.1: A biased photoconductive switch (left). Photoconductive antenna with biased photoconductive gap. The pulsed femtosecond laser pulse is focussed into the photoconductive gap(right).

In the simple model of a short dipole antenna the radiated electric field $E(r,t)$ in free space can be described for distance $r$ and the time $t$ as:

$$E(r,t) = \frac{l_e}{4\pi\epsilon_0 c^2 r}\frac{\partial J(t)}{\partial t} sin(\theta) \propto \frac{\partial J(t)}{\partial t}, \tag{3.8}$$

where $J(t)$ is the current in the dipole, $l_e$ the effective dipole length, $\epsilon_0$ the dielectric constant of free space, c the speed of light in vacuum and $\theta$ the angle of direction from the dipole. From equation 3.8 thus the strength of the radiated field is both proportional to the dipole length and the first derivative of the driving photocurrent.

The photocurrent density in a semiconductor can be described by

$$j(t) \propto I(t) \otimes [n_f(t) e v(t)], \tag{3.9}$$

where $\otimes$ denotes the convolution product, $I(t)$ the optical intensity, $e$ the elementary charge, $n_f(t)$ the density of free charges and and $v(t)$ the velocity of the photocarriers.

The rate equation for the generated carriers is

$$\frac{dn_f}{dt} = -\frac{n_f}{\tau_c} + G(t), \tag{3.10}$$

where $\tau_c$ is the carrier trapping rate and $G(t)$ is the generation rate of charges from the laser pulse.

The classical Drude model is a good description of the dynamics of free photogenerated carriers in a semiconductor. The average velocity of the free carriers can here be modeled by the differential equation:

$$\frac{dv}{dt} = -\frac{v}{\tau_s} + \frac{e}{m^*}E_{loc}(t), \tag{3.11}$$

where $\tau_s$ is the carrier scattering rate, $m^*$ the effective mass of the carriers and $E_{loc}$ the local electric field.

An important effect that needs to be included is the screening of the applied electric bias field due to the induced free charges setting up a polarization field opposite direction of the bias field [69]. The effect of the space-charge reduces the bias field to

$$E_{loc} = E_{bias} - \frac{P_{sc}}{\eta\epsilon} \tag{3.12}$$

where $P_{sc}$ is the polarization field due to screening, $\eta$ is a geometrical factor equal to three for an isotropic dielectric material [69]. Pedersen *et al.* demonstrated in Ref. [70] that increasing the optical injected carriers can screen the applied bias-field so it strongly influences the amplitude and the THz pulse shape.

From these considerations important properties of the semiconductor material used for photoconductive antennas are high electron mobility, high breakdown voltage and high resistivity.

Equation 3.9 results in that the carrier drift velocity and hence the mobility ($v_d = \mu E$) is an important material parameter for the semiconductor material used for the THz generation since $n(t)ev(t)$ is presenting the impulse response to the fast femtosecond laser pulse excitation. A short carrier lifetime is in opposite to the photoconductive detector not a requirement.

A high breakdown voltage is desirable for the application of high biasfields while a high dark resistivity minimizes the heat in the structure.

The most used semiconductor materials used with modelocked Ti:Sa femtosecond lasers are GaAs, low-temperature grown GaAs (LT-GaAs) and radiation-damaged Silicon-on Sapphire (RD-SOS).

The THz pulse is typically collimated after generation in the point source like photoconductive gap by a high resistivity hyper-hemispherical silicon lens. High resistivity silicon matches the refractive index of GaAs very well at THz frequencies (Si 3.47 and GaAs 3.6) which avoids reflections between the substrate and the lens. Further has Si low absortion and very low dispersion at THz frequencies [71].

### Optical rectification

Another generation scheme for ultrashort electromagnetic pulses is employing nonlinear crystals, i.e. ZnTe, and can be described by the nonlinear phenomenon called *optical rectification*. Optical rectification is a nonlinear optical effect originating from the second order susceptibility $\chi^{(2)}$ that in the frequency domain produces polarization $P(k, \omega)$.

$$\begin{aligned} \mathbf{P}(k,\omega) &= \mathbf{P}^{(0)}(k,\omega) + \mathbf{P}^{(1)}(k,\omega) + \mathbf{P}^{(2)}(k,\omega) + \cdots \\ &= \mathbf{P}^{(0)}(k,\omega) \\ &\quad +\varepsilon_0(\chi^{(1)}_{ij}\mathbf{E}_i(k_i,\omega_i) + \chi^{(2)}_{ijk}\mathbf{E}_i(k_i,\omega_i)\mathbf{E}_j(k_j,\omega_j) + \cdots) \end{aligned} \tag{3.13}$$

where $k$ is the wavenumber, $\omega$ is the angular frequency and $\chi^{(n)}$ is the susceptibility tensor of rank $n+1$. $\mathbf{P}^{(0)}$ is the static polarization, $\mathbf{P}^{(1)}$ is the linear polarization and $\mathbf{P}^{(2)}$ is the quadratic polarization. By inspection

of the left hand side of equation 3.13 it can clearly be seen that $\mathbf{P}^{(2)}$ and higher orders susceptibilities are giving rise to frequency mixing terms.

Now assuming two plane electromagnetic waves $E_1 = \frac{1}{2}[A_k(t)\exp(-i\omega_1 t) + c.c.]$ and $E_2 = \frac{1}{2}[A_l(t)\exp(-i\omega_2 t) + c.c.]$, where $A_{k,l}$ are the envelopes and $\omega_{1,2}$ are the carrier frequencies, then the $2^{nd}$ order induced polarization can be written as:

$$\begin{aligned} P^{(2)} &= \epsilon_0 \chi^{(2)}_{jkl} \frac{1}{2}[A_k(t)\exp(-i\omega_1 t) + c.c.] \\ &\qquad \times \frac{1}{2}[A_l(t)\exp(-i\omega_2 t) + c.c.] \\ &= \epsilon_0 \chi^{(2)}_{jkl} \frac{1}{4}\{[A_k A_l \exp[-i(\omega_1 - \omega_2)t] + c.c.] + \\ &\qquad [A_k A_l \exp[-i(\omega_1 + \omega_2)t] + c.c.]\} \\ &= P^{(2)}_{\Delta} + P^{(2)}_{\Sigma} \end{aligned} \tag{3.14}$$

Looking at Eq. 3.14 we see that $P^{(2)}_j$ consists of a sum term, $P^{(2)}_{\Sigma}$ and a difference term, $P^{(2)}_{\Delta}$. If we now assume that the electromagnetic waves are identical i.e. $A_k = A_l = A$ and $\omega_1 = \omega_2 = \omega$, we get

$$\begin{aligned} P^{(2)} &= \frac{1}{2}A^2(t)\epsilon_0 \chi^{(2)}_{jkl}[1 + \frac{1}{2}\exp(-i2\omega t) + c.c.] \\ &= P^{(2)}_{\Delta}(0) + P^{(2)}_{\Sigma}(2\omega) \end{aligned} \tag{3.15}$$

Equation 3.15 shows that we get two non-zero polarization terms which both are dependent on the electric field amplitude. $P^{(2)}_{\Delta}(0)$ is completely independent of the carrier frequency and describes the effects of *optical rectification*. The term $P^{(2)}_{\Sigma}(2\omega)$ is oscillating at twice the carrier frequency and describes the nonlinear phenomenon of *second harmonic generation (SHG)*.

$P^{(2)}_{\Delta}(0)$ in equation 3.15 is proportional to the square of the electromagnetic amplitude and is thus proportional to the incident wave intensity. If

$A = const.$ i.e. the amplitude is time-independent which equals a permanent polarization inside the medium.

If we instead apply an amplitude modulated electromagnetic wave, this will result in a time-dependent $P_{\Delta}^{(2)}(0)$. According to the wave equation shown in equation. 3.7, this time dependence will lead to an electromagnetic radiation. This is the property that is used for the generation of the ultrafast electromagnetic THz signals in the nonlinear crystal. When a femtosecond pulse is incident on a ZnTe crystal, the optical rectification process creates a time-varying induced polarization which in the following give rise to an broadband electromagnetic radiation which is covering the THz frequency range.

The above description of the optical rectification is only valid for descriptions of the local interaction, but it clearly neglects wave propagation inside the crystal. To obtain a good efficiency of the process one generally would use a crystal of a appreciable thickness, thus then propagation effects cannot be ignored. Pulse broadening may occur for both for the optical wave and for the generated THz pulse throughout the crystal. However, the most critical effect is phasematching between the THz wave and the optical wave[72].

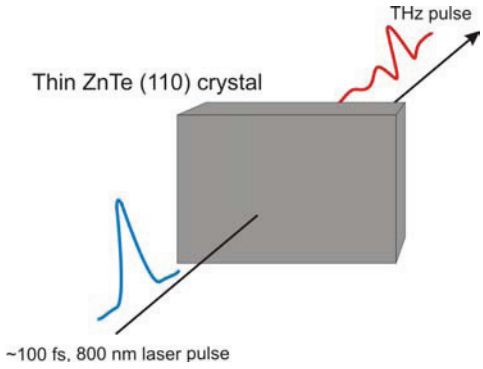


Figure 3.2: Principle of optical generation of THz radiation by optical rectification (Pockels effect).

## 3.3 THz detectors

### Detection with photoconductive antennas

The detection scheme for photoconductive antennas is very much the inverse process of the photoconductive generation scheme. The main difference to the emitter is that the detector has exchanged the DC-bias supply with an ampere meter. Photocarriers are created in the photoconductive gap by a optical probe pulse, the carriers are then accelerated by the incident THz-field and the current in the antenna is detected typically by an lock-in amplifier. The electric field of the THz pulse is mapped in the detector as a function of time by scanning the arrival time of the optical gate pulse with respect to the THz pulse.

The photocurrent in the detector $J(t)$ is represented by:

$$J(\tau) = \frac{1}{T}\int_0^T E_{THz}(t)\sigma(t-\tau)dt, \tag{3.16}$$

where $\sigma$ represents the surface conductivity in the photoconductive gap. The ideal detector would have a delta function detector response to map out the exact incoming THz field. However, the detector photocurrent is a convolution of the THz field with the finite conductivity which is determined by the optical intensity, carrier drift velocity and carrier population. The detector bandwidth can be optimized by decreasing the response time of the detector by using semiconductor materials with a sub-picosecond carrier recombination time and a relative high carrier mobility.

Two main materials have been used with 800 nm Ti:Sapphire lasers because of their sub-ps recombination time and their relative high carrier mobility. These materials are LT-GaAS [73] and RD-SOS[74].

### Electro-optic detection

Another detection method uses a free-space electro-optic detection technique (Fig. 3.4) [75–77]. This technique uses another <110>-oriented ZnTe crystal. The THz pulse and the laser pulse are propagated collinearly through the ZnTe crystal. The THz pulse induces a birefringence in ZnTe

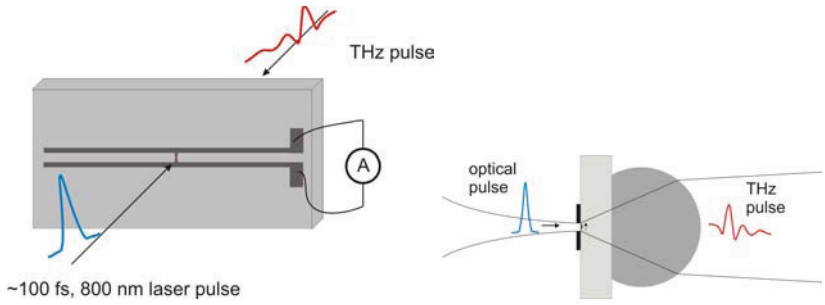


Figure 3.3: Principle of detection of THz radiation by a photoconductive antenna. The presence of THz radiation and a optical gating pulse drives a current in the photoconducting antenna which is measured by a current amplifier or lock-in. (left) Front view of the photoconductive detector, (right) side view of the photoconductive detector depicting the Si lens used to collect the THz pulse into the photoconductive gap.

crystal which is read out by the linearly polarized laser pulse. When both the laser pulse and the THz pulse are in the crystal, the laser polarization will be rotated by the presence of the THz pulse linearly to the incident THz field strength. Using a $\lambda/4$ waveplate and a beamsplitting polarizer together with a set of balanced photodiodes, the THz pulse amplitude is mapped out by monitoring the laser pulse polarization rotation after the ZnTe crystal at a variety of delay times with respect to the THz pulse.

The induced phase retardation in the ZnTe crystal is given by

$$\Delta\Gamma = \frac{2\pi}{\lambda} d n_{opt}^3 r_{41} E_{THz}, \tag{3.17}$$

where $d$ is the optical thickness of the crystal, $n_{opt}^3$ the group refractive index of the electro-optic crystal at the probe beam wavelength and $r_{41}$ the electro-optic coefficient. Equation 3.17 shows the ability to read out the full electric field $E_{THz}$, both amplitude and phase, as the THz field is directly proportional with the phase retardation of probe beam.

A fundamental limit to the detection bandwidth using this technique is

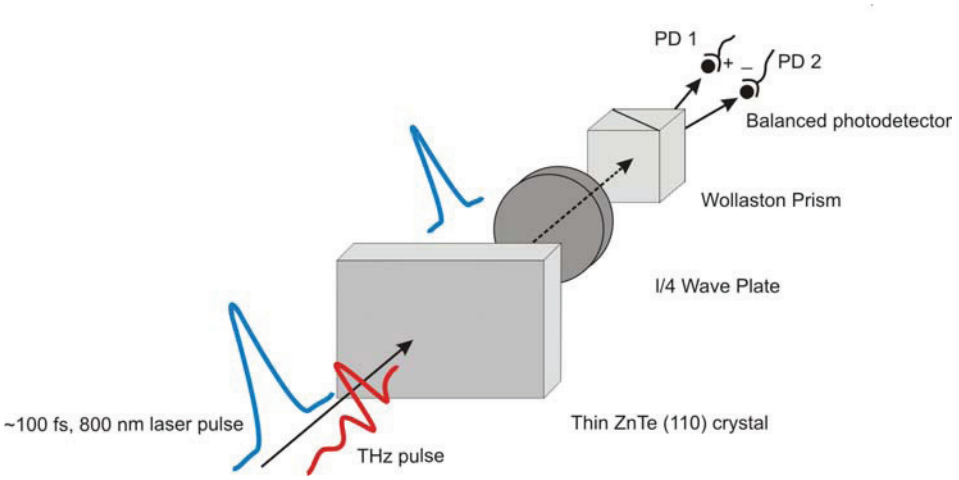


Figure 3.4: Principle of optical detection of THz radiation by electro-optic sampling. The presence of THz radiation in the ZnTe crystal rotated the polarization of the 800 nm probe pulse. The polarization change is detected in a pair of balanced photodiodes.

the potential phase mismatch in the crystal between the THz pulse and the 800 nm detection beam due to the difference in refractive index at these two wavelengths [77]. Another fundamental bandwidth limiting characteristic for ZnTe is a phonon absorption at 1.6 and 3.7 THz [78] and a TO phonon at 5.31 THz [75].

ZnTe is the most commonly used electro-optic crystal, although GaSe, GaP, InP, GaAs and DAST also have been used. A much more detailed study on the crystal orientation dependence of the THz detection in ZnTe is given by Planken et al. in [79].

## 3.4 THz time-domain spectroscopy

In the previous section we have described the concepts to generate and detect THz radiation with photoconductive antennas. This section will

deal with most prominent THz spectroscopy scheme; THz time-domain spectroscopy (THz-TDS).

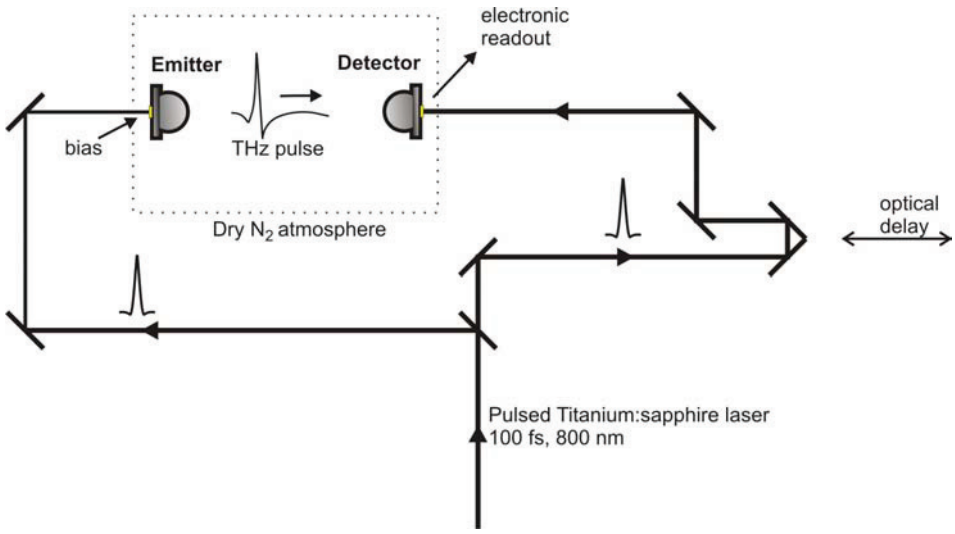


Figure 3.5: Sketch of a typical THz-TDS using photoconductive antennas as emitter and detector. The sample under investigation is positioned in the THz beam path and sample cell is typically purged with $N_2$ to avoid water absorption lines in the acquired spectrum.

Figure 3.5 shows a sketch of a typical THz-TDS setup. A optical beam-splitter splits the ultra short laser pulses from the modelocked Ti:sappire into two beam paths. One part is directed into the THz generation arm and the other will be used at the detector as gating pulse. Each beam is focussed on a photoconductive switch which generates and detects the THz pulse, respectively. Either the generation beam or the detection beam is led through a variable delay line in order to secure that the optical pulse at the detector arrives at the same time as the THz pulse and gates the detector. By changing the optical delay line the THz pulse is mapped out as a function of time. The weak photocurrent in the detector is measured

by a lock-in amplifier or a high gain transimpedance amplifier to ensure a good signal-to-noise ratio. When using a lock-in detection scheme either the optical beam, the THz beam or the bias voltage of the emitter is modulated at the lock-in detection frequency. After generation in the photoconductive antenna the THz beam is collimated with a high resistivity hyper-hemispherical Si lens and at the detector again focussed by the Si lens into the photoconductive gap. Often a intermediate focus of the THz pulse is required and can easily be introduce by using two pairs off-axis parabolic mirrors.

An example on the detected time dependent electric field $E(t)$ propagating in lab air and nitrogen purged dry environment, respectively, is shown in Fig. 3.6(left). The oscillations on the measurement of the THz pulse obtained in lab air are due to the decaying of rotational transitions in water molecules of the water vapor in lab air atmosphere [80]. The THz beam path is due to this usually kept in a $N_2$ or dry air atmosphere.

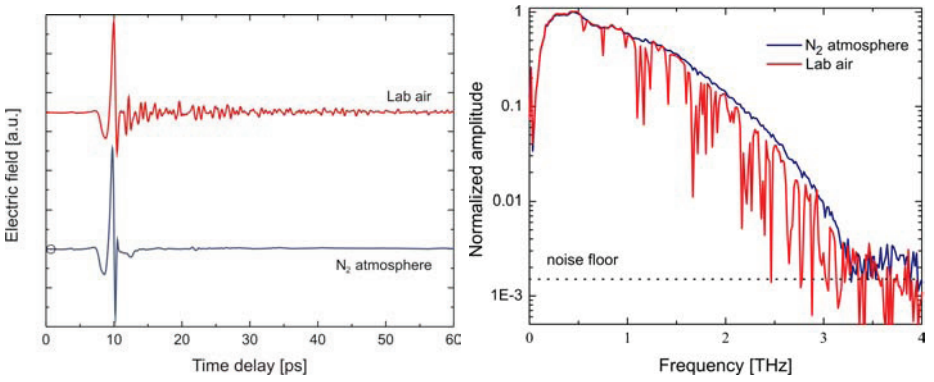


Figure 3.6: (left) Terahertz pulse taken in a classical THz-TDS setup using a 100 fs, 800 nm pulsed laser and photoconductive antennas. (right) Fourier transform of the THz pulse showing the frequency components of the amplitude of a THz pulse in lab air and in a dry atmosphere.

The obtained time dependent electric field measurement $E(t)$ can be Fourier transformed by the discrete equivalent of the Fourier transform of

$$E(\omega) = \frac{1}{2\pi} \int_{-\infty}^{\infty} E(t) e^{-i\omega t} d\tau, \tag{3.18}$$

where $E(\omega)$ is the frequency dependent electric field. The amplitudes of the Fourier transformations of the time dependent electric fields of lab air and dry nitrogen purged air are shown in Fig. 3.6(right), respectively. The distinct lines in the spectrum of the lab air are the water vapor absorbtion lines. The maximum detectable bandwidth of this spectrometer is up to 3 THz and the system has a signal-to-noise ratio of approx. 1:800 at the peak of the spectrum.

A great feature of THz-TDS compared to other optical spectroscopic techniques is, that this technique obtains the electric field and not just the intensity. Resulting in that both the amplitude and phase of the field are obtained one can e.g. extract the complex refractive of a material with known thickness without the need of the *Kramers-Kronig* relation which describes the mathematical relation between the real and imaginary part of a complex function [81].

The complex index of refraction is here defines as:

$$\tilde{n(\omega)} = n(\omega) - i\kappa(\omega) = n(\omega) - i\frac{\alpha(\omega)c}{2\omega}, \tag{3.19}$$

where $n(\omega)$ is the frequency dependent index of refraction and $\kappa(\omega)$ is the frequency dependent extinction coefficient, $\alpha(\omega)$ is the absorption coefficient and $c$ the speed of light in vacuum. The complex refractive index has a direct relationship to both the conductivity and the dielectric function of a medium which makes the knowledge of either one of these highly useful.

The following will show how to determine the frequency dependent index of refraction and the absorbtion of a sample using a THz-TDS operated in transmission-mode configuration. The transmitted field through a sample of thickness $d$ is depicted Fig. 3.7.

The reference pulse in transmission-mode trough an spectrometer without sample is needed for the later the calculation of the index of refraction.

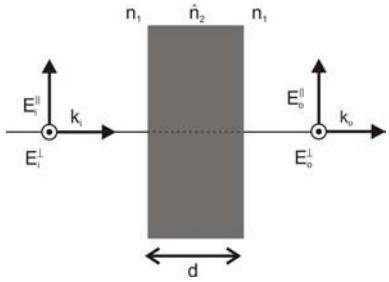


Figure 3.7: Sketch of a transmission through a sample with thickness $d$ and complex index of refraction $\hat{n}_2$.

A reference pulse $E_{ref}(\omega)$ in frequency domain for two orthogonal polarizations can be expressed as

$$\begin{aligned}\begin{pmatrix} E^{\parallel}_{ref}(\omega) \\ E^{\perp}_{ref}(\omega) \end{pmatrix} &= \begin{pmatrix} E^{\parallel}_{i}(\omega) \\ E^{\perp}_{i}(\omega) \end{pmatrix} \cdot e^{-\alpha_{air} d/2} \cdot e^{-i\omega n_{air} d/c} \\ &= \begin{pmatrix} E^{\parallel}_{i}(\omega) \\ E^{\perp}_{i}(\omega) \end{pmatrix} \cdot e^{-i\omega d/c}, \end{aligned} \tag{3.20}$$

where $E_i(\omega)$ is the incident THz pulse generated by the emitter, $n_{air}$ is the refractive index of air, which is assumed to be 1 and $\alpha_{air}$ is the absorption coefficient of air which is assumed to be zero.

When placing the sample into the beam path of the spectrometer, the electric field alters to $E_{sam}(\omega)$ and can now be expressed as

$$\begin{pmatrix} E^{\parallel}_{sam}(\omega) \\ E^{\perp}_{sam}(\omega) \end{pmatrix} = \begin{pmatrix} E^{\parallel}_{i}(\omega) \cdot t^{\parallel}_{12} \cdot t^{\parallel}_{21} \\ E^{\perp}_{i}(\omega) \cdot t^{\perp}_{12} \cdot t^{\perp}_{21} \end{pmatrix} \cdot e^{-\alpha_{sam}(\omega) d/2} \cdot e^{-i\omega n_{sam}(\omega) d/c}, \tag{3.21}$$

where $n_{sam}(\omega)$ is the refractive index of the sample, $\alpha_{sam}(\omega)$ the absorption coefficient and $t^{\parallel}_{12} \cdot t^{\parallel}_{21}$ and $t^{\perp}_{12} \cdot t^{\perp}_{21}$ the Fresnel transmission coefficient for the interfaces for parallel and orthogonal polarization, respectively. For

simplicity are we in the following assuming that the incoming field only is parallel polarized. The unknown electric field $E_i$ is represented in both Eq. 3.20 and Eq. 3.21, and can therefore be eliminated by taking the ratio of the two fields (assuming $n = n_{sam}$ and $\alpha = \alpha_{sam}$).

$$\begin{aligned} \frac{E_{sam}(\omega)}{E_{ref}(\omega)} &= \frac{E_i(\omega) \cdot t_{12} \cdot t_{21} \cdot e^{-\alpha(\omega)d/2} \cdot e^{-i\omega n(\omega)d/c}}{E_i(\omega) \cdot e^{-i\omega d/c}} \\ &= t_{12} \cdot t_{21} \cdot e^{-\alpha(\omega)d/2} \cdot e^{-i\omega[n(\omega)-1]d/c}. \end{aligned} \tag{3.22}$$

At normal incidence of the field onto the sample ($\theta_i = 90°$) equation 3.22 reduces to

$$\frac{E_{sam}(\omega)}{E_{ref}(\omega)} = \frac{4\hat{n}(\omega)}{[1+\hat{n}(\omega)]^2} \cdot e^{-\alpha(\omega)d/2} \cdot e^{-i\omega[n(\omega)-1]d/c} \equiv A(\omega) \cdot e^{-i\phi(\omega)}. \tag{3.23}$$

The ratio between $E_{sam}(\omega)$ and $E_{ref}(\omega)$ is a complex expression with the amplitude $A(\omega)$ and phase $\phi(\omega)$. The index of refraction and the absorption coefficient can now be extracted out of equation 3.23 by inspection of the real and imaginary part.

When the sample thickness is comparable or larger than the wavelength (1 THz = 300 $\mu$m), the index of refraction of the sample can be expressed just by looking at the phase difference between the reference and the sample pulse. In this situation the phase shift arising from the Fresnel coefficients is much smaller than the phase shift originating from the sample propagation,

$$n(\omega) \simeq 1 + \frac{c}{\omega d}\phi(\omega). \tag{3.24}$$

After determination of the refractive index one can calculate the absorption coefficient of the sample from the amplitude of equation 3.23.

$$\alpha(\omega) \simeq -\frac{2}{d} \cdot \ln\left\{ A(\omega)\frac{[1+n(\omega)]^2}{4n(\omega)} \right\}. \tag{3.25}$$

## 3.5 Pulsed terahertz imaging techniques

### Amplitude and phase imaging

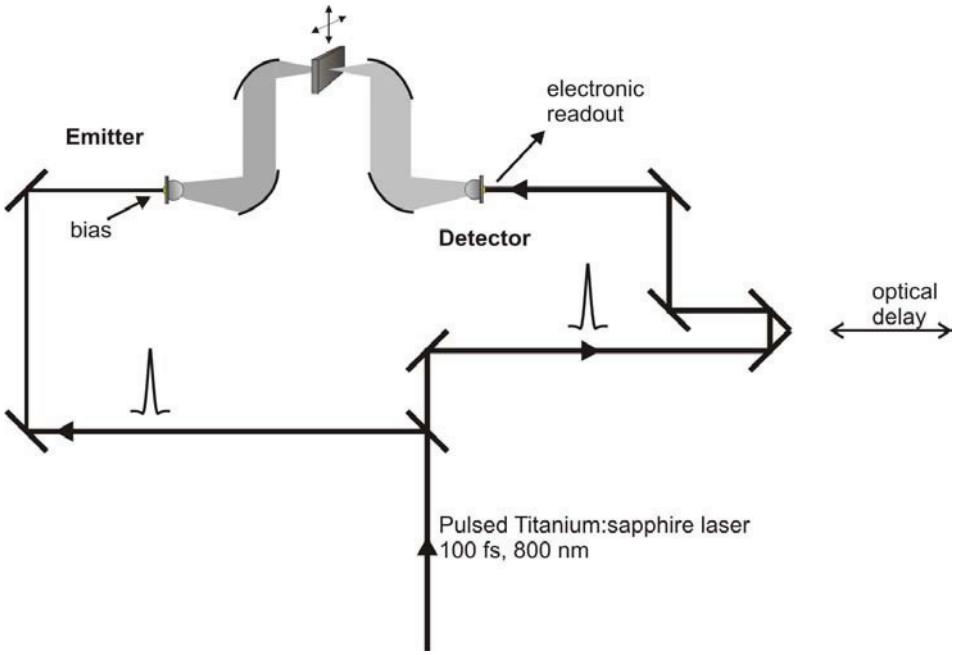


Figure 3.8: Schematic of a typical transmission-mode raster scan time-domain imaging system. The imaging plane is at an intermediate focus point half way between emitter and detector.

A popular THz imaging system has since the very beginning of THz imaging with [27, 82] simply been the teraherz time-domain spectroscopy (THz-TDS) setup. Various imaging setups make use of raster scanning an object in the THz beam of a THz-TDS either in transmission- or reflection-mode configuration (Fig. 3.8). An image acquired by raster scanning in a THz-TDS contains a full THz waveform for every single pixel, enabling the data analysis capability described in the previous section. However,

these systems use often mechanical translation stages to move the object in the THz beam and here is a clear trade off between scanning speed and scanning range (time delay). An increase in scanning speed is directly converting into an either more coarse image or less information in every pixel due to a reduction in scanning range. The advent of the asynchronous optical sampling technique used in [83, 84] promised a substantially increased image acquisition speed at the expense of a more complex femtosecond laser source. Two femtosecond Ti:sapphire lasers with slightly different repetition rates are locked with a fixed frequency offset one to the other. One laser is used for generation at the THz emitter and the other is gating the THz waveform at the detector. The delay between the laser pulses sweeps automatically across the THz pulse relative to the gating pulse where the scan rate is determined by the frequency offset between the two laser. In [83] a time delay of 1 ns is scanned at a frequency of 5 kHz without moving mechanical parts. Compared with that of conventional TDS schemes based on lock-in detection and mechanical delay stages, the readout time of the THz detector is reduced by a factor of 20.

### Tomography

Stacked time-of-flight measurements, by the authors called terahertz tomography imaging, where the first 3D images first were described by Mittleman *et al.* [86] in 1997. The measurement setup was a classical THz-TDS operated in reflection geometry and including a mechanical x-y stage scanning the object across a focussed THz beam. The imaging technique acquires thin 2D cross-sectional slices of the internal structure of a 3D object by detecting the multiple reflections from the incident pulse at different dielectric interfaces (Fig. 3.10). The 3D internal structure can be reconstructed by stacking of the acquired 2D data. Figure 3.11 shows a measurement of a 3.5-in. floppy disk. Changes of the refractive index at dielectric interfaces in the 2D slice's can be mapped out and are shown in Fig. (3.11b).

The principles of tomography imaging allows imaging of highly transparent, non-polar, non-metallic materials. The pulsed nature of the THz-TDS makes it directly usable for acquiring depth information of a 3D-

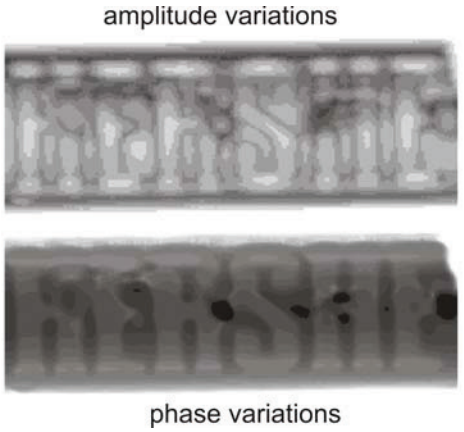


Figure 3.9: Shows a THz image of a chocolate bar obtained by raster scanning the object in a THz TDS in transmission mode. The upper image shows the amplitude variation of the peak-to-peak amplitude of the transmitted pulse. The letters are visible due to scattering of the incoming THz pulse and the almonds in the chocolate bar are visible due to a different absorbtion coefficient than the rest of the bar. The lower image the phase variation of the THz pulse. Here the image gives evidence of thickness variation across the bar due to the embossed letters in the chocolate. Adapted from [85].

object. By time-of-flight analysis the different layers can be assigned to the internal structure of the object, which makes this technique extremely interesting for non-destructive testing in industrial applications.

THz time-of-flight principles are used in one of the most prominent industrial application of THz imaging until today. NASA is using the technology to image insulation foam and especially looking for the identification of defects in the space shuttle foam [87]. The crash of the NASA space shuttle Columbia was assigned to possible defects as voids and delaminations of the insulation foam of the space shuttle fuel tank. Since it is difficult to locate defect in insulation with other techniques as X-ray or ultra-sound,

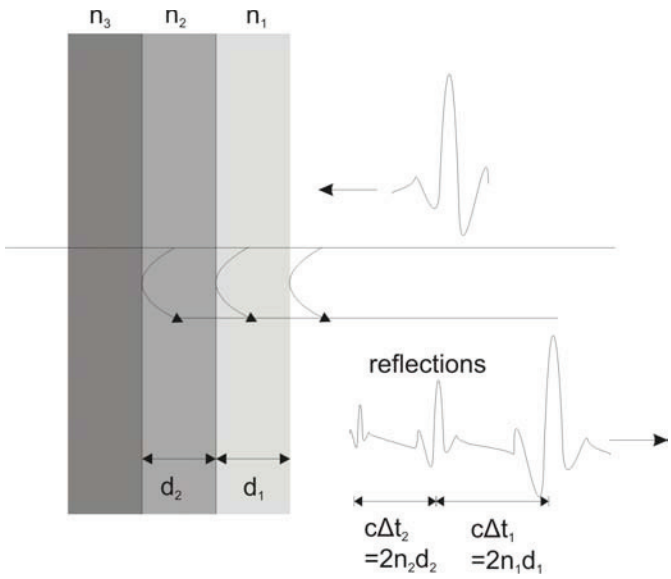


Figure 3.10: Reflection of THz pulse from dielectric interfaces.

THz tomography has found application in non-destructive low-density, low absorption testing.

### Computed Tomography imaging

Computed tomography (CT) imaging is an imaging technique normally referring to a cross-sectional 3D-image taken with X-rays. In classical CT systems the object or the emitter-detector pair is rotated and 2D-slices called shadow images are taken at different rotational angles. The imaging scene can be described by the Radon integral:

$$P(r,\theta) = \int_{L(r,\theta)} f(x,y)ds, \tag{3.26}$$

where $f(x,y)ds$ is the probability that a ray is absorbed or deflected in the segment $ds$ along a straight line L. $f(x,y)$ represents the optical

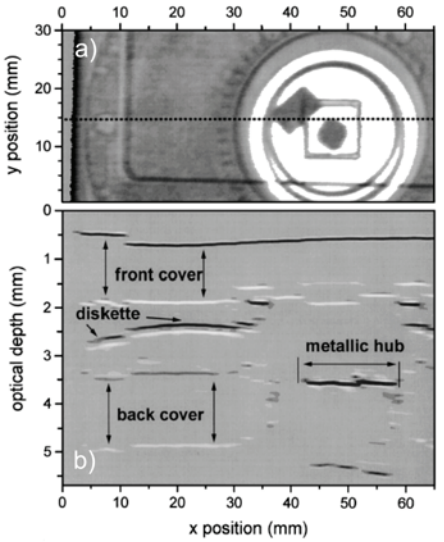


Figure 3.11: THz image of a 3.5-in. floppy disk depicting the total reflected power (a) and a tomographic image (b) at $y = 15\ mm$ marked by the dashed line in (a). Lighter and darker regions indicate changes in the index of refraction in the object. Reprinted from [86].

property of the object at the point $(x, y)$. By inverse transformation of the integral equation the CT image is reconstructed.

CT THz imaging was first demonstrated by Zhang an co-workers in Ref. [14]. The most important difference between X-ray CT and THz-CT is that a THz-CT image can contain information about the amplitude and the phase of the object. This lead to extra valuable information, as the refractive index.

The radon integral in equation 3.26 can be adapted for THz-CT by Fourier transforming it and rewriting it in its complex form

$$E_{det}(\omega, \theta, l) = E_i(\omega) exp\left[\int_{(r,\theta)} \frac{-i\omega}{c}(n(r) - i\kappa(r))dr\right], \tag{3.27}$$

where $E_i$ is the Fourier components of the incoming field at $\omega$, $E_{det}$ is the detected field at frequency $\omega$, L is a straight line between emitter and detector at an angle $\theta$ and a horizontal offset $l$ from the object's rotation axis and $n(r) - i\kappa(r)$ is the complex refractive index that needs to be determined at position $r$.

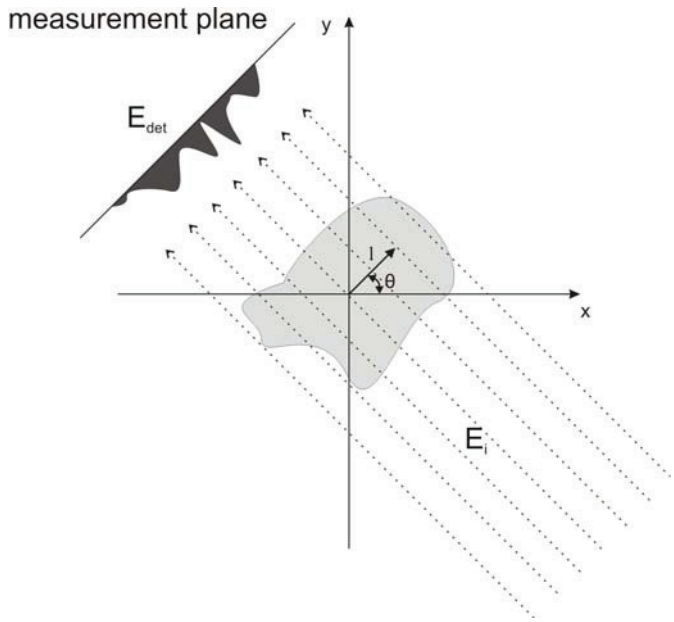


Figure 3.12: Schematic of computed tomography. The object is rotated around the z-axis (z is out of the page). The incident THz beam $E_i$ propagates through the object at an angle $\theta$ and a offset $l$ from the rotation axis. In the measurement plane both the amplitude and the phase of $E_{det}$ is detected.

By making the approximation that the detected pulse is related to the incident pulse by equation 3.27 the Radon transform can be inverted and used to reconstruct the image with filtered backprojection algorithm [14].

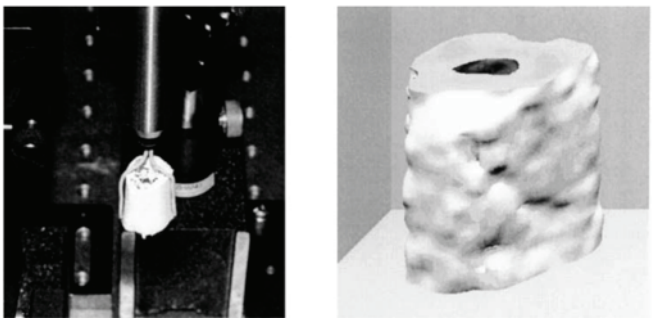

Figure 3.13: Photograph(left) and a rendered 3D reconstructed THz-CT image of a turkey bone. Reprinted from [14].

### Synthetic aperture imaging systems

THz imaging system making use of phased array and synthetic aperture techniques, well known from radar systems, have been proposed by several groups. Mostly these studies were limited to simple systems making use of a single emitter-detector pair that typically is scanned itself or the THz beam is steered with an advanced mirror arrangement to spatially cover the imaging plane. In ref. [17] McClatchey *et al.* presented an THz synthetic aperture system based using an inverse synthetic aperture deconvolution technique. The system demonstrates millimeter and submillimeter resolutions along the cross range and range axes, respectively. The range resolution, determined by the THz pulse bandwidth is 0.12 mm, while the cross range resolution is 1.2 mm. Further does the same group present fundamental studies on a synthetic phased array imaging system that can produce images sharp enough to resolve features whose size is in the order of the THz wavelength [18]. Both systems employ only one single emitter-

detector pair together with an advanced moving mirror array making up the phased array system.

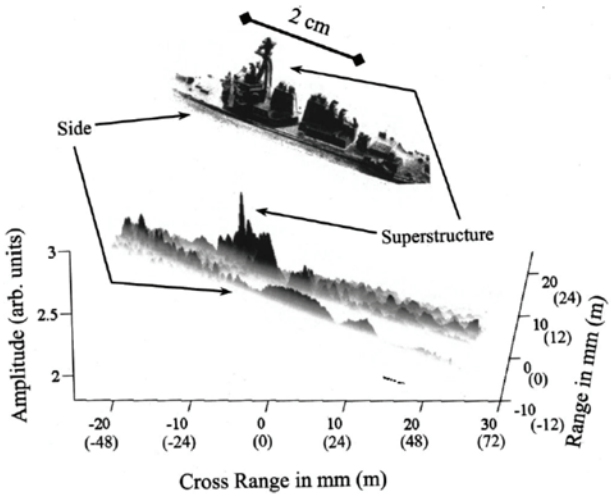


Figure 3.14: High contrast photograph and THz SAR image of a destroyer scale model (1:2000). SAR images are taken with 20° angular range and 1° resolution. Reprinted from [17].

Bandyopadhyay *et al.* have in [19] proposed an interferometric array inspired by radio-interferometry. The idea of the imaging interferometer consists of an array of multiple individual detectors or sensors (Fig. 3.15). Each pair of THz detectors measure the amplitude and phase of incoming THz radiation. By calculating the spatial Fourier components of all different detector positions an image can be reconstructed. Bandyopadhyay *et al.* [19] presents though only data from a pair of CW photomixers mowed along the line sketched in Fig. 3.15a.

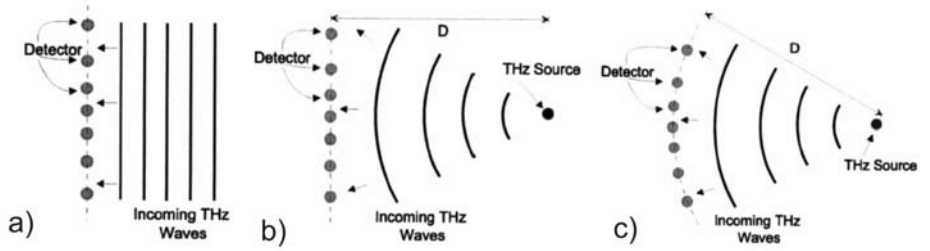


Figure 3.15: a) Parallel wavefronts incident on a planar arrangement of detectors. The wavefront is detected simultaneously at all detectors. Requires a point source at infinite distance from the detection array. b) The THz source is placed at a finite distance D from the detector array. This introduces a phase delay between the detected wavefronts in the detectors. This situation is difficult with respect to data analysis since the standard Fourier inversion procedure of interferometric imaging assumes planar wavefronts. (c) Adjusting of the detectors is matching the circular incoming wavefront, so the detectors detect the same wavefront simultaneously. The circular arrangement is analogous to situation a). Adapted from [19].

## 3.6 Conceptional ideas for a new pulsed THz imaging system

After having reviewed the field of pulsed THz imaging systems one can recognize the clear need for a robust, fast and easy-to-use multi-element THz imaging system. The fundamental concepts of a vast of imaging techniques have been showed here, mostly though just the basic concept. Time-flight-measurements have until today been the most successful technique finding more and more application areas, also in industrial applications. The fundamental problem of the technique is still the image acquisition time which for most industrial applications is far too long. This problem has been addressed attention and various techniques have been proposed to speed up the imaging time. There is though today still a profound need for a faster system for imaging at e.g. video rate.

In chapter 5 we will address both the need for a multi-element system, together with an image acquisition concept making use of syntectic apertures image reconstruction techniques and a fast electronic time-delay scan.

# Chapter 4

# Experiments on carbon nanotubes using a multi-element THz-system

Before going into a detailed description of our development of a multi-element imaging system, this chapter presents experimental results using an existing fiber coupled multi-element THz time-domain spectroscopy (THz-TDS) system. Besides the experimental data acquired, these experiments will show the extreme usefulness of a multi-element system in e.g. angle dependent scattering measurements. The used spectrometer has the capability of very fast realignment of emitters and detectors due to the fiber coupled sensor heads and further the possibility of simultaneous measurements of scattered signals at different detector location. All this allows measurements only very hardly achievable with a classical THz time-domain spectrometer and without very time consuming realignment procedures.

THz time-domain spectroscopy of carbon nanotubes (CNTs) has previously been used to investigate their optoelectronic properties [88–90]. These works focused on characterizing the frequency-dependent electronic and optical properties (refractive index, absorption, and conductivity) of a variety

of configurations of carbon nanotubes.

First this chapter will present results examining the scattering of THz radiation from multi-walled carbon nanotubes (MWCNTs) oriented perpendicularly to the substrate plane. The MWCNT's under investigation were provided by the group of Dr. Koziol from Cambridge University, UK. Despite the wavelength of the terahertz radiation (0.3 – 3 mm) being significantly larger than the diameters of the nanotubes, significant scattering of the incident terahertz radiation occurs. In fact, when compared to measurements performed on bulk metals, the scattering from the oriented nanotubes is significantly higher. At this point in time it is still not clear what gives rise to the enhanced scattering of the oriented tubes and will require further research in future. However, first measurement results are presented here.

The chapter will be closed by a different experiment on another type of multi-walled carbon nanotube fibers oriented in the substrate plane [91, 92]. The aim of this experiments was to investigate the possibility to monitor oxidation impurities in the nanotube sample as a function of THz transmission and reflection of the sample. The data presented is also a initial research data and must be investigated further in the future.

## 4.1 Scattering experiments on carbon nanotube carpet

With the advantages afforded by terahertz time-domain spectroscopy, it is logical that it has been used to study the optoelectronic properties of various nanomaterial systems. Due to the diffraction- limited spatial resolution, THz-TDS can not be used to probe individual nanomaterials i.e. a single nanotube. Instead, this technique characterizes the bulk electrical or optical properties. Jeon *et al.* were the first to report terahertz time-domain spectroscopy of anisotropically aligned single walled carbon nanotube films [89]. They found that their experimentally derived frequency dependent conductivity did not follow the Drude model and that it changed greatly as a function of the purity of the sample. Jeon also showed that the THz

transmission strongly followed the alignment of the THz beam polarization to the aligned direction of the nanotubes. This result inspired recent work showing that aligned carbon nanotube films can function as linear polarizers for THz radiation [93].

Since 2002, several groups have used THz-TDS with carbon nanotubes to examine the role of nanotubes type, growth conditions, host material, doping, etc. by monitoring the THz transmission, refractive index, absorption, and conductivity [88, 94–99]. One consistent issue with this work is the difficulty in determining the conductivity and other electronic properties from the terahertz data. The choice of the conduction model is difficult in the case of carbon nanotubes as, to this date, most samples are not monodisperse, meaning that each sample is often a mixture of metallic and semiconducting nanotubes. Even in the case of multi-walled carbon nanotubes, where the tubes are dominantly metallic, it is difficult to maintain a consistent tube diameter. Terahertz time-domain spectroscopy is a valid method of determining the bulk electronic properties, but it will not be able to characterize the properties of specific types of carbon nanotubes until more pure sample growth methods are discovered. Innovative methods of using terahertz radiation to study single nanotubes do exist as evidenced by Zhong's work where they studied the transport through a single carbon nanotube via the use of a field-effect transistor [100]. The bulk terahertz frequency electronic properties of other types of nanomaterials such as semiconductor nanowires [101], CdSe nanoparticles [102], and nanostructured $TiO_2$ [103] have been investigated using THz-TDS.

The multi-walled carbon nanotubes (MWCNTs) sample were grown via chemical vapor deposition (CVD) to form carpet-like films consisting of nanotubes aligned approximately parallel to one another and normal to the plane of a glass substrate [104]. Fig. 4.1 shows a SEM picture of the tubes. The approximate density of the carbon nanotubes in the carpet film is $5 \cdot 10^6$ mm$^{-2}$. The figure also shows a very good alignment of the CNTs throughout the sample (the black arrow indicate the direction of growth). The dimensions of the tube are $\approx$ 80 nm outer diameter and $\approx$ 20 nm inner diameter and the thickness of the CNT 'carpet' is approximately 500 mm. The tubes are synthesized by the CVD method at 760 $^o$C. The carrier gas

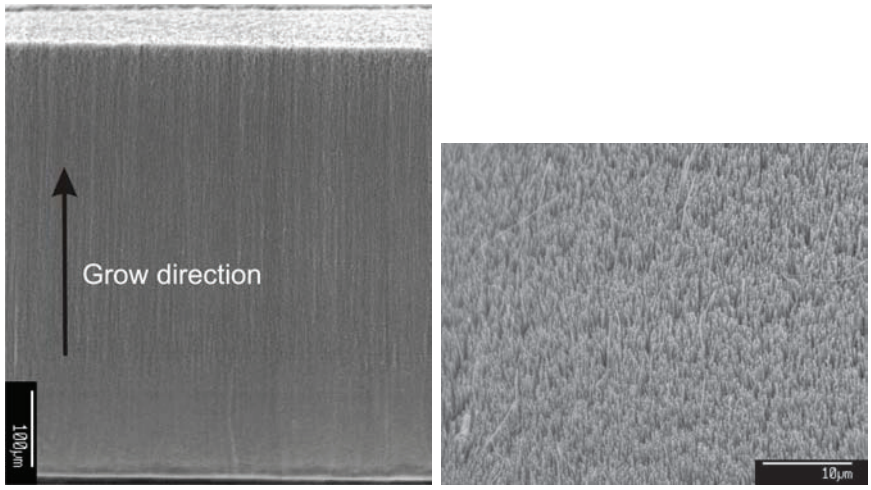


Figure 4.1: Multiwalled aligned nanotubes from Cambridge University[91]. (left) SEM image of the tubes. The carpet has a thickness of approximately 500 mm. (right) close up of the CNT´s which shows the 'carpet-like' very good alignment.

in the reactor was argon.

A THz time-domain spectroscopy system with fiber-coupled photoconductive antennas is used to perform the scattering characterization (Fig. 4.2). This worldwide unique THz-TDS system builds on a commercial THz-TDS system (Picometrix, T-Ray 2000) which was extended from the original 1 channel receiver/transmitter pair (RX/TX) version to contain 8 RX/TX channels instead. This unique system is owned by the US Air Force Research Laboratories and on long-term loan provided to the Wright State University. The experiments shown here are only using one channel and thereby only making use of the advantage of fiber coupled sensor head.

The scattering experimental setup can basically be described as follows: THz pulses are normally incident on the sample (0 degrees) and the scattered radiation is detected in reflection at several off-axis angles varying the detection angle from 20 to 80 degrees (Fig. 4.3). Wire-grid polarizers

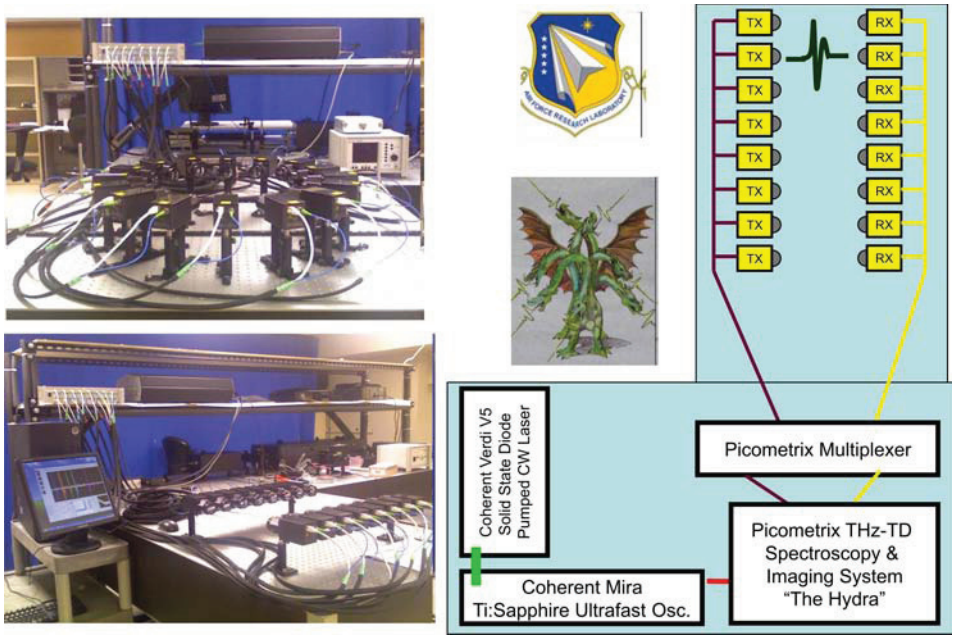


Figure 4.2: Sketch of THz spectroscopy/imaging system at Wright State University (WSU) with multiple fiber coupled transmitter/detector pairs. Traditional time-domain terahertz systems consist of one source and one detector. WSU's Hydra system has 8 source/detector pairs making it ideal for scattering and polarization dependence measurements.

are placed in front of the transmitter and receiver antennas to insure which polarization component is incident on the samples and detected.

A simple first experimental setup for measuring the direct back-reflection from the MWCNT carpet sample is depicted in Fig. 4.4(left). THz pulses, generated by a photoconductive transmitter (TX) antenna are normally incident on the sample. The reflected pulse is diverted by an in-line pellicle beam splitter that guides the pulse to the receiving (RX) photoconductive antenna. Wire-grid polarizers are placed in front of the transmitter and re-

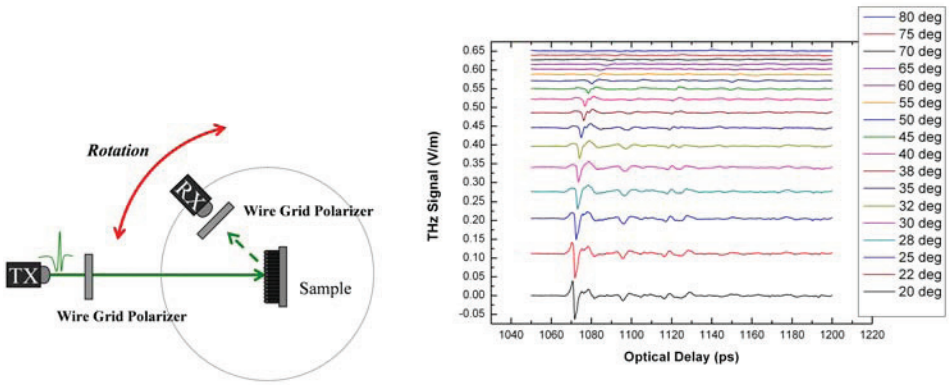


Figure 4.3: Sketch of the experimental setup. The scattering is measured by a fiber based THz TDS.

ceiver antennas to insure that a linear polarization component is incident on the samples and detected. Fig. 4.4(right) compares the time-domain THz pulse reflected from the MWCNT carpet to that from a piece of polished bulk copper. The pulse reflected from the copper is significantly stronger than that from the MWCNT carpet. This is expected as the bulk reflectivity of the carbon nanotubes should be smaller than for carbon due to the differences in conductivity.

THz pulses were normally incident on the sample (0 degrees) and the scattered radiation was detected in reflection at several off-axis angles varying from 20 to 80 degrees (Fig. 4.3(left)). Fig. 4.3(right) shows results from time-domain measurements on multi-walled carbon nanotubes in which the THz pulses were normally incident on the sample and the scattered radiation is detected in reflection at several off-axis angles. These results are compared to radiation scattered off of a bulk metal sample (brass), indicating that the scattering is greatly enhanced in the presence of the carpet-like film of nanotubes (Fig. 4.5(left)). The THz radiation scattered by the carpet falls off exponentially with increasing detection angle and does not return to an intensity level comparable to scattering from bulk metal

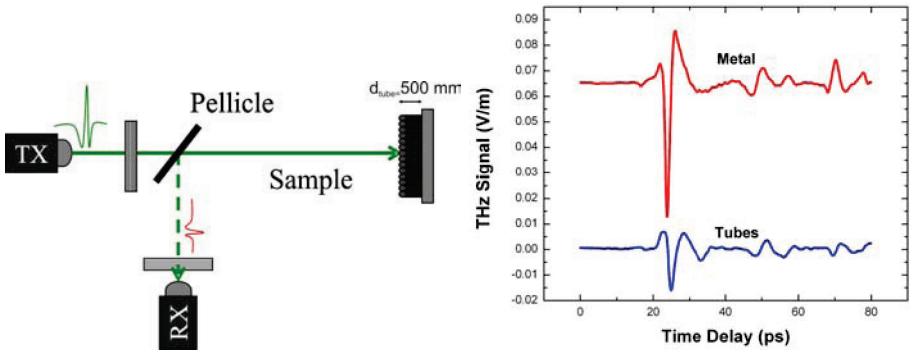


Figure 4.4: (left) Schematic of a direct backreflection measurement. (right) Backreflection data measuring backreflections from metal and nanotubes. The reflection strength from the nanotubes are seen to be lower than that of pure metal. This is expected as the bulk reflectivity of carbon nanotubes is lower due to it lower conductivity.

until 60 degrees. Fig. 4.5(right) compares the time-domain waveforms at the 30 deg. detection angle when the pulses are incident on the nanotube carpet to that from bulk metal. It can be seen that the THz radiation scattered off of the carpet is significantly larger than that for bulk metal. While Fig. 4.5(right) shows only an 80 ps long time window, actual measurements were performed over a much longer time window and no scattered radiation from the bulk metal at a magnitude comparable to that for the oriented nanotubes was present.

Fig. 4.6 provides evidence that the oriented alignment of the nanotube carpet is critical to this scattering phenomenon. THz radiation scattered from films of randomly oriented multi-walled carbon nanotubes and a sheet of graphite are more similar in magnitude to scattering from bulk metal than from oriented nanotubes. Preliminary analysis of the data in the frequency-domain indicates that the scattering is independent of frequency.

Despite the wavelength of the terahertz radiation (0.3 – 3 mm) being significantly larger that the diameters of the nanotubes, significant scatter-

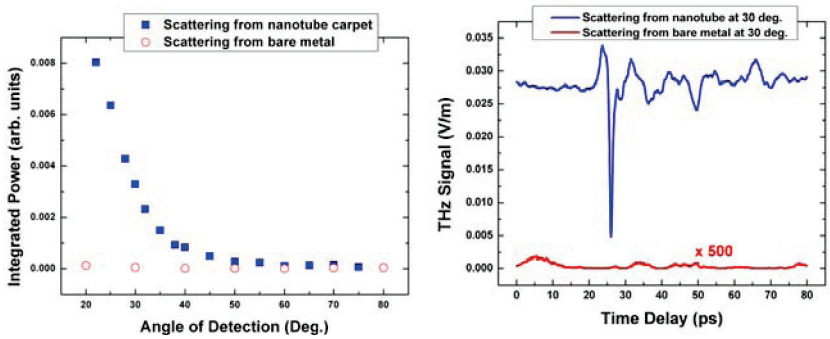


Figure 4.5: (left) Angle dependent reflection measurement at normal incidence. (right) Scattering at 30 degree detection angle at normal (0 degree) input. The nanotubes differ substantially from the bare metal data.

ing of the incident terahertz radiation occurs. In fact, when compared to measurements performed on bulk metals, the scattering from the oriented nanotubes is significantly higher. These results are counter-intuitive as the wavelength of the THz radiation is large enough that one would not expect that the scattering from the nanotube carpets to differ from the bulk metal with such significance. While the conductivity of brass is not the highest as compared to other metals, the conductivity of the nanotubes is not expected to be larger than for the brass metal. In fact, the scattering of terahertz radiation from the MWCNT carpet samples is always significantly stronger than that for bulk metal, regardless of the type of metal employed. It is possible that this behavior is due to surface roughness as terahertz spectroscopy has been shown to be sensitive to this [105–107]. A side view SEM micrograph of the MWCNT carpet suggested a surface roughness on the order of 300 nm. The spacing between the individual nanotubes in the carpet varied between 50 nm to 500 nm, which is still well below the wavelength of the THz light. The scattering of terahertz radiation by random media and the interaction of it with oriented materials has been well studied, but not for materials features that are so much smaller than the wavelength of light [108–112]. Other scattering phenomenon may

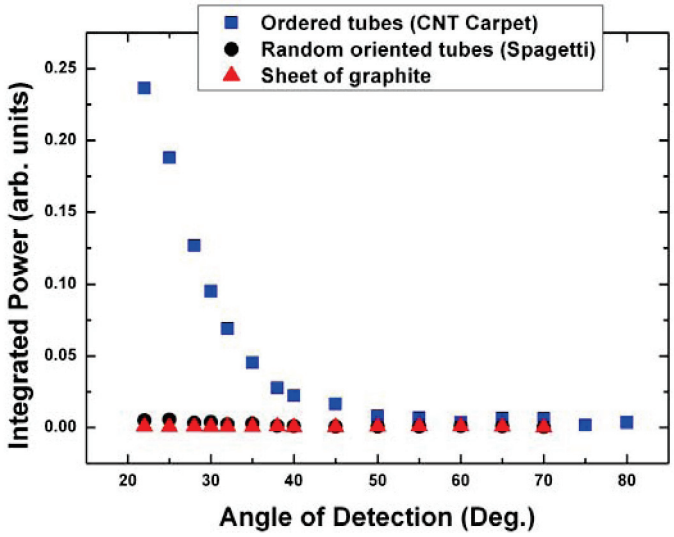


Figure 4.6: Angle dependent reflection measurement at normal incidence comparing the scattering of carbon nanotubes, sheet of graphite and pure metal. The scattering from the nanotubes re significant larger then from the other object.

play a possible role in describing the theory as well including coherent back scattering and weak localization[113–115]. This is though at this point in time still unclear and under further investigation.

The CNT carpet consist of densely packed upright standing 500 mm long CNT rods and compared with a metal plate the surface of the two samples looks very different. One could, even if it at this point is not clear how, imagine that the THz wave is penetrating into the CNT carpet of conductive CNT rods and somehow coherently backscattered in the way the experimental data shows. Since the THz pulse shape looks like the incident THz pulse, one can exclude that multiple scattering paths are giving the rise to the backscattering. A single scattering path would neither give rise to the significant off-angle scattering of the radiation, when excluding

surface roughness issues. One possible explanation to this could be that the scattering is originating from a multiple scattering path that adds up coherently in the backscattering direction. A scattering phenomenon like this would be comparable to coherent backscattering and weak localization theories, but this is unclear at this point in time. To get more reliable data for this theory there is a need to take more data, especially scattering data at small scattering angles (<20 degrees). Our collaborating group at Wright State University have proposed a new setup taking data narrow angle data and sketch of this setup is shown in Fig. 4.7.

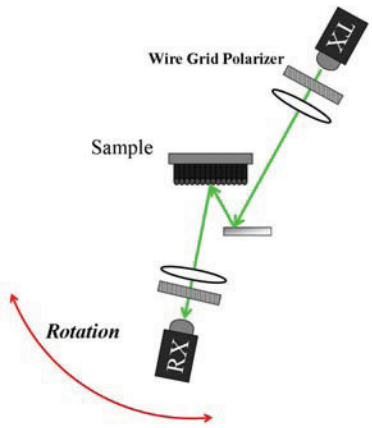


Figure 4.7: Modified THz-TDS system for scattering measurements.

## 4.2 Initial investigation of impurities in carbon nanotubes with THz-TDS

Additional work on a different kind of carbon nanotubes has also been conducted during the stay at Wright State University. The initial interest was to study the interaction of THz waves on carbon nanotube fibers[91, 92], inspired by the work of [88–90], who used THz-TDS to characterize the

frequency dependent refractive index, absorption, and conductivity. The main purpose of our experiments was to investigate the role of impurities/contaminants on the conductivity of the carbon nanotubes using THz-TDS. Figure 4.8 depicts a carbon nanotube fiber under investigation.

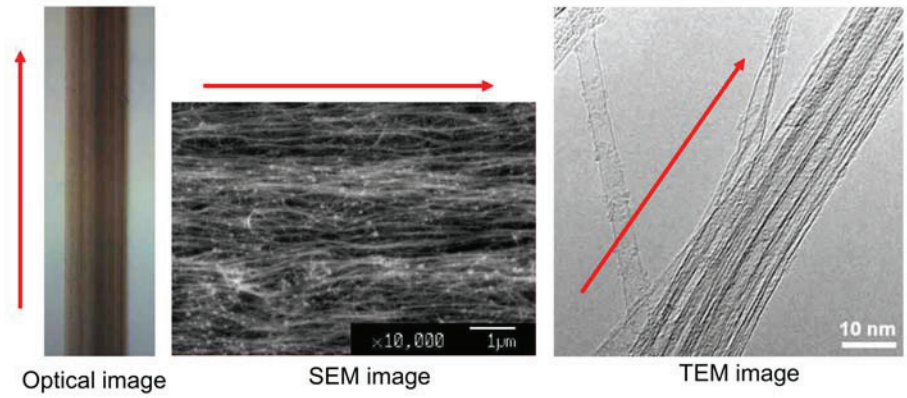


Figure 4.8: Optical, SEM and TEM image of a carbon nanotube fiber aligned to the substrate plane[92]. The arrows indicate the alignment of the nanotubes.

Fig. 4.9 shows THz transmission measurements performed on multi-walled carbon nanotubes (aligned parallel to the substrate plane) [91, 92]. The samples were baked at high temperatures under vacuum conditions in order to remove the effects of water vapor and other contaminants present under ambient conditions. The experimental setup is depicted in Fig. 4.10. Monitoring of the THz transmission in-situ during the baking indicated that the increased transmission was a product of the decreased conductivity of the samples due to impurity removal. The mechanism from this initial data as follows: The transmission through the CNT film increases with higher

temperature, a higher temperature decreases impurities in the CNT and this decreases the conductivity of the tubes.

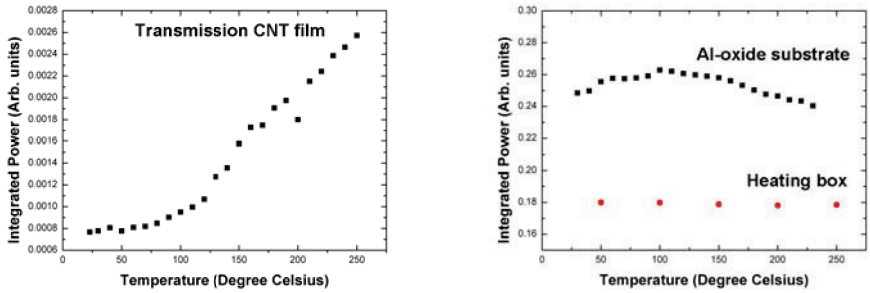


Figure 4.9: (left) Increased THz transmission through the MWCNT sample as it baked under vacuum. (right) Plots of the THz transmission through the sample substrate and the bare box indicating that the increased transmission as a function of temperature in Fig. 4.9(right) is due mainly to the sample.

Fig. 4.9(right) shows that the heating box and the nanotube substrate have independent or opposite temperature vs. transmission characteristics. These results suggest that terahertz spectroscopy merits further investigation into its ability to detect impurity and doping in carbon nanotubes samples. THz-TDS could due to its ability to monitor conductivity possibly be a valuable monitor for impurities in the production of carbon nanotubes. More measurements on this are planned in cooperation with the group providing the nanotubes to follow up on the results from this initial conceptual study.

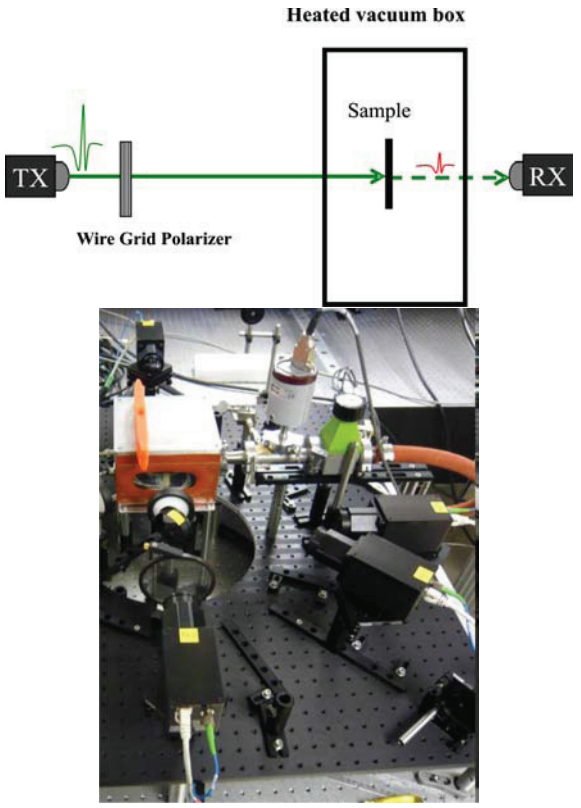


Figure 4.10: Measurements setup used with the CNT film. Measurement box characteristics: Pressure: min. 24 $\mathrm{kN} \cdot \mathrm{m}^{-2}$, low absorbtion and low dispersion TOPAS windows, PID controlled temp. up to 250°C.

## 4.3 Summary

This chapter showed two experiments using a fiber coupled THz-TDS system. Especially the scattering experiments could barely not be conducted without a fiber based system due to the enormous amount of realignment needed when using classical free-space coupled THz emitter and detector

units. Acquiring angle resolved scattering data from various objects is a very good example where a simple, hassle-free measurement instrument is no longer requiring the majority of attention, but the application itself is getting into focus as a result of improved technology and operator usability.

The scattering of pulsed THz waves from a carbon nanotube carpets showed a unexpected significance compared to bulk metal. At normally incident THz radiation on the CNT carpet sample the scattering at a 30 degree detection angle was more that 500 times larger compared to bulk metal. The scattering occurs despite the wavelength of the terahertz radiation being significantly larger than the diameters of the nanotubes. At this point in time it is not understood what is causing the significant scattering and further experiments are planned to correlate the data to some possible theory, among these weak localization and coherent backscattering theories.

Experiments on CNT fibers with a THz-TDS system showed the ability to measure conductivity changes possibly connected to impurities and contamination in the nanotubes fibers. These measurements could be a valuable tools for understanding and monitoring the impurities in CNT fibers.

# Chapter 5

# A broadband multi-element THz imaging system

This chapter presents the work on a broadband multi-element THz imaging system developed under the scope of an European Space Agency (ESA) project Contract No. 21155/07/NL/ST, "Terahertz Camera for Remote Detection of Material Defects and Biological and Chemical Substance". The project work was divided between several project partners, namely, DTU Elektro, DTU Space, SynView GmbH and DTU Fotonik. The work described in this chapter will focus on the work conducted at DTU Fotonik and only give a short overview of the work done by the other partners mainly for understanding the general concepts.

ESA´s main interest is remote stand-off detection of material defect and bonding flaws in for instance spacecraft isolation foam or spectral recognition of chemical substances. More generally this project was used to push the technology in Europe towards a terahertz 'camera' for remote detection.

The main concept of a broadband multi-element THz imaging system is inspired by phased array and synthetic aperture radar imaging systems operating in the microwave range. Combining the large knowledge on data analysis and imaging capabilities of these systems with a new multi-element THz system will give a novel possibility of fast image acquisition avoiding

time consuming raster scanning imaging method.

This system features an in-plane emitter-detector array consisting of 32 emitters and 32 receiver units. The technology used in every single unit is inherited from the standard THz-TDS systems making use of photoconductive switches driven by a femtosecond laser pulse train. A novel concept is the all-fiber pulse delivery network that includes an all-fiber dispersion compensation scheme. By avoiding free-space dispersion compensation units the system wins on robustness which is of great importance making the step from the laser laboratories and towards real life imaging applications.

The work presented in this chapter is state-of-the-art development conducted in the framework of this thesis and is not describing the complete final THz camera in every detail. The ESA THz camera project is, however, at this point in time not finalized yet as the project first will end in March 2010. Apart from this, it needs to be mentioned that the complete ESA project consist of two independent imaging systems, one based on electronic CW THz sources and detectors and the other one based on photonic generation and detection concepts (covered in this text). The basic idea was to merge two different technologies that can support each other in the image acquisition process. The electronic system is operated at around 300 GHz and is designed to acquire images of a larger scene ($1 \times 2$ m), but with a coarser spatial resolution than the photonic based broadband camera system. A larger scene can be covered due to the higher average power obtainable with electronic CW THz sources. The coarser spatial resolution is due to the longer wavelength used. The advantage of the photonic based system is the capability of obtaining broadbanded spectral information of the imaged objects and that the high frequency content in the broadband radiation is improving the spatial resolution.

The theoretical THz generation and detection concepts used for the photonic based pulsed THz imaging concepts have been discussed in chapter 3.

## 5.1 System overview

The photonic part of the ESA THz camera was designed on background of basic requirements from the European Space Agency. The aimed stand-off working distance is at is maximum expected to be 0.5 m due to the low average output power from the photonic THz sources. The scene size should at least be 500×500 mm and the image acquisition speed is aimed to be close to real-time. In order to be able to image moving objects, it is necessary to have a sufficiently short acquisition time, in which it can be assumed that the object is resting. Further should the camera be able to work outside the controlled laboratory environment. The initial requirements for the pulsed broadband system are as indicated in Table 5.1.

| | |
|---|---|
| Stand-off distance [m] | 0.5 |
| Lower operating frequency [GHz] | 300 |
| Upper operating frequency [GHz] | 2000 |
| Scene length [mm] | 500 |
| Scene length [mm] | 500 |
| Imaging Speed | real-time |

Table 5.1: Photonic imaging system parameters

Several iterative concept development rounds taking all technological challenges, like imaging algorithm, emitter/receiver design, pulse distribution, data acquisition etc. into account resulted in a camera design which was validated in computer simulations. Simulations showed that an image of the required quality should be formed by a synthetic aperture in 2D using 32 transmitting × 32 receiving channels where no additional optics is used to direct the THz waves towards the imaging scene. Fig. 5.1 shows the simulation result of the imaging capability of a planar 32 by 32 emitter detector array. 32 receivers are placed in the inner part of the array spaced by 13.3 mm and 32 detectors are placed in the outer part spaced by 80 mm. The system dimensions were chosen to be 400 × 400 mm for the size of the array plane and 300 mm distance to the object plane. The spatial resolution of the configuration was examined using the USAF resolution pattern.

On the upper left side the original object data are displayed and the right hand side shows the reconstructed data. One can depict that structures below 1 mm are nicely reconstructed. Fig. 5.2 highlights the importance of a broad system bandwidth in this imaging array which is one of the main features of the THz-TDS setup.

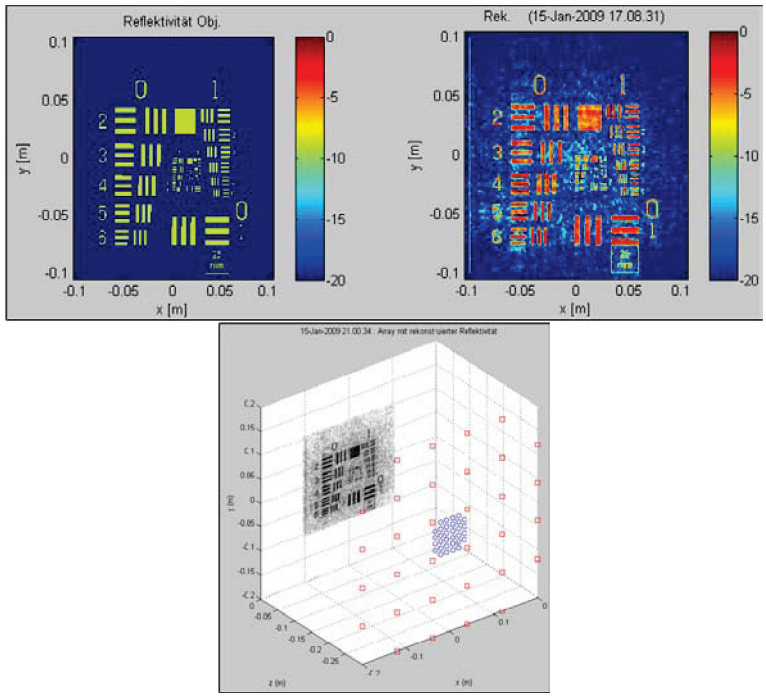


Figure 5.1: Simulation results of a planar 32 by 32 emitter detector array. Rx/Tx arranged in square arrays, 6x6 elements, corners missing (32 elements each). The receivers (blue dots) are placed in the inner array spaced by 13.3 mm and the detector (red squares) in the outer spaced by 80 mm. The system bandwidth is 100-1000 GHz. Courtesy of Synview (www.synview.de).

The more detailed system design is shown in Fig. 5.3 and this takes

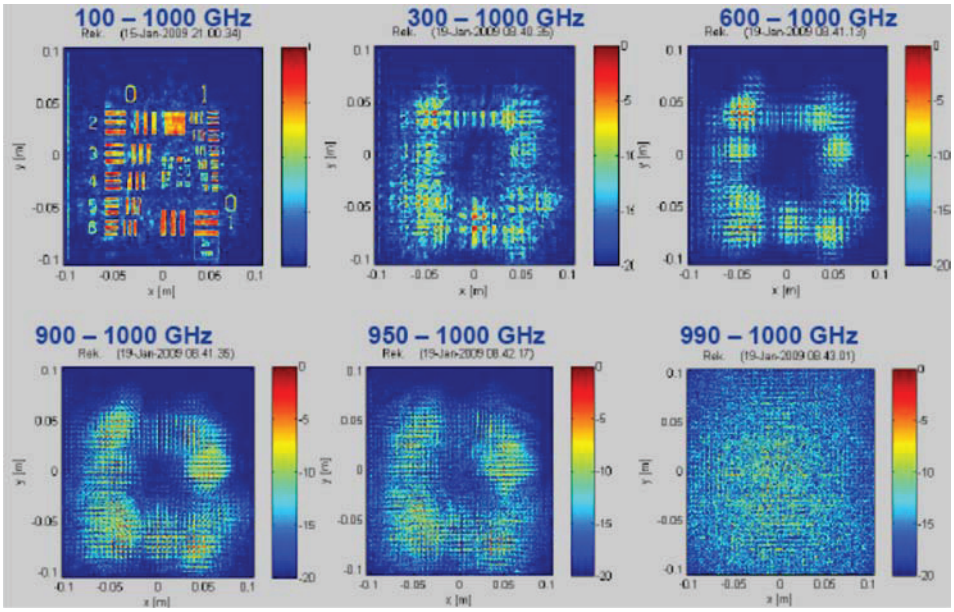


Figure 5.2: Simulation results of the imaging capability of the geometry shown in Fig. 5.1 at various system bandwidths. Courtesy of Synview (www.synview.de).

background in the design guidelines obtained by the simulation results shown above. The design contains an optical part and an electronic part. The optical part of the system includes an advanced dual-femtosecond fiber laser, a fiber distribution system with dispersion control, and the 2D array of 32 individual THz emitters and 32 individual THz detectors. The electronic part of the system delivers the required control voltages to the THz emitters and reads out the THz signals from the detectors for further processing in the data acquisition hardware and software. Fig. 5.3 shows an outline of the most principal components of the optical as well as the electronic part of the photonic imaging system.

The design that will be presented in the following is based on a simple

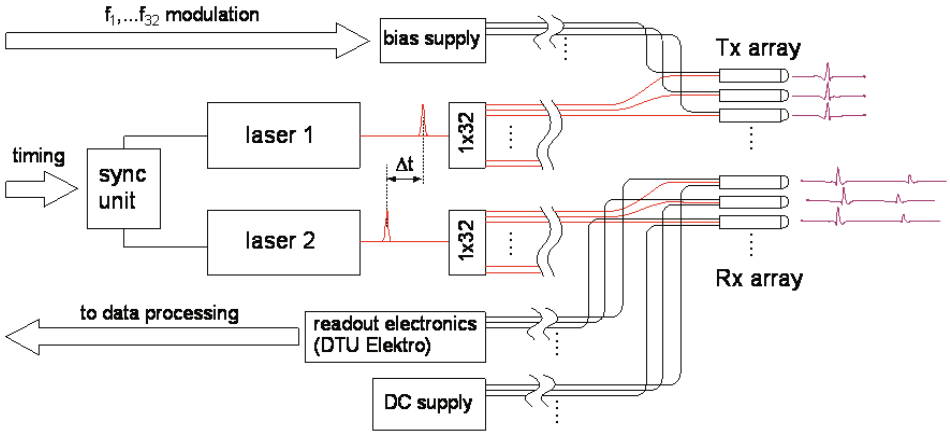


Figure 5.3: Complete photonic THz imaging system, including electronic components. The thick arrows indicate communication with the data acquisition back-end.

strategy, namely to minimize the amount of moving parts in the system. The most important places where this strategy has played a defining role is in the choice of:

- a **fiber-based femtosecond laser system** to drive the THz antennas,
- a **variable time delay** with no moving mirrors between the two femtosecond beams responsible for generation and sampling, respectively, of the THz signals,
- an **all-fiber dispersion compensation** scheme that will be employed to ensure ultrafast, femtosecond laser pulses at the THz antennas,
- an **all-fiber distribution** subsystem that will be employed to distribute the femtosecond pulses from the lasers to the 64 THz antennas,

- a **butt-coupling** of each optical fiber to the individual THz antennas.

## 5.2 Theory of pulse delivery via fiber link

This section will introduce the theoretical background needed for the understanding of propagation of short pulses in optical fibers. The propagation of ultrafast laser pulses in optical fibers is described by considering the linear propagation effects, including linear attenuation, group velocity dispersion and third-order dispersion, as well as the nonlinear propagation effects, including the Kerr effect, stimulated Raman scattering, and self-steepening. In the following we will describe the basic formalism of linear pulse propagation, introduce nonlinear effects in the propagation, and combine these effects into the well-known nonlinear Schrödinger equation that describes pulse propagation in a nonlinear medium.

### Linear propagation effects

The basis of the description of linear pulse propagation is the propagation constant $\beta$ which determines the accumulated phase after propagation of a distance $z$,

$$E(\omega, z) = E(\omega, 0) \exp(i\beta z) \ . \tag{5.1}$$

The propagation constant is related to the effective index of refraction at the frequency $\omega$ through

$$\beta(\omega) = \frac{n_{eff}(\omega)\omega}{c} \ , \tag{5.2}$$

where $n_{eff}$ often is found by an eigenmode analysis of the propagation characteristics of a given optical fiber [54].

For femtosecond pulses in the 100-fs range, with a narrow spectral pulse bandwidth, $(\omega - \omega_0) \ll \omega_0$, it is justified to employ a Taylor expansion of the frequency-dependent propagation constant in the vicinity of the central frequency $\omega_0$ of the laser pulse,

$$\beta(\omega) = \beta(\omega_0) + \beta_1(\omega - \omega_0) + \frac{1}{2}\beta_2(\omega - \omega_0)^2 + \frac{1}{6}\beta_3(\omega - \omega_0)^3 + \dots \ , \quad (5.3)$$

where the coefficients $\beta_n$ are the $n$-th order derivatives of the propagation constant at a central frequency,

$$\beta_1 = \left.\frac{\partial\beta}{\partial\omega}\right|_{\omega=\omega_0} , \quad (5.4)$$

$$\beta_2 = \left.\frac{\partial^2\beta}{\partial\omega^2}\right|_{\omega=\omega_0} , \quad (5.5)$$

$$\beta_3 = \left.\frac{\partial^3\beta}{\partial\omega^3}\right|_{\omega=\omega_0} . \quad (5.6)$$

The coefficient $\beta_1$ is related to the group velocity of the pulse propagating though the fiber as $\beta_1 = 1/v_g$.

The dispersive properties of optical fibers are often characterized by the dispersion parameter $D$ related to the second derivative of the propagation constant,

$$D(\lambda) = -\frac{2\pi c}{\lambda^2}\beta_2 \ . \quad (5.7)$$

The dispersion parameter is in units of s/m$^2$, and is often reformulated into units of ps/nm/km, describing the amount of pulse broadening per nanometer bandwidth of the pulse and per kilometer propagation distance.

The dispersion parameter is a function of frequency, or wavelength. The wavelength dependence of $D$ is typically rather linear within the bandwidth of a 100-fs laser pulse, and therefore the dispersion slope $S = \partial D/\partial\lambda$ is used as an additional parameter to describe pulse propagation. If we assume that $S$ is independent of the wavelength within the bandwidth of the pulse then the wavelength dependence of the dispersion parameter can be written as

$$D(\lambda) = D_0 + S_0(\lambda - \lambda_0) \ , \quad (5.8)$$

where $D_0 = D(\lambda_0)$ and $S_0 = S(\lambda_0)$ are the values of the dispersion parameter and the dispersion slope, respectively, at the central wavelength of the

pulse. This relation can also be expressed as function of frequency,

$$D(\omega) = D_0 - 2\pi c S_0 \left(\frac{\omega - \omega_0}{\omega\omega_0}\right) \approx D_0 - 2\pi c S_0 \left(\frac{\omega - \omega_0}{\omega_0^2}\right) \tag{5.9}$$

where the approximation is valid in the vicinity of the central frequency.

We can relate $D_0$ and $S_0$ to the expansion coefficients of the propagation constant,

$$D_0 = -\frac{2\pi c}{\lambda_0^2}\beta_2 \ , \tag{5.10}$$

$$S_0 = \left(\frac{2\pi c}{\lambda_0^2}\right)^2 \beta_3 + \frac{4\pi c}{\lambda_0^3}\beta_2 \ . \tag{5.11}$$

With these relations we can express the expansion coefficients of the propagation constant as

$$\beta_2 = -\frac{\lambda_0^2}{2\pi c} D_0 = -\frac{2\pi c}{\omega_0^2} D_0 \ , \tag{5.12}$$

$$\beta_3 = \left(\frac{\lambda_0^2}{2\pi c}\right)^2 \left(S_0 + \frac{2D_0}{\lambda_0}\right) = \left(\frac{2\pi c}{\omega_0^2}\right)^2 \left(S_0 + \frac{\omega_0 D}{\pi c}\right) \ . \tag{5.13}$$

If these expressions for the expansion coefficients are inserted in equation 5.3 we obtain an expression for the propagation constant of the form

$$\beta(\omega) = \frac{1}{v_g}(\omega - \omega_0) - \frac{\pi c D}{\omega_0^2}(\omega - \omega_0)^2 + \frac{2}{3}\left(\frac{\pi c}{\omega_0^2}\right)^2 \left(S + \frac{\omega D}{\pi c}\right)(\omega - \omega_0)^3 + \ldots \tag{5.14}$$

### Nonlinear Schrödinger equation

The standard method for describing the propagation of a laser pulse in a medium is to separate the carrier wave and the pulse envelope. Then the propagation can be described by the dynamics of the slowly varying pulse envelope $u(z,t)$ in the reference frame moving along with the pulse at the group velocity, $t = t' - z/v_g$ where $t'$ is the physical time. This assumes that

the electric field propagates in the positive $z$-direction. If we further assume that the field is polarized in the $x$ direction and use a scalar representation then the differential equation governing its propagation is [54]

$$\frac{\partial u}{\partial z}+\frac{\alpha}{2}u+i\frac{\beta_2}{2}\frac{\partial^2 u}{\partial t^2}-\frac{\beta_3}{6}\frac{\partial^3 u}{\partial t^3}+\ldots = i\gamma\left(|u|^2u+i\frac{t_0}{2\pi}\frac{\partial(|u|^2u)}{\partial t}-T_Ru\frac{\partial(|u|^2)}{\partial t}\right). \tag{5.15}$$

This differential equation is generally known as the nonlinear Schrödinger equation (NLSE). The expansion coefficients $\beta_2$ and $\beta_3$ can be expressed in terms of experimental measured dispersion parameters $D_0$ and $S_0$ and the propagation of a given input pulse $u(t)$ through an optical fiber with an effective modal area $A_{eff}$ can be calculated to great accuracy using the NLSE. The expansion coefficient $\beta_1 = 1/v_g$ cancels out in the differential equation since we have chosen a reference frame moving with the group velocity. The nonlinear terms describe the Kerr effect, self-steepening, and stimulated Raman scattering. $T_R$ in equation 5.15 represents the Raman response. The nonlinear parameter $\gamma$ is defined as

$$\gamma = \frac{2\pi n_2}{A_{eff}\lambda_0} = \frac{n_2\omega_0}{cA_{eff}} \tag{5.16}$$

where $n_2$ is the nonlinear, intensity-dependent index of refraction. For silica glass, $n_2 = 2.6 \cdot 10^{-20}$ m$^2$/W.

The dimensions of each term in the NLSE must of course be the same. Comparing the first term on the right-hand side with the first term on the left-hand side of equation 5.15 we see that the dimensions of $\gamma|u|^2$ must be the same as the dimensions of $\partial/\partial z$. Since $\gamma$ has dimensions W$^{-1}$m$^{-1}$ and $\partial/\partial z$ has dimensions m$^{-1}$ then $|u|^2$ must be given in units of W, and hence $u$ is in units of W$^{1/2}$. The function $u(z,t)$ is thus not directly the electric field, but rather proportional to the electric field, with magnitude equal to the square root of the instantaneous power. The initial field $u(0,t)$ must be normalized so that

$$U_0 = \int_{-\infty}^{\infty}|u(0,t)|^2dt \tag{5.17}$$

where $U_0$ is the energy of the laser pulse.

In the following we will assume that the input laser pulse can be estimated to have the gaussian-shaped in time,

$$u(0,t) = \sqrt{P_0}\exp\left(-\frac{1}{2}(1+iC)\frac{t^2}{\tau^2}\right) \tag{5.18}$$

where $\tau = FWHM/2\sqrt{\log 2}$ is the width of the pulse, defined in terms of $FWHM$, the full-width-at-half-maximum duration of the laser pulse. The parameter $C$ is the dimensionless chirp parameter, that expresses the length of the pulse with respect to a transform-limited pulse - e.g. a 100-fs pulse stretched to around 1 ps has $C = +10$ if the chirp is positive (due to anomalous dispersion) and $C = -10$ if the chirp is negative (due to normal dispersion).

The NLSE is typically solved using the symmetrized split-step Fourier transform method. Several software packages are available for this purpose. The package `SSPROP` from T. E. Murphy and colleagues from the Photonics Research Laboratory at the University of Maryland [116] is a fast and easy-to-use complete package for Matlab that uses the symmetrized split-step Fourier transform method to solve the NLSE. The simulations presented in the following are performed with this software.

## 5.3 Frequency resolved optical gating (FROG) technique

We use a home-build second-harmonic generation frequency optical gating (SHG-FROG) setup in our experiments to characterize the ultrashort laser pulses and to validate the quality of the numerical simulations and optimize the fiber link. Compared to other ultrashort pulse characterization methods the FROG technique does not only determine the pulse duration and the pulse intensity, but can also recover the full time dependent electrical field of the input pulse. R. Trebino and his group at Georgia Tech pioneered this technique [117–119].

A typical FROG setup is similar to that of an intensity autocorrelator but the photodiode that is typically used in the autocorrelator is replaced

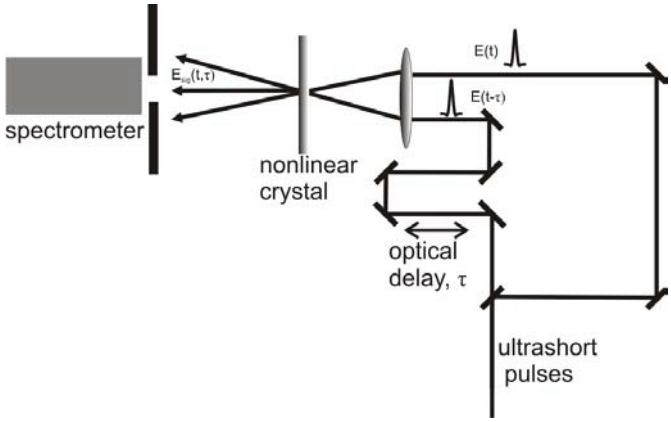


Figure 5.4: Sketch of the SHG-FROG measurement setup. The mixing product of the two pulses is detected in the spectrometer as a function of time delay difference between the two beam paths.

by a spectrometer (Fig. 5.4). For every arrival time difference between the two pulses a full frequency spectrum is measured. The data is typically plotted in a spectrogram which is a plot of the intensity as a function of time and frequency (or wavelength). This can be expressed as

$$I_{sig}^{SHG}(\omega,\tau) = \left| \int_{-\infty}^{\infty} E(t)E(t-\tau)e^{-i\omega t}dt \right|^2, \tag{5.19}$$

where $E(t)$ is gated by a delayed version of itself $E(t-\tau)$ inside the nonlinear crystal. This technique is very sensitive, though phase matching issues have to be taken into account when choosing the nonlinear crystal (thinner crystal more bandwidth). A thin crystal has a broader SHG phase matching bandwidth than a thick crystal. We use a 0.13 mm BBO crystal which has a reasonable flat conversion efficiency over 50 nm. By employing a iterative FROG retrieval algorithm one can from the measured FROG spectrogram reconstruct the amplitude and phase of the electric field of input pulse.

## 5.4 Pulsed femtosecond laser source

The choice of the laser system is intimately linked to the choice of the temporal delay control between the generation and sampling femtosecond laser beams that will be implemented. We have chosen the dual femtosecond fiber-based laser system from Toptica (Fig. 5.5). This system includes the technical specifications required for the imaging system, and offers the possibility of electronically controlled optical sampling (ECOPS), which will be described later in this section. All laser pulses were measured and retrieved by the FROG technique and the retrieved pulses are also compared to the measured intensity autocorrelation.


Figure 5.5: Dual-laser FFS femtosecond laser system from Toptica. Left image shows an inside view of one of the two lasers. Right image shows the two lasers on an optical table. The laser in front will drive the 32 THz detectors and the laser in the back will drive the 32 THz emitters.

### Description of femtosecond fiber laser

The two femtosecond lasers are locked to the same repetition rate by active control of the cavity length of one of the two lasers. The complete laser system chosen for the photonic imaging system consists of the two

femtosecond lasers (FFS.SYS and FFS.SYS.HP), their power supplies, the synchronization electronics (FFS.SYNC) and a laptop PC for control of the system via an USB interface. The laser system is operational within 30 seconds after switch-on, with no alignment procedure.

The lasers have the specifications shown in Table 5.2.

In the originally delivered laser system the laser pulses are coupled into free space from a fiber end-facet using a lens to a free-space prism setup for dispersion control, and subsequently the pulses are delivered from the output port of the laser system. The output pulses have been onto specs. as seen in Table 5.2. We have customized the laser system so that it is optimized for the fiber delivery. Instead of the free-space element in the standard laser systems we have removed the dispersion control and spliced the output fiber of the laser systems directly onto the fiber link. In this way we assure a near-perfect pulse energy budget, increase the stability of the whole system considerably, and reduce the risk of damage to the optics due to the high peak power. The output pulse length directly out of the fiber, before the compressor, is in the ps range rather than in the 100 fs range after the prism compressor. Fig. 5.6 depict the FFS.SYS laser before and after customization.

### Pulse characteristic of laser source

The output of the two Toptica lasers is characterized with the FROG technique. The retrieved pulse is then used as input pulse in the pulse propagation algorithm. Fig. 5.7 shows a spectrogram of the direct output of FFS.SYS (laser 1), obtained in a FROG measurement and retrieved by the FROG phase retrieval algorithm. We see good agreement between the measured and the retrieved pulse spectrogram and from the retrieved pulse spectrogram the retrieved pulse intensity and phase and the autocorrelation is extracted (Fig. 5.8). The pulse length of FFS.SYS(laser 1) at the fiber output can be determent to 0.9 ps.

| **Parameters** | **FFS.SYS (laser 1)** | **FFS.SYS.HP (laser 2)** |
|---|---|---|
| Output power | 250 mW | 350 mW |
| Output power at end of output fiber | 293 mW | 425 mW |
| RMS noise on power | <0.1% | <0.1% |
| Repetition rate | 90.272 MHz | 90.272 MHz |
| Pulse energy | 2.5 nJ | 3.9 nJ |
| Pulse energy at end of output fiber | 3.25 nJ | 4.7 nJ |
| Beam profile | TEM00 | TEM00 |
| Beam divergence | < 1 mrad | < 1 mrad |
| Polarization | Linear, horizontal | Linear, horizontal |
| Wavelength | 1550 nm | 1550 nm |
| Pulse length | 110 fs | 120 fs |
| Pulse length at end of output fiber | 0.9 ps | 1.0 ps |
| Relative time jitter | - | 60-80 fs (typical) |
| Operational voltage | 230 V | 230 V |
| Dimensions ($w \times h \times d$) | $318 \times 122 \times 236\ mm^3$ | $576 \times 122 \times 236\ mm^3$ |

| | **FSS.SYNC (sync unit)** |
|---|---|
| Relative time jitter | 60-80 fs |
| Repetition rate change | > 200 kHz |
| Piezo transducer resonance frequency | > 5 kHz |
| Temporal sweep rate | > 100 Hz (100 ps range) |
| Control voltage | 1 V/ns, max 10 V |

Table 5.2: Laser specifications

### Pulse compression in single-mode fiber

The high peak power directly out of the fiber laser will due to dispersion and nonlinear effects (especially self-phase modulation) not be able to propagate very far in standard single-mode fiber before it is compressed to its minimum pulse length. In the absence of a dispersion compensating scheme will the pulse be compressed to its minimum before reaching the $1\times32$ splitter. A Gaussian input pulse ($\tau_{FWHM} = 1$ ps, $C = -10$ and a pulse energy of $E_{pulse} = 2.8$ nJ) is compressed to its minimum pulse length of 29 fs after 930 mm of standard single-mode fiber as shown in Fig. 5.9. After passing the 930 mm full compression point nonlinear effects as SPM take over. This

is seen in as splitting of the pulse into a double pulse structure. To obtain a practical useful fiber link length which can reach the sensor heads and to protect the splitter from the high peak power of a fully compressed pulse, the pulse has to be stretched in the very first section of the fiber link. The design of the fiber link will be addressed in detail in section 5.5.

### Optical Delay control

The optical delay control defines the timing of the arrival of the femtosecond laser pulses to the THz emitter antennas and to the THz detector antennas, respectively. One of the main purposes of the dual femtosecond laser system is to implement an accurate and fast electronically controlled delay between the two pulse trains. The principle of the Electronically Controlled Optical Sampling (ECOPS) is shown in Fig. 5.10. The two lasers FFS.SYS and FFS.SYS.HP are locked to the same repetition rate (approximately 90 MHz) by the FFS.SYNC synchronization unit, implemented by a standard PID feedback loop to a piezo-driven end mirror in one of the laser cavities.

A small perturbation to the actively controlled laser cavity results in a subsequent temporal shift of one of the pulse trains, as shown in Fig. 5.10. This perturbation is introduced by applying an additional voltage pulse to the piezo-driven end mirror of the cavity, resulting in a slightly longer or shorter cavity length. If the perturbation is of short duration, i.e. only slightly longer than the cavity round-trip time, then the result of the perturbation is a constant time shift of one beam with respect to the other. The electronics of the FFS.SYNC unit is designed to set the temporal delay between the two laser outputs based on a DC input voltage. This means that a simple input ramp voltage controls the delay between the two pulse trains. The sweep rate of the voltage ramp will be set to match the bandwidth of the data acquisition system. A typical sweep can be carried out at a speed of 10 ps/ms, resulting in a full scan of a 100-ps time window at a rate of 100 Hz.

## 5.5 Design of fiberlink

The femtosecond pulse trains will be delivered via an all-fiber distribution link from the laser system to the individual THz antennas. In this section we will specify the optical fibers involved in this link and present numerical simulations and FROG measurements of the propagation of femtosecond laser pulses through a fiber link. For the simulation we use the symmetrized split-step Fourier transform method, including third-order dispersion and nonlinear propagation effects to assure accurate simulation of the fiber link.

With this all-fiber solution from laser to each THz antenna a reproducible power budget is possible, and the design is very rugged with respect to external vibrations and temperature fluctuations. Due to the all-fiber design no additional alignment is needed of the fiber link.

### Design strategy

In order to handle the high peak power of the compressed femtosecond pulse it is essential that the pulse remains rather long throughout as large a fraction of the fiber link as possible. We obtain this a by further stretching of the output from the fiber lasers ($\approx$ 1 ps) to a duration of 2 – 3 ps by the use of a dispersion compensating fiber (OFS Fitel extra-wide-band DCF). The stretched pulse is then coupled into a section of standard single-mode fiber (Corning SMF- 28) which in turn is connected to the fiber power splitter. After the power splitter, a length of SMF-28 is again attached, and at a suitable distance the fiber link is terminated. At this point the output pulse is compressed to sub-100 fs and is ready for delivery onto the THz chips. The SMF-28 can be directly spliced to the power splitter input. The power splitter also uses SMF-28 so the loss will be negligible. The loss is less than 0.02 dB per splice throughout the system except for the splice to DCF which is 0.6 per splice because of the mode-mismatch between DCF and SMF.

The length of the dispersion compensation fiber in a low power system is chosen so that the total dispersion of the fiber link is zero, according to

$$D_{tot}L_{tot} = D_{DCF}L_{DCF} + D_{SMF}L_{SMF,1} + D_{1\times32}L_{1\times32} + D_{SMF}L_{SMF,2} = 0 \tag{5.20}$$

where $D_{DCF}L_{DCF}$ denotes the product of the dispersion parameter for DCF fiber and the DCF fiber length, $D_{SMF}L_{SMF,1}$ is the product of the dispersion parameter for SMF fiber and the length of fiber section 1, $D_{1\times32}L_{1\times32}$ the dispersion parameter of the $1 \times 32$ splitter and the length inside the splitter and $D_{SMF}L_{SMF,2}$ is the product of the dispersion parameter of SMF and the length of fiber section 2. The shortest pulse duration is ensured if not only the effective dispersion parameter $D_{tot}$ vanishes for the total fiber link, but also the slope $S_{tot}$ of the dispersion parameter needs to be balanced [120],

$$S_{tot}L_{tot} = S_{DCF}L_{DCF} + S_{SMF}L_{SMF,1} + S_{1\times32}L_{1\times32} + S_{SMF}L_{SMF,2} = 0 \tag{5.21}$$

Since the slope of the dispersion of e.g. SMF-28 is positive the slope of the DCF must be negative. The important quantity for a zero-dispersion-slope system is that the relative dispersion slope (RDS) of the compensating fiber is the same as the RDS of the rest of the fiber link. RDS is defined as the ratio between the dispersion slope to the dispersion:

$$RDS = \frac{S}{D} \tag{5.22}$$

However, this gives though only an estimate for the fiber link since the nonlinear effect as SPM contribute additionally.

### Dispersion parameters for selected fibers

Standard single-mode fiber displays anomalous dispersion at 1550 nm. Specialty fibers are available that can compensate the dispersion of standard single-mode fibers.

Table 5.3 and 5.4 show dispersion parameters, dispersion slopes and RDS for several fibers with anormalous dispersion (D > 0) and for several dispersion-compensating fibers. Comparison of these fiber types show

Table 5.3: Dispersion parameters for various fiber types with anomalous (positive) dispersion at 1550 nm, in part adapted from [120].

| Fiber type | $D_0$ [ps/nm/km] | $S_0$ [ps/nm$^2$/km] | RDS [1/nm] | $A_{eff}$ [$\mu$m$^2$] | $\gamma$ [$10^{-3}$ W$^{-1}$m$^{-1}$] |
|---|---|---|---|---|---|
| SSMF[a] | 17.2 | 0.059 | 0.0034 | 82 | 1.29 |
| TrueWave® REACH[a] | 7.1 | 0.042 | 0.0058 | 55 | 1.91 |
| TeraLight[b] | 8 | 0.058 | 0.0073 | 63 | 1.67 |
| TrueWave® RS[a] | 4.5 | 0.045 | 0.010 | 52 | 2.03 |
| ELEAF fiber[a] | 4.2 | 0.085 | 0.020 | 72 | 1.46 |
| NL-1550-POS-1[c] | 1.2 | 0.0017 | 0.0014 | 2.8 | 37.6 |
| LMA-35[c] | 25 | 0.07 | 0.0028 | 530 | 0.199 |

[a] fiber from Corning
[b] Fiber from Alcatel
[c] Fiber from Crystal Fiber, A/S

Table 5.4: Dispersion parameters for various fiber types with normal (negative) dispersion at 1550 nm, in part adapted from [120].

| Fiber type | $D_0$ [ps/nm/km] | $S_0$ [ps/nm$^2$/km] | RDS [1/nm] | $A_{eff}$ [$\mu$m$^2$] | $\gamma$ [$10^{-3}$ W$^{-1}$m$^{-1}$] |
|---|---|---|---|---|---|
| standard DCF[a] | -100 | -0.23 | 0.0023 | 20 | 5.27 |
| EWB-DCF[a] | -120 | -0.44 | 0.0037 | 21 | 5.02 |
| HS-DCF[a] | -95 | -0.65 | 0.0065 | 15 | 7.03 |
| EHS-DCF[a] | -120 | -1.2 | 0.010 | 14 | 7.53 |
| UHS-DCF[a] | -130 | -2.1 | 0.016 | 14 | 7.53 |
| NL-1550-NEG-1[b] | -0.5 | +0.014 | -0.028 | 2.8 | 37.6 |

[a] fiber from OFS Fitel
[b] Fiber from Crystal Fiber A/S

that the RDS of a standard SMF-28 from Corning is compensated rather efficiently by the EWB-DCF from OFS. Based on this we have chosen the EWB-DCF fiber from OFS in combination with standard SMF-28 for the dispersion compensation in the fiber link.

## Fiber link simulations

Fig. 5.12 shows the design approach we will use to deliver short pulses between the fiber laser and the emitter. The aim of the simulations is to validate the design concept and to determine the total fiber length of the last piece of SMF (section IV) needed to re-compress the pulse.

Table 5.5 summarizes the composition and the fiber parameters of the fiber link design approached (see Fig. 5.12). (Section I) is a short section of single-mode fiber needed to couple into the dispersion-compensating fiber. (Section II) is the DCF that stretches the input pulse to a duration of a few picoseconds. (Section III) is an intermediate section between the DCF and the power splitter and (section IV) is the output part of the power splitter and a length of standard single-mode fiber that recompresses the pulse to its minimum duration.

Table 5.5: Design parameters of the fiber link.

| **Parameter** | **section I St. SMF** | **section II EWB-DCF** | **section III St. SMF** | **section IV St. SMF** |
|---|---|---|---|---|
| $L_{sec}$[a] [m] | 0.38/0.38 | 0.56/0.56 | 0.93/0.93 | 1.0+SMF/1.0+SMF |
| $A_{eff}$ [$\mu$m$^2$] | 82 | 21.9 | 82 | 82 |
| Coupling loss [dB] | 0.63 | 0.01 | 16.5 | 0.1 |
| Average power[a] [mW] | 293/425 | 254/369 | 5.70/8.27 | 5.57/8.08 |
| $D_0$ [ps·nm$^{-1}$km$^{-1}$] | 17.2 | -119.5 | 17.2 | 17.2 |
| $S_0$ [ps·nm$^{-2}$km$^{-1}$] | 0.059 | -0.41 | 0.059 | 0.059 |
| $RDS$ [nm$^{-1}$] | $3.43 \cdot 10^{-3}$ | $3.43 \cdot 10^{-3}$ | $3.43 \cdot 10^{-3}$ | $3.43 \cdot 10^{-3}$ |
| $\gamma$ [W$^{-1}$m$^{-1}$] | $1.29 \cdot 10^{-3}$ | $4.81 \cdot 10^{-3}$ | $1.29 \cdot 10^{-3}$ | $1.29 \cdot 10^{-3}$ |
| $\beta_2$ [ps$^2$] | -0.022 | 0.152 | -0.022 | -0.022 |
| $\beta_3$ [ps$^3$] | $1.32 \cdot 10^{-4}$ | $-9.12 \cdot 10^{-4}$ | $1.32 \cdot 10^{-4}$ | $1.32 \cdot 10^{-4}$ |

[a] First number is the 293-mW link to the detectors, second number is the 425-mW link to the emitters

We used the NLSE to propagate the pulse at 293 mW and 425 mW average input power through the fiber link design. The input pulse used in the numerical simulations is mainly the retrieved pulse from section 5.4 to get precise knowledge of pulse phase (chirp) and intensity. The Gaussian pulse ($\tau_{FWHM} = 1$ ps, $C = -10$) is used for the first conceptual numerical

simulations, thus, it is only a qualified approximation to the real input pulse.

We will show the main part of the results only for the 293 mW simulation, since the 293 mW and the 425 mW regime generally follow the same compression principles and further was the experimental data available for the 293 mW simulation. The numerical simulations of the high power link will only be shown with the Gaussian input pulse to show that the concept is also valid for the 425 mW link.

Fig. 5.13 shows an overview of the temporal profile of the pulse during propagation through 293 mW fiber link design. The density plots show the power on a logarithmic scale, in units of dBm. The abrupt change in intensity at $z = 1900$ mm is caused by the power splitter which reduces the power by 16.5 dB. The diagrams show that at a certain distance ($z = 5570$ mm) the pulse is re-compressed to the shortest duration($\tau_{FWHM} = 94$ fs). At this point the fiber link will be terminated and contacted to the THz antenna. The first section of the link correctly disperses the pulse to several ps duration, and hence nonlinear propagation effects are minimized through the power splitter.

Fig. 5.14 shows the pulse intensity and the linear phase indicating that the pulse is close to fully compressed at $z = 5570$ mm.

To validate the compression principle also for the high power FFS.SYS.HP (laser 2), we increase the Gaussian pulse energy to $E_{puls} = 4.7$ nJ (corresponding to an average power of 425 mW) and keep the pulse width of 0.9 ps and $C = -10$ as in the previous case. Fig. 5.15 shows the same overview of the temporal profile of the pulse during propagation for the 425 mW fiber link. The pulse has a compressed FWHM minimum at 81 fs at $z = 5340$ mm. Figure 5.16 depicts the magnified view of the simulation using 293 mW input power and 425 mW, respectively. As expected reaches the 425 mW its minimum pulse duration earlier than the 293 mW link due the power enhanced compression in the SMF fiber, but generally can we conclude that the two system are operating in the same regime, meaning that the high pulse energy system is not suffering from nonlinearity issues that not can be compensated for in the fiber link scheme.

However, by comparing the numerical pulse propagations of a Gaus-

sian input pulse in Fig. 5.13 and Fig. 5.15 to a pulse propagation of the measured input pulse from the FFS.SYS(laser 1) depicted in Fig. 5.17, we see an evident difference between the two plots. One major difference is that numerous side peak are appearing, which can be assigned to the much more complex structure of the input pulse. Further the position and the pulse width of the optimal compression position changed. The pulse in the pulse propagation simulation depicted in Fig. 5.17 can be compressed to a FWHM pulse width of 101 fs at $z = 5450$ mm and has hence changed by 120 mm compared to the Gaussian input pulse simulation. After the point of shortest duration the pulse shape re-broadens due to the anomalous dispersion in the SMF and due to SPM originating from the high peak power. Hence it is important to terminate the fiber link at the correct point before this reshaping happens. Fig. 5.18 shows the more complex compressed pulse intensity and phase.

Fig. 5.19 shows a magnified view of the region of the shortest possible pulse. The design compresses the pulse to its shortest duration at approximately 5450 mm total length of the fiber link at a more complex pulse structure.

A different picture of the pulse propagation along the fiber is obtained by looking at the autocorrelation of the pulses as a function of fiber length. We can use the autocorrelation to compare directly with the experimental data obtained in the fiber link measurements. Fig. 5.20(top) depict the zoomed view of the minimum pulse width area. Fig. 5.20(bottom) shows the autocorrelation of the shortest pulse length at $z = 5450$ mm which has a autocorrelation FWHM of 135 fs.

The simulations above indicate that the duration of the pulse after the link can be considered to be in the region of sub-100 fs, by far sufficient to ensure the desired bandwidth from the THz antennas.

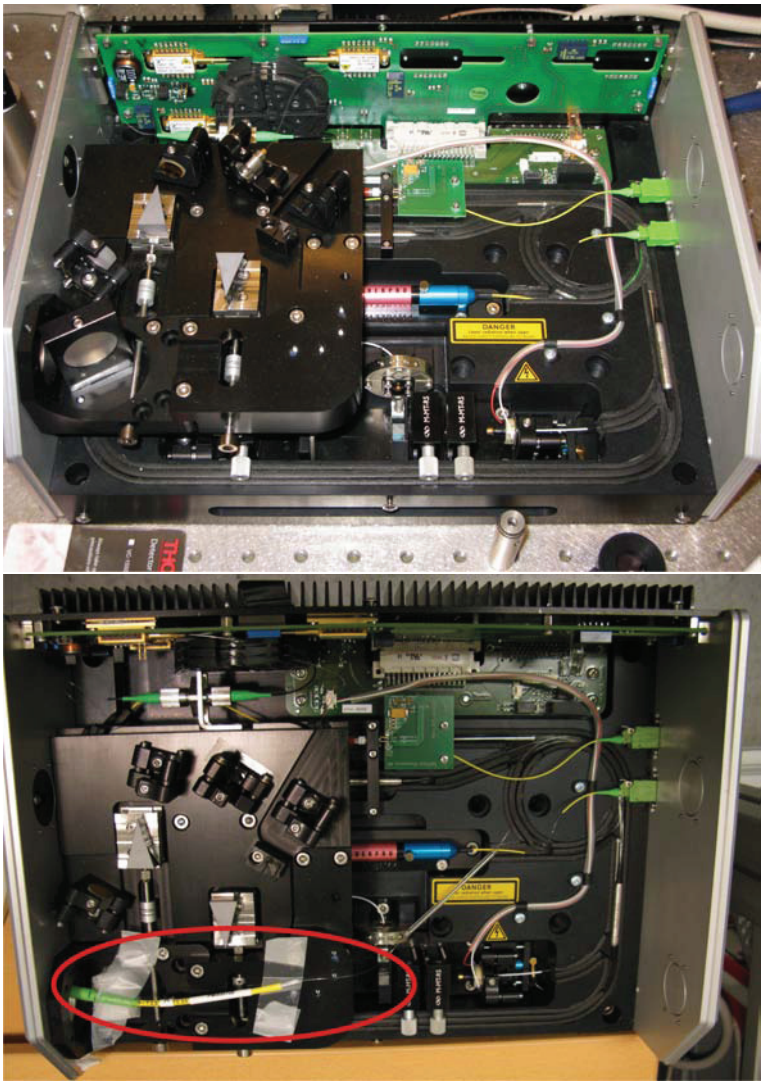

Figure 5.6: (top) FFS.SYS laser before rerouting of the prism-compressor. The output pulse length was measure to 110 fs. (bottom) The prism-compressor is now rerouted and the original free-space output coupler removed and replaced by an APC/FC-connector. The connector was fusion spliced onto the fiber laser output. The output pulse length directly out of the fiber connector is measured to 0.9 ps and the output power increased by approximately 25%.

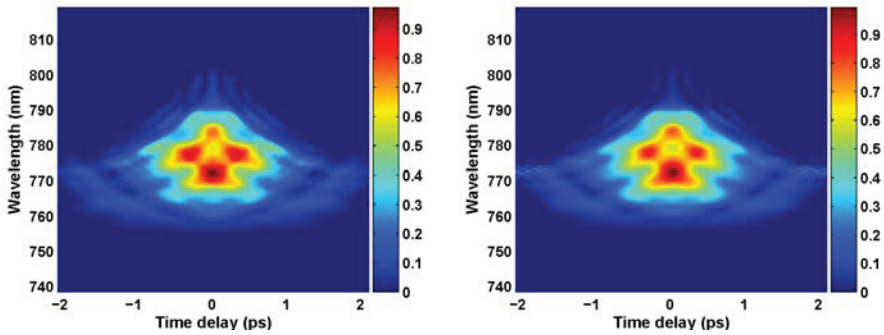


Figure 5.7: FROG spectrograms of the measured and the phase retrieved pulse.

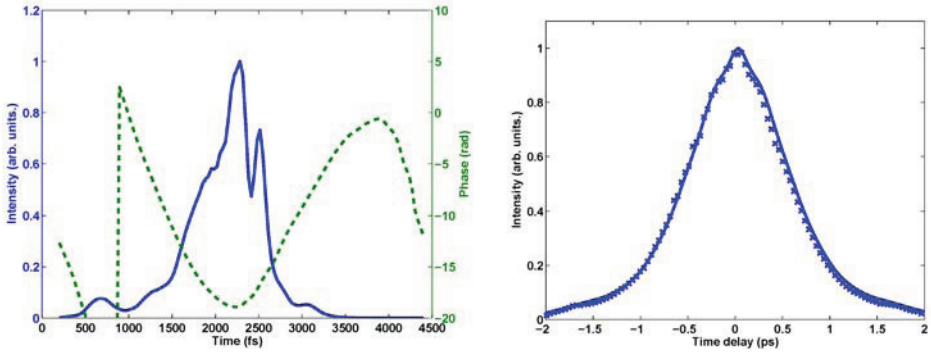


Figure 5.8: (left) The retrieved pulse intensity (blue line) and phase (green dotted line). (right) Comparison of the measured autocorrelation (blue stars) and the autocorrelation of the retrieved pulse (blue line).

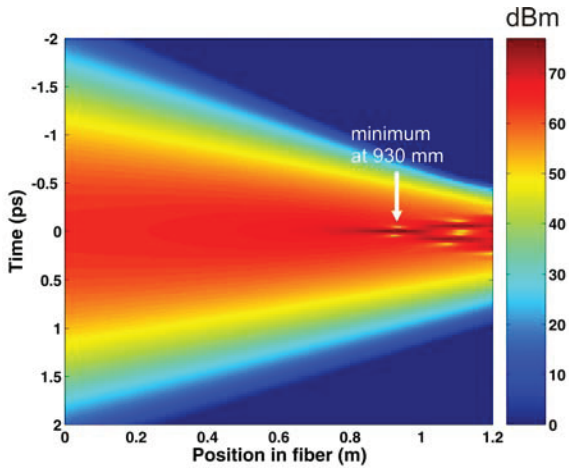


Figure 5.9: Pulse compression of a gaussian input pulse in 1.2 m SMF. The input pulse length is 1 ps, C=-10 and the pulse energy is 2.8 nJ. The minimum pulse intensity with a FWHM of 29 fs is reached after 930 mm of single-mode fiber.

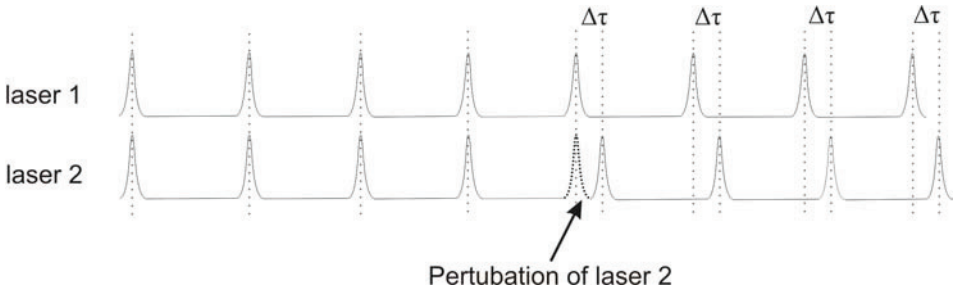


Figure 5.10: Electronically Controlled Optical Sampling (ECOPS) principle - the two lasers are locked to the same repetition rate. A short-term perturbation of one of the laser cavity lengths shifts the relative timing between the two pulse trains by an amount $\Delta\tau$.

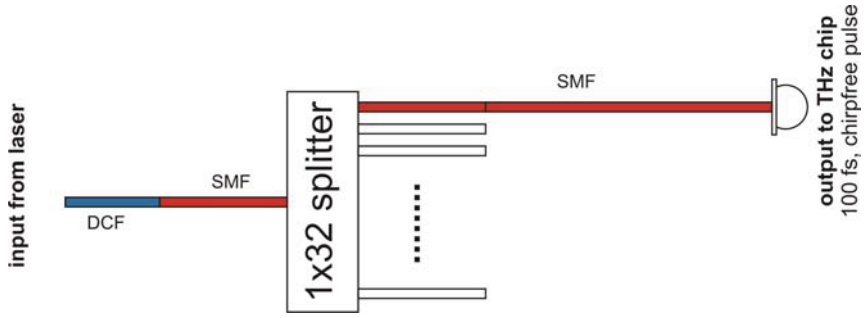


Figure 5.11: Schematic of the fiber link. The input laser pulse is stretched in a dispersion compensating fiber (DCF) module with single mode fiber (SMF) pigtails. The DCF module is spliced onto a 1 × 32 splitter and each of these channels is spliced onto a piece of single mode fiber for pulse compression.

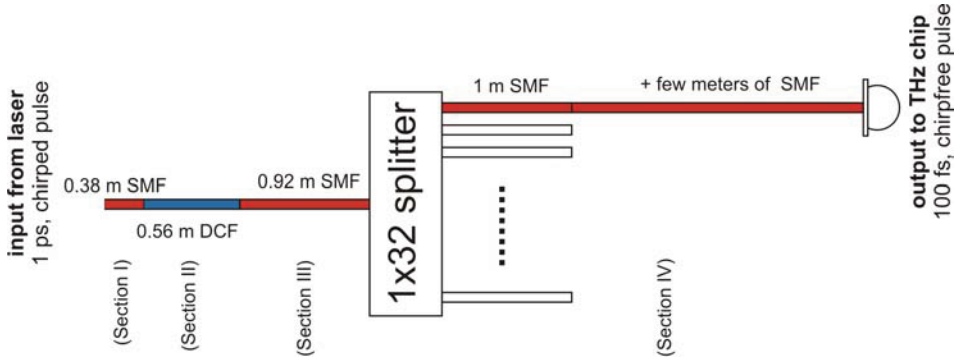


Figure 5.12: Design approach of the fiber link between the femtosecond laser and the THz antennas.

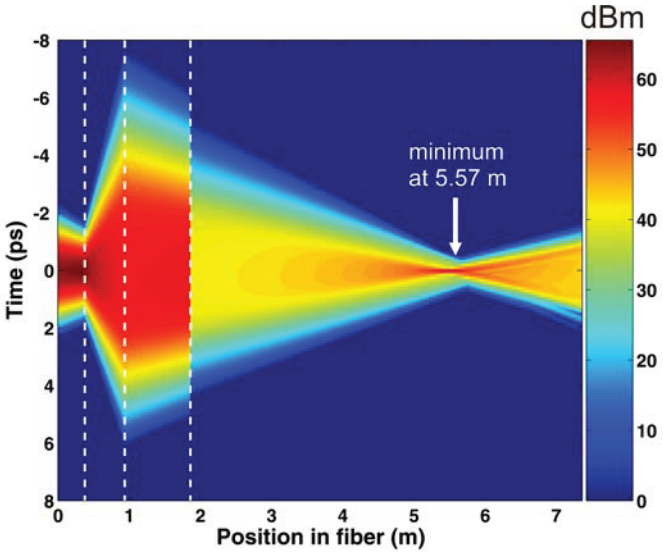


Figure 5.13: 2D plot on a logarithmic scale (dBm) of the pulse intensity during propagation through the fiber link. The input pulse is a Gaussian pulse with $\tau_{FWHM} = 1$ ps, $C = -10$, $E_{puls} = 2.8$ nJ. The abrupt change in intensity at $z = 1900$ mm propagation distance is due to the power splitter which reduces the power by 16.5 dB. The dashed lines indicate the boarders between the different fiber link sections.

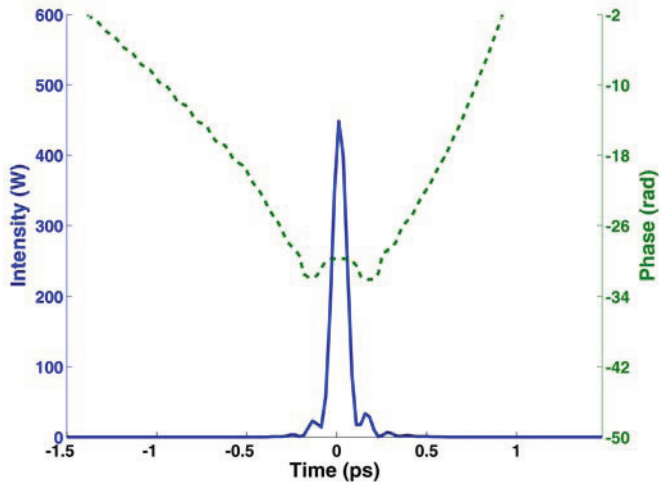


Figure 5.14: Plot of the intensity and the phase of the compressed Gaussian pulse at $z = 5570$ mm. The pulse exhibits a linear phase across the center peak showing a compressed pulse which is close to chirp-free. The FWHM pulse width is 94 fs.

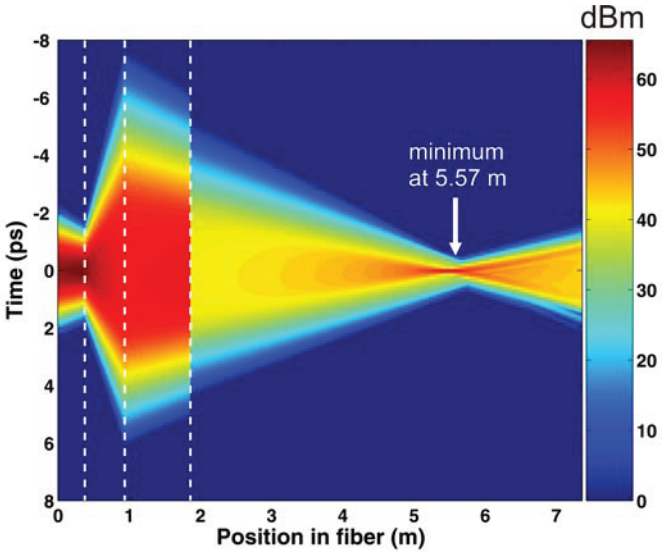


Figure 5.15: 2D plot on a logarithmic scale (dBm) of the development of the pulse shape of an Gaussian pulse ($\tau_{FWHM} = 1$ ps, $C = -10$, $E_{puls} = 4.7$ nJ) and intensity during propagation through the 425-mW fiber link.

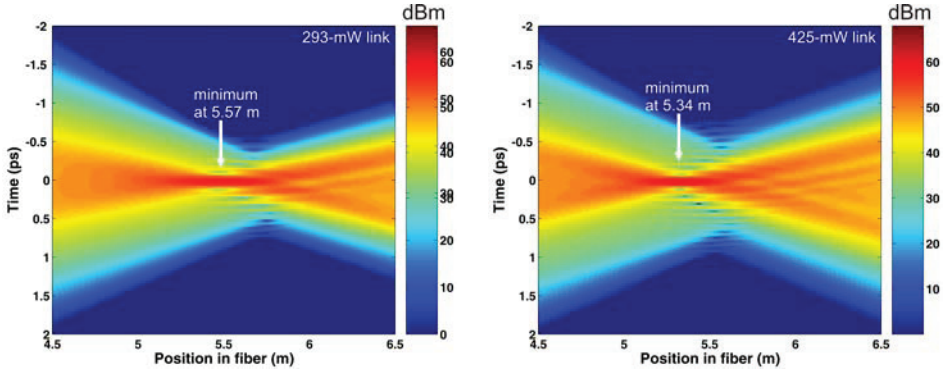


293-mW 425-mW

Figure 5.16: Zoom on the region of the fiber link where the pulse gets recompressed to its shortest pulse length.

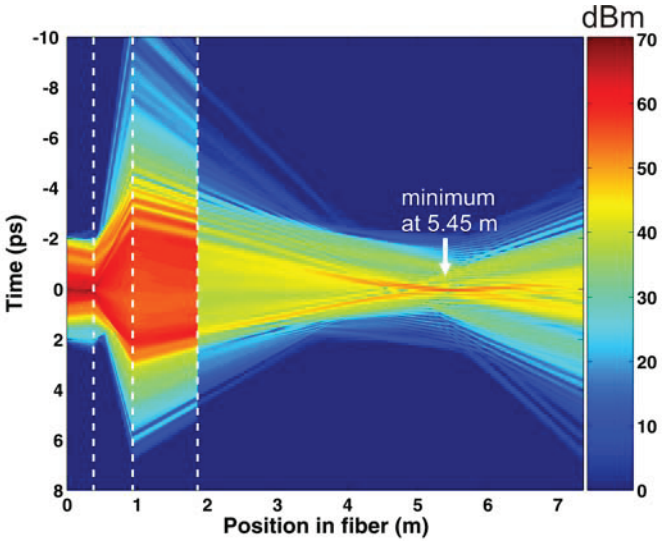


Figure 5.17: 2D plot on a logarithmic scale (dBm) of the pulse intensity as a function of fiber length using the measured output pulse from the FFS.SYS(laser 1) as input pulse.

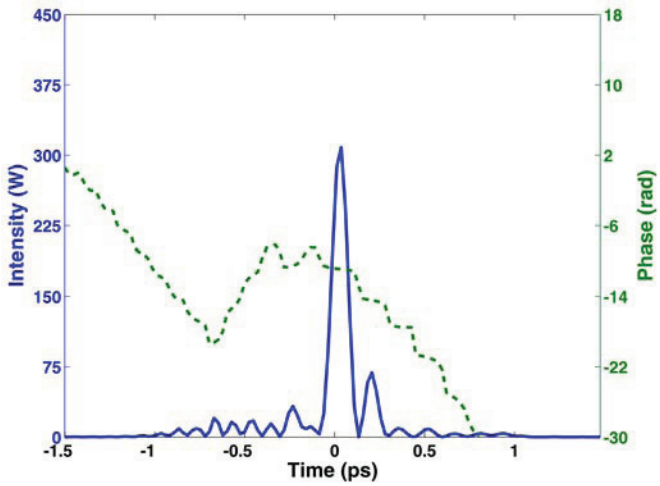


Figure 5.18: Plot of the intensity and the phase of the compressed pulse at $z = 5450$ mm. The optimum fiber link length has changed by 120 mm compared to the Gaussian input pulse simulation. The FWHM pulse lengths is 101 fs.

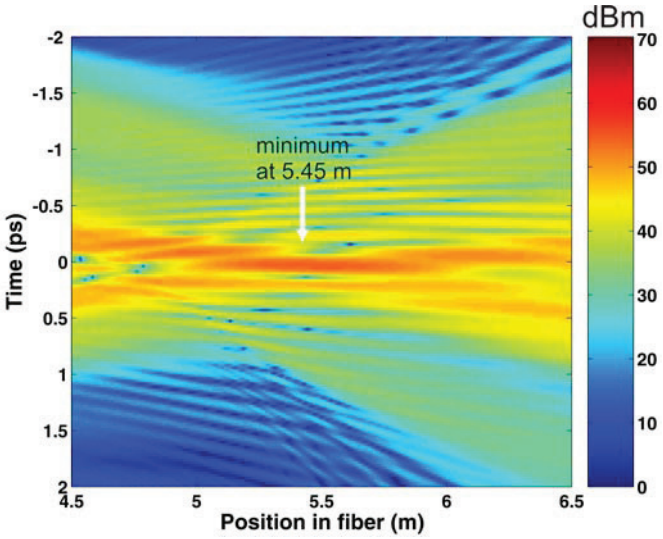


Figure 5.19: Zoom on the region of the fiber link where the pulse gets recompressed to its shortest pulse length.

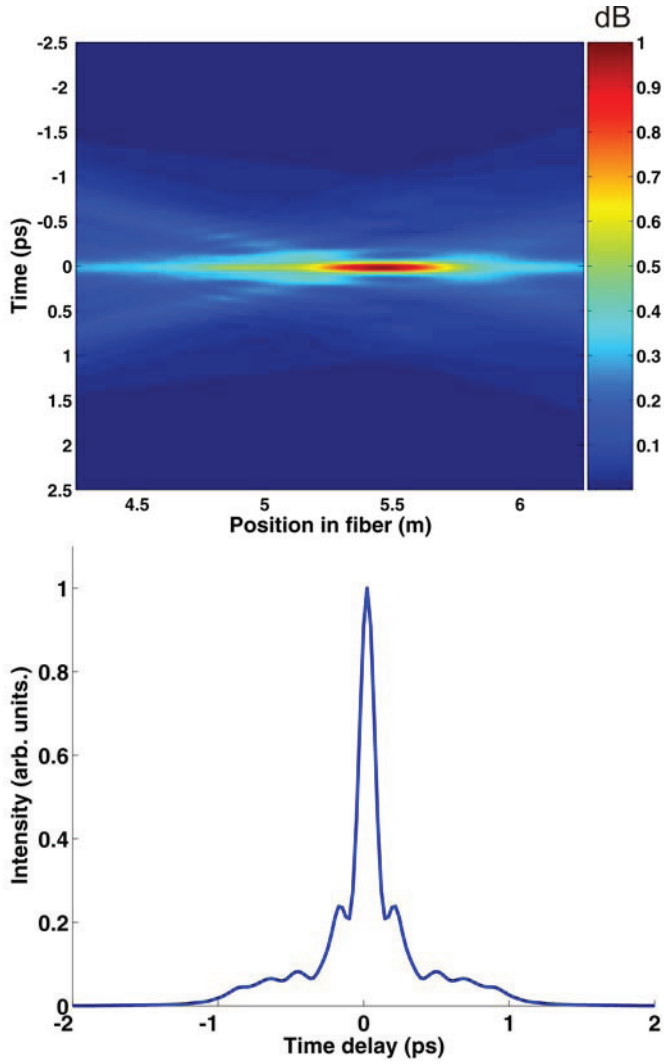


Figure 5.20: (top) 2D plot of the intensity autocorrelations of the pulses propagating along the fiber link. The intensity is normalized to unity. (bottom) Autocorrelation of the shortest pulse length at $z = 5450$ mm where the autocorrelation has a FWHM of 135 fs.

### Measurement results of fiber cutback experiments

The simulation results are validated in a fiber cutback experiment. We have recorded FROG traces for various fiber lengths, scanning across the area where the numerical simulations predicted a minimum pulse length. Figure 5.23 depicts a FROG trace of the position of the minimum measured pulse width at $z = 5100$ mm and the respective retrieved FROG trace. The retrieved FROG trace is in good agreement with the measured trace and exhibits a FROG-error of 1.5 %.

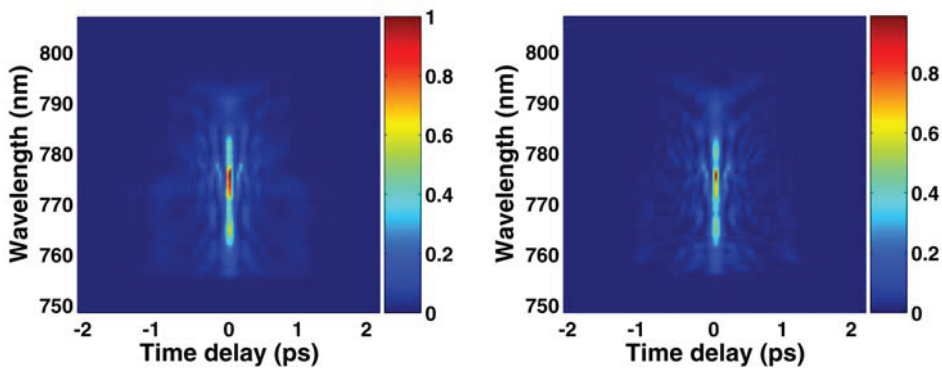


Figure 5.21: Measured and retrieved FROG trace of the minimum pulse duration at $z = 5100$ mm. The FROG-error of the retrieved pulse is 1.5 %.

The by the FROG algorithm retrieved pulse intensity and phase are shown in Fig. 5.22. The extracted pulse intensity exhibit ripples in the trailing edge indicating a complex pulse structure which is expected due to actual input pulse shape (cf. Fig. 5.8).

Fig. 5.23 shows a series of measured FROG traces at 4 different fiber cutback lengths obtained by following the pulse along the fiber towards the optimal pulse lengths minimum. The FROG traces exhibits how the pulse intensity both in frequency and in time-domain is assembled to one short

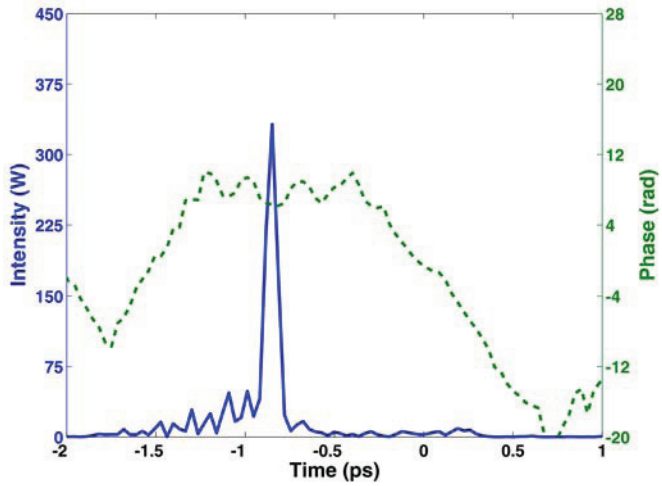


Figure 5.22: Plot of the intensity and the phase of the retrieved pulse at $z = 5100$ mm.

pulse. The energy in the pronounced side pulse in the FROG spectrogram, which in the autocorrelation appears as two pulses, is assembled in the center of the FROG trace when the optimum compressed pulse width is reached. This behavior is also seen in the numerical simulations. Notice that an simulations with an Gaussian input pulse not would be able to explain these spectrograms or equivalently explain the autocorrelations which show side pulses.

Fig. 5.24(top) shows a zoomed view of the measured autocorrelation functions as function of fiber link length. A minimum is seen at about 5.1 m of total fiber link length. At this point the pulse is shortest and the fiber should be terminated to the THz antennas. The development of the autocorrelations along the minimum pulse length show by comparing the two plots in Fig. 5.24 for measured and numerical data, respectively, very similar features before and after the full compression point. These feature are present despite the deviation in the fiber link lengths. The minimum measured autocorrelation FWHM is determent to 99.2 fs ($\sim$ 70 fs pulse

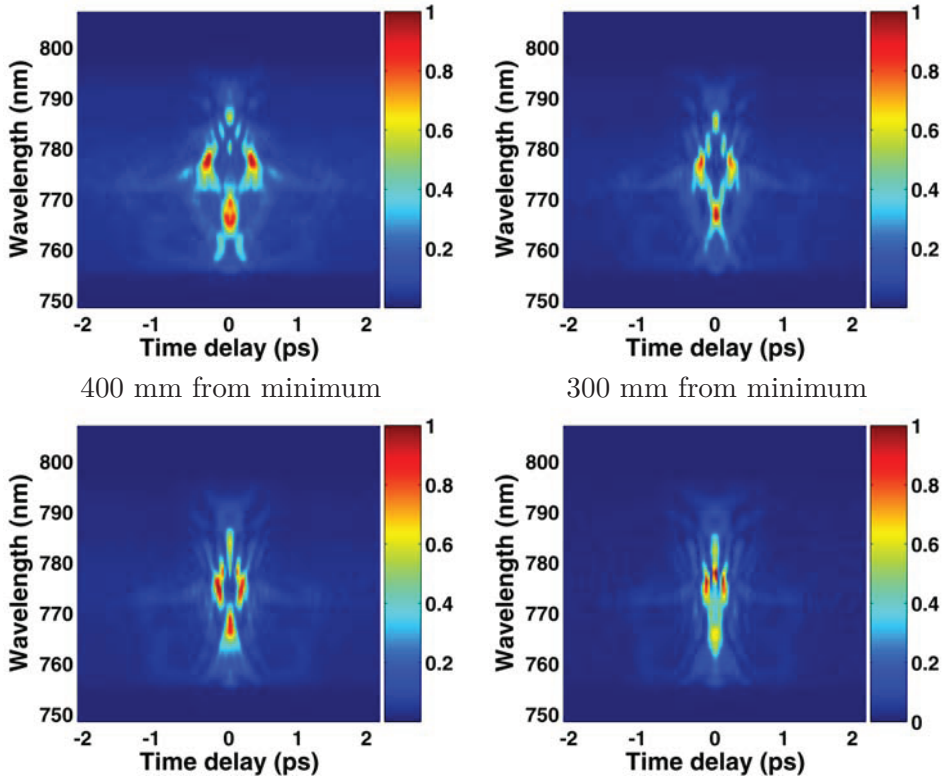


400 mm from minimum

300 mm from minimum

200 mm from minimum

100 mm from minimum

Figure 5.23: 4 FROG traces along the fiber following the pulse on the way to its minimum pulse width.

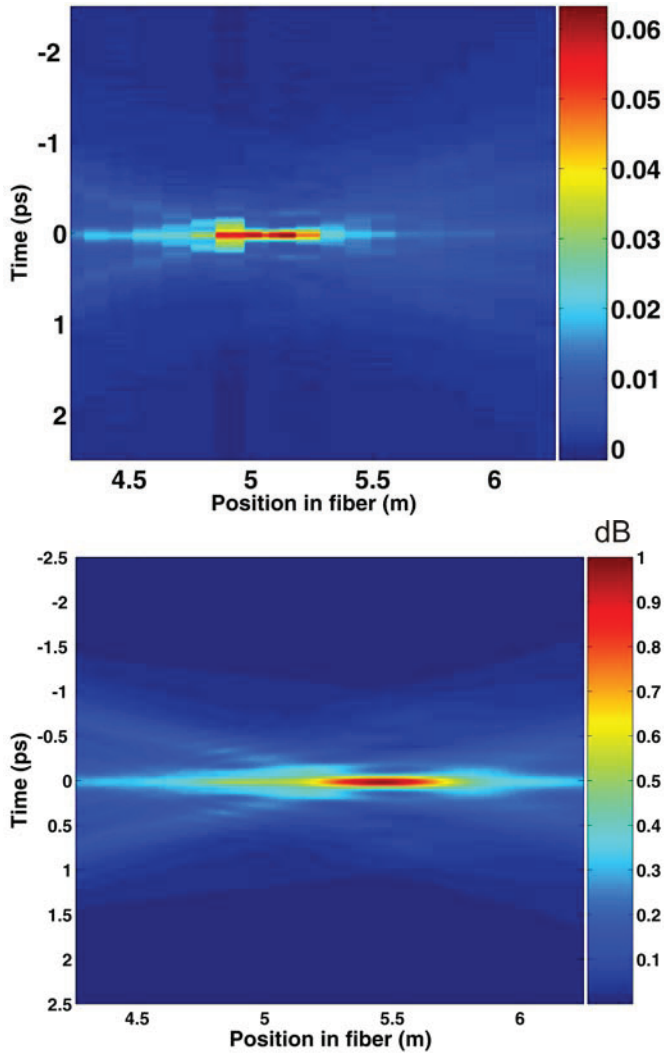


Figure 5.24: (top) The measured autocorrelation functions of the fiber link where the pulse gets re-compressed to a sub-100 fs pulse length. The data is obtained in a cutback experiment. The minimum pulse lengths is at $z = 5100$ m and has a autocorrelation FWHM of 99 fs (bottom) Simulated autocorrelations of the real input pulse from the FFS.SYS(laser 1). The autocorrelation FWHM is 135 fs at a minimum of $z = 5450$ m.

length) at 5.1 m link length (Fig. 5.25). Fig. 5.25 compares also the numerical autocorrelation at $z = 5450$ mm and the measured autocorrelation at $z = 5100$ mm. Also the two minimum pulse lengths autocorrelations are very similar and within the uncertainties of the experimental results acceptable.

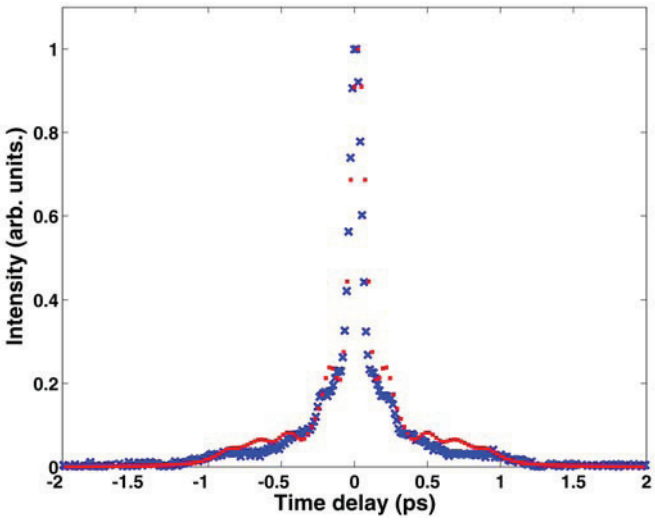


Figure 5.25: Plot of the measured (crosses) and the numerically simulated (squares) autocorrelations. The measures autocorrelation at a fiber link length of 5.1 m. The FWHM of the autocorrelation is 99.2 fs $\sim$ 70 fs pulse length.

Deviations to the numerical simulations regarding the optimal fiber link length can both be explained by the uncertainties of the fiber dispersion of the used Corning SMF-28 fiber, which is accurate within 5 % and variations in the active area of the fiber, which just is known within 10 % accuracy. These uncertainties of vital fiber parameters determining the dispersion and the nonlinearity are seen to be the major limiting factors for a more precise modeling of the fiber link. An exact determination of these fiber parameters for the fiber used could improve the quality of the numerical simulations.

The exact fiber parameters for the DCF fiber module were available for the numerical simulations. Since the minimum pulse width is at shorter fiber link lengths than predicted by the simulations does the fiber link exhibit more dispersion than expected. In the simulations presented has the fiber splitter been treated as a simple extension of the SMF. This might not be a valid approximation and lead to additional dispersion introduced by the planar waveguide structure inside the splitter. This could also give rise to faster compression in the fiber link.

## 5.6 Fiber splitters

The 32 THz transmitters will be connected to one of the lasers (FFS.SYS.HP) and the 32 THz receivers will be connected to the other laser (FFS.SYS). The femtosecond pulse train from each laser is coupled into a single-mode fiber, and split into 32 equal portions in a $1 \times 32$ power splitter from the Danish company Ignis Photonyx. These power splitters are based on planar waveguide technology developed at the Technical University of Denmark. The power splitters from Ignis Photonyx are capable of handling the required optical power (up to 440 mW). The technical specifications of the power splitters are summarized in Table 5.6. The loss is specified as max. 16.5 dB, with a uniformity better than 1.4 dB. The 1/32 splitting corresponds to a loss of 15.05 dB [10log(32)], and the remaining 1.5 dB is the insertion loss. The uniformity is a very conservative specification. The actual uniformity in the units that we have purchased displays a measured uniformity of approx. 0.2 dB, with an average loss of 16.3 dB.

| | |
|---|---|
| Operation wavelength | 1310 &1550 |
| Insertion loss [dB] | 16.5 |
| Uniformity [dB] | 1.5 |
| Return loss [dB] | >55 |
| Directivity [dB] | >55 |
| Operating Temp. | -40 to +85 |
| Dimensions | $100 \times 80 \times 10$ |

Table 5.6: Fiber splitter specifications.

Fig. 5.26 shows the appearance of one of the splitters. From the factory the inputs and all outputs are equipped with standard FC connectors, facilitating the construction of the fiber link. However, in order to reduce losses due to the connectors we will splice the power splitter directly to the input fiber from the laser system. The output fibers of the splitter can due to the reduced power level after the splitter be connected with the standard FC/PC connectors mounted by the vendor. This will keep the flexibility

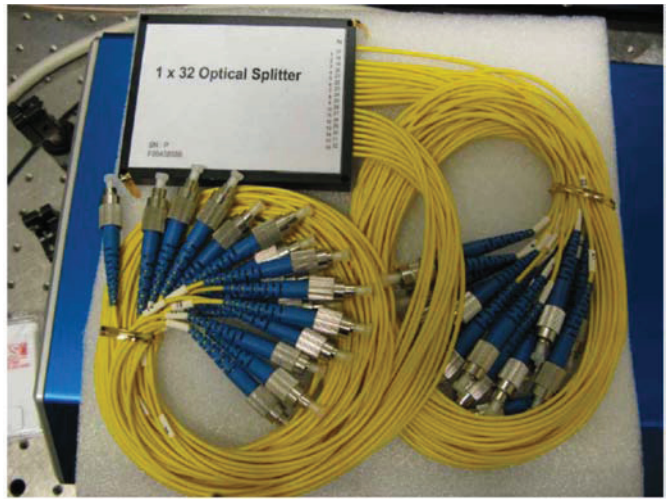


Figure 5.26: $1 \times 32$ power splitter from Ignis Photonyx. The power uniformity between the individual output channels is measured to be better than 0.2 dB.

to change the last part of the link which is directly connected to with the THz antennas.

## 5.7 Sensor head design

The optical fibers from the fiber link will be connected to the THz antennas inside a small unit that we will call the THz head in the following. The THz head will host the following components:

- THz antenna chip
- THz collimating optics
- Coupling between optical fiber and THz antenna
- Current-sensitive preamplifier (only THz detector head)

- Electrical connectors

The sensor head is designed on background of the electromagnetic simulations conducted by DTU Space and SynView. The simulations were showing the optimum placement and total number of emitters and detectors fulfilling the requirements for the whole system. Simulations showed that the optimum placement for the illumination of a $10 \times 10$ cm scene is to place both 32 emitters and 32 detectors in a square with missing corners (see Fig. 5.1). The optimum emitter spaced was showed to be 80 mm. The detectors are then placed in the center of the planar emitter array but only spaced by 13.3 mm. The detector placement put a very stringent design limitation on the layout of the sensor heads due to the extremely limited space available for the THz emitter and detector unit. A major effort has been to design units small enough to fit into available space. The detection unit incorporates a low noise trans-impedance amplifier to boost the photocurrent detected in the photoconductive chip to ensure sufficient signal-to-noise ratio before going onto a several meters long coaxial cable.

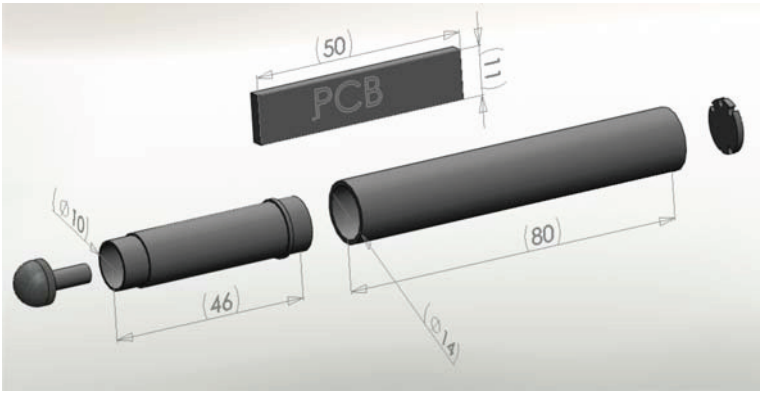


Figure 5.27: Rendering of the sensor head assembly. Shows the lens-chip-ferrule mount, the dimensions of the transinpedance amplifier and the mounts holding these parts together.

## Chip

Both THz emitters and receivers used are photoconductive switches (see chapter 3) to respectively generate and receive THz radiation. The THz antennas consists of a short dipole antenna metalized onto a photoconductive material. The photoconductive material used for the THz antennas should have a strong response at the wavelength of the laser system, 1.55 $\mu$m. Indium-gallium-arsenide (InGaAs) is the standard choice for this wavelength region due to the reduction of the band gap with increasing indium content. A short lifetime can be achieved by growing the material at a low temperature. However, this method often leads to unreasonably high dark currents. A high dark current is problematic for both THz emitters and THz detectors. In the emitter the dark current results in additional heating due to a background current that constantly flows when a bias voltage is applied to the antenna. In the THz detector the dark current results in additional noise. In order to circumvent these problems we have chosen a design known from the literature [24] where active regions of lowtemperature- grown InGaAs layers are isolated from each other by AlInAs barrier layers. The structure is illustrated in Fig. 5.28.

The active part of the structure consists of 100 repeat units of 12 nm beryllium-doped InGaAs and 8 nm of beryllium-doped InAlAs. The active region hence contains 1.2 $\mu$m of photoconductive material, comparable to the penetration depth of 1.55-$\mu$m photons. The active region is grown at low temperature (130°C) to ensure ultrashort carrier lifetime. The sheet resistance of this material has been reported to be in excess of 1M$\Omega/\square$, in contrast to bulk Be-doped low-temperature-grown InGaAs materials that exhibit sheet resistances below 50.000 $\Omega/\square$. The material is commercially available from Menlo Systems GmbH (Munich, Germany). This company delivers complete antennas (H-structure dipole stripline electrodes), and we have purchased a large batch (75 chips) for the project. THz pulses obtained from the antennas are illustrated in Fig. 5.29.

The chip specifications are depicted in Table 5.7. The THz radiation is collimated out of the photoconductor using hyper-hemispherical high-resistivity silicon lenses.

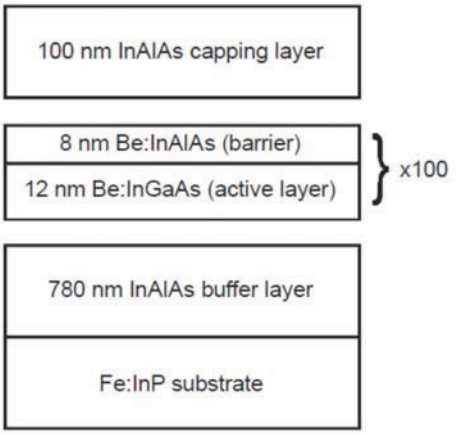


Figure 5.28: Schematic of the photoconductive material that will be used for the THz antennas. The active InGaAs regions are separated by barrier regions that contain the photogenerated charge carriers to the respective active layers. Hence the dark current is suppressed significantly.

Fig. 5.29 shows a THz pulse generated and detected making use of the photoconductive antennas described above, an all-fiber optic dispersion compensation scheme and a glued photoconductive antenna to silicon lens. The FWHM of the optical pulses is sub-100 fs and the optical power incident the emitter and detector is 10 mW, respectively. The applied bias voltage is modulated with 1 kHz for lock-in detection and the applied bias voltage of is ± 3 V. Fig. 5.29 shows the THz pulse and the Fourier-transform of the pulse, depicting a bandwidth up to 2 THz and a SNR of approximately 1:250.

### Lens

The THz radiation generated in the small spot at the output of the fiber will be collimated using hyper-hemispherical silicon lenses. These lenses are de-

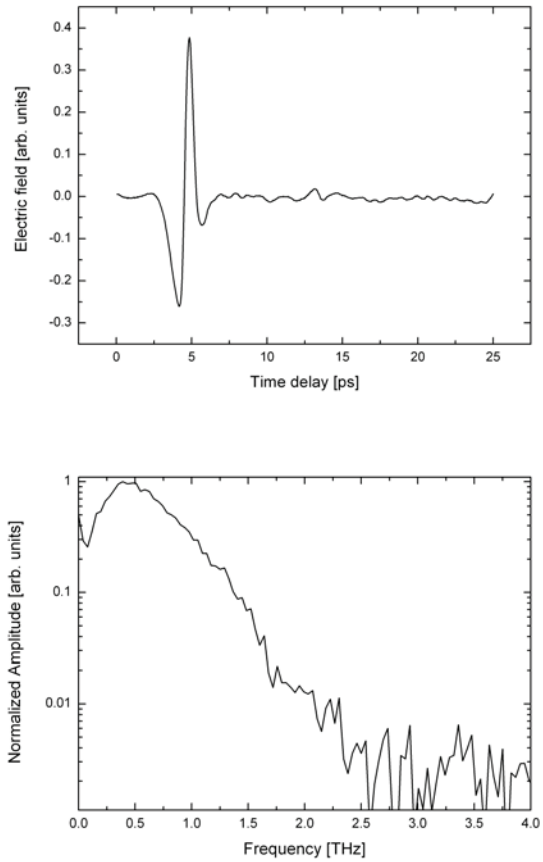


Figure 5.29: (top) THz pulse generated and received with photoconductive antennas from Menlo fed by femtosecond laser pulses from the fiberlink. 10 mW input power on both emitter and receiver and ± 3 V bias modulation with 1 kHz on the emitter. (bottom) Fourier-transform of the THz pulse.

| | |
|---|---|
| **Dipole length** | 25 $\mu$m |
| **Photoconductive gap** | 10 $\mu$m (matched to SMF-28 MFD) |
| **Photosensitivity** | $< 1.57$ $\mu$m |
| **Electrical bias voltage** | 3 V |
| **Laser power** | $5 - 30$ mW |
| **Laser pulse length** | $100 - 200$ fs |
| **Dark current** | 350 $\mu$A |
| **Increase of current at correct alignment** | $12 - 40$ $\mu$A |
| **Substrate thickness** | 350 $\mu$m |
| **Antenna chip dimensions** | $4 \times 4$ mm$^2$ |

Table 5.7: Antenna chip specifications

| | |
|---|---|
| **Lens type** | Hyper-hemispherical lens |
| **Material** | High-resistivity float-zone (HRFZ) silicon |
| **Surface quality** | 80/50 scratch/dig |
| **Surface accuracy** | 0.01 mm deviation from ideal sphere and plane |
| **Diameter** | $10.00 \pm 0.03$ mm [radius $5.00 \pm 0.015$ mm] |
| **Height** | $6.71 \pm 0.03$ mm |
| **THz chip substrate thickness** | Prepared for 350 $\mu$m substrate |

Table 5.8: Specifications of THz substrate lenses for the antennas

livered from the Russian supplier Tydex Inc. which has a long track record in delivery of silicon THz optics to companies and research laboratories. The specifications of the THz lenses are shown in Table 5.8.

Design consideration on the lens are the alignment precision between the focal point of the lens and the center of the photoconductive gap on the THz chip. In this compact THz sensor head design the lens is glued directly together with the chip. After an investigation of the correct viscosity of the UV-curing glue used the lens could be positioned with a precision of 8 $\mu$m into the gap of the THz chip. This precision is judged to be sufficient with background in [121].

### LNA amplifier design

The special designed low-noise amplifier (LNA) has a trans-impedance gain of $10^9$ V/A, hence generating a voltage of 1 V for a THz signal strength of 1 nA which is typically seen in a THz-TDS system. The PCB of the current pre-amp has dimensions $1.1 \times 5.0$ cm$^2$, and is mounted inside the cylindrical THz head housing. THz pulses detected with the current preamplifier, using a conventional THz-TDS system, are shown in Fig. 5.30. The THz pulse was monitored on a digitizing oscilloscope at a scan rate of 8 Hz, limited by the mechanical motion employed in that experiment. The noise on the baseline of the THz trace recorded by the newly developed current LNA preamplifier is significantly lower than the noise seen on the trace recorded using a commercial current preamplifier. The power supply voltage was set to $+/-5$ V.

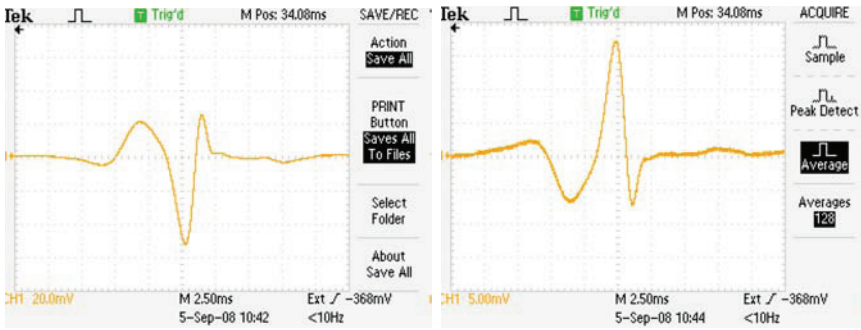


Figure 5.30: THz traces recorded at a scan rate of 8 Hz, using the newly developed current preamplifier (left) and a commercially available preamplifier(right). Our design shows a lower baseline noise and higher bandwidth than the commercial product.

### Sensor head assembly

The sensor head will be assembled in the housing depicted in Fig. 5.31. The housing is designed with respect to facilitate a receiver spacing of

13.3 mm and a low-cost workshop manufacturing. Only the receiver will incorporate the LNA, while the emitter is connected to a bias supply. The lens-chip-fiber assembly shown in the inset of Fig. 5.31 will be slided in one of the cylindrical aluminum parts. The LNA will in the receivers be slided into the remaining cylindrical tube. An electrical ground connection will be established by a connection of the outer ground border of the custom designed LNA print board to the housing, which will assure good noise shielding. The fiber and the electrical wiring will be routed from the end facet of the sensor head to the PCB and LNA board, respectively.

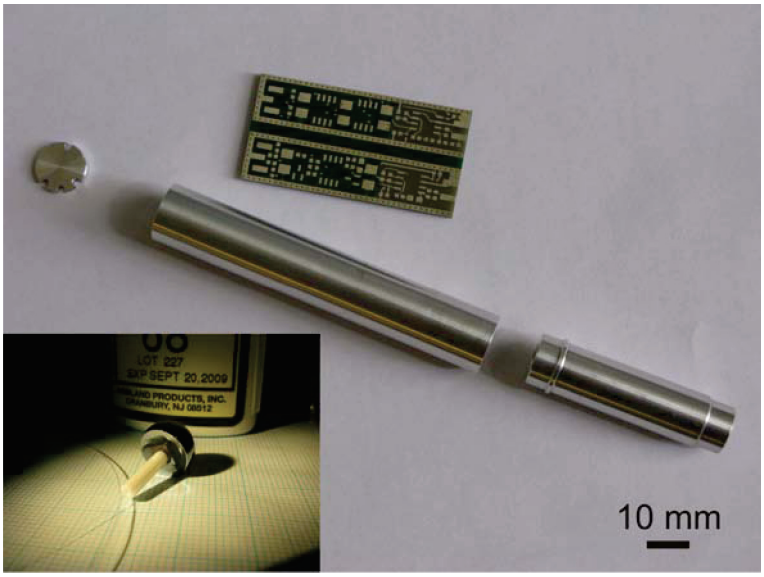


Figure 5.31: Photograph of the parts of the THz sensor head. The diameter of the heads is 12 mm, and the total length is 130 mm. The silicon lenses have a diameter of 10 mm and will be mounted into the rightmost part. The PCB shows the unpopulated current amplifier and fits into the tube shown in the center of the picture. The inset Photoconductive antenna chip glued directly onto the silicon lens. The fiber link is butt-coupled into the photoconducting gap.

The connection between the lens, the chip and the fiber will be established as sketched in Fig. 5.32.

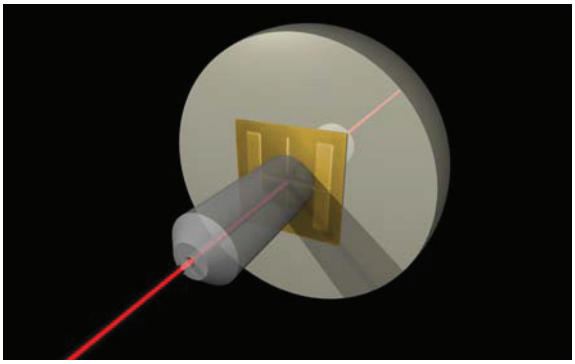

Figure 5.32: Sketch of the lens, THz chip and butt-coupled fiber assembly.

The lenses will be aligned with respect to the THz antenna using a custom-made alignment tool, as indicated in Fig. 5.33, which holds the silicon lens with a vacuum while the chip is aligned on the lens backplane with respect to the lens center under a microscope, using four needles attached to x-y translation stages. Once aligned with respect to the center, the chip is pressed to the lens back plane by a fifth needle, and low-viscosity glue is applied in a small droplet at the edge of the chip. After drying the chip is securely mounted to the lens backplane, and aligned to as good as precision as the specification of the lens diameter allows. The optical fiber will be attached directly in contact with the THz antennas. We prefer this solution instead of initial designs where a free-space unit conjugate optic (UTC) was suggested to couple light from the fiber to the THz antenna. This modification is due to:

- Higher stability of the glued solution,
- More compact construction, allowing smaller THz head.

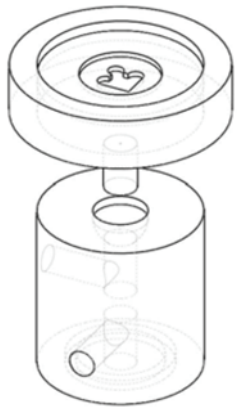

Figure 5.33: Tool for alignment of the hyperhemispherial silicon lens precisely with respect to the photoconductive gap on the THz antenna.

The fiber will be placed inside a ceramic ferrule, attached with glue (Northland Optical Adhesive, NOA63), and polished to optical quality. Custom-made ceramic ferrules with plane end facets (normally the ends are rounded on ferrules) are supplied by the company Adamant Kogyo co., Japan. The ferrule with fiber is then attached to the photoconductive area of the THz antenna while monitoring the photocurrent in the antenna. After optimizing the photocurrent according to the specifications supplied by Menlo Systems for each chip by lateral motion of the ferrule, low-viscosity glue will be applied and allowed to dry. During the curing process the photocurrent will be continuously monitored, and small possible drifts of the alignment can hence be monitored and corrected. The THz antenna is then a single unit with fiber and silicon lens glued on each side of the THz chip. This solution results in a construction with no parts that can be moved with respect to each other, and hence the construction will be very stable.

| | |
|---|---|
| Number of transmitters, Tx | 32 |
| Number of receivers, Rx | 32 |
| Distance from array center to scene center | 300 mm |
| Tx array | $6 \times 6$ square, 4 corner elements missing |
| Tx element spacing | 80 mm |
| Rx array | $6 \times 6$ square, 4 corner elements missing |
| Rx element spacing | 13.3 mm |
| Construction material | Aluminium |
| Fabrication tolerance | $\pm$ 0.01 mm on all important dimensions |

Table 5.9: Specification of the geometrical arrangement of the photonic imaging array.

## 5.8 Design of the 2D synthetic aperture array

The individual THz antennas will be mounted in an array as determined by the detailed numerical simulation of the best possible arrangement performed by SynView GmbH and DTU Space. The array will be set up with all emitters and detectors located in the same plane with the geometrical and material specifications shown in Table 5.9. The 32 receivers are stacked in a 6 mm $\times$ 6 mm square in the inner part of the array and spaced by 13 mm. The transmitter units are placed in the outer part and spaced by 80 mm. All units are fitted into a $20 \times 500 \times 500$ mm aluminum mounting structure and pointing towards a center of scene at 300 mm from the structure. Each Tx/Rx element is directed towards the scene center, and each Tx element is illuminating the full scene. This feature made the manufacturing process of the aluminum mounting structure highly non-trivial. Since the mounting hole for every single units needs to be tilted by 2 angles relative to the plane of the plate, being able to point towards the center of the scene, this required skills from a highly specialized machine shop. The 2D array was finally produced at the Risø DTU mechanical workshop on a computer controlled CNC 5-axis milling machine.

Fig. 5.34 shows the 3D rendering of at fully populated imaging array and Fig. 5.35. Manufacturing

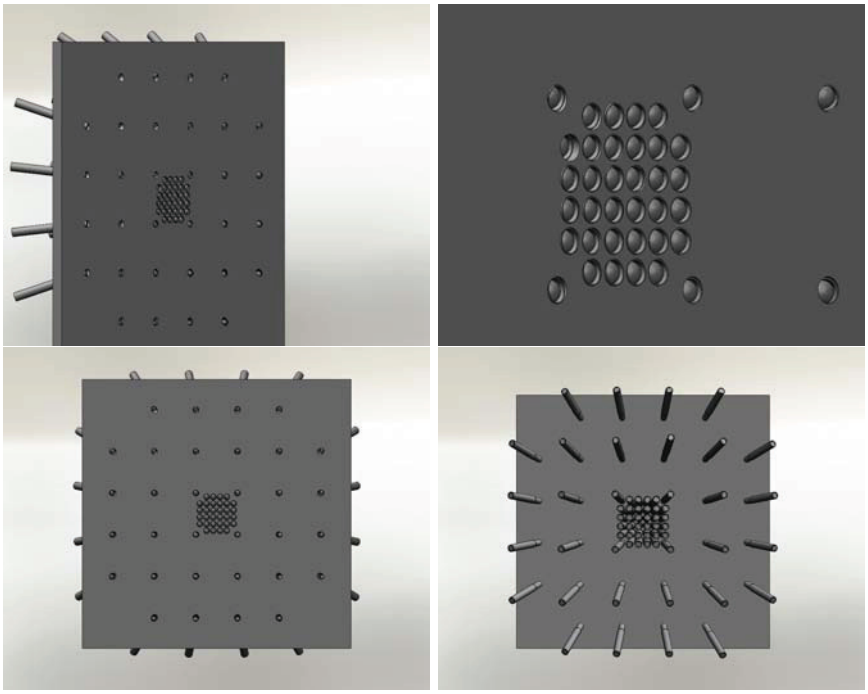

Figure 5.34: 3D CAD rendering of the 2D synthetic aperture array including 32 emitter and 32 detector heads.

## 5.9 Data aquisition

The data acquisition concept was designed in collaboration with DTU Elektro and is not realized yet. The data acquisition board for the photonic imaging system is illustrated schematically in Fig. 5.36. The basic concept of the data acquisition is to establish a lock-in detection scheme for every single emitter/receiver channel. Every single emitter is bias-modulated with its own carrier frequency controlled by a 32 channel DAC card. The data from the individual receiver channels is detected by an 32 channel ADC card and in the following stage demodulated in the data processing

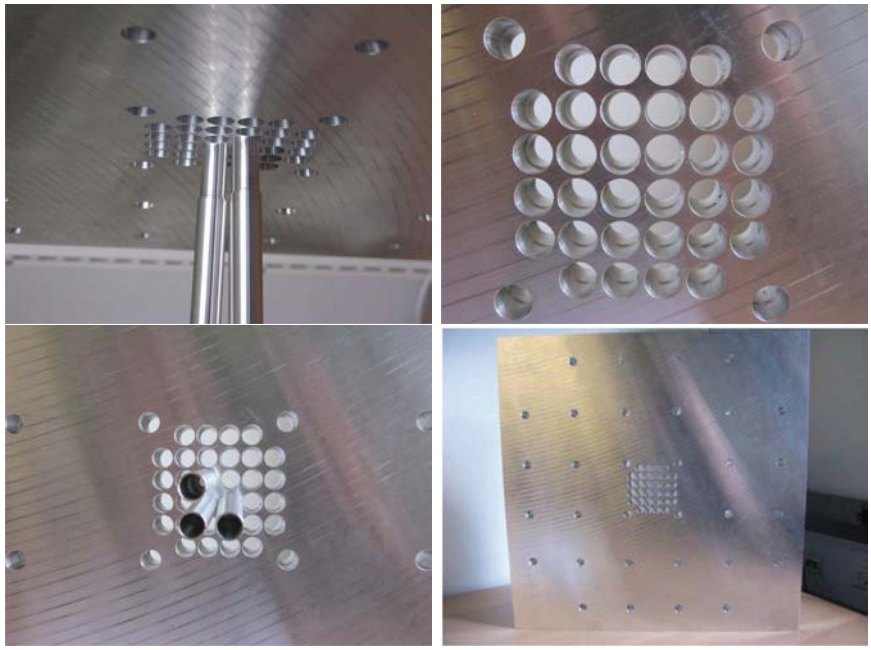

Figure 5.35: Photographs of the 2D synthetic aperture array including 32 emitter and 32 detector heads.

software. The preprocessing software is preparing the acquired data for the imaging algorithm, that is reconstructing the 3D image.

An ICS-610 32 channel ADC board and the ICS-625B 32 channel DAC board are the most likely candidates for the photonic imaging systems data acquisition unit, but the final decision is not made yet. The system is comprised of 32 channels each sampled with 64 kS/s. This leads to a IF modulation bandwidth of 32 kHz for the receiver channels. The data is received in slices of 1 ms and hence the number of samples is Np = 64 (samples / receiver) $\times$ 32 = 2048Samples.

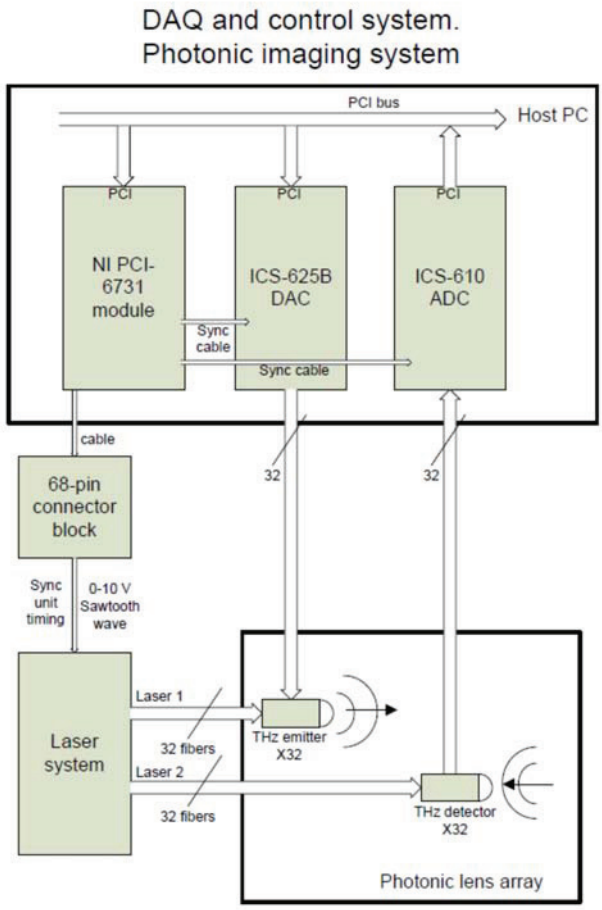


Figure 5.36: Photonic data acquisition system. The same National Instruments PCI board that is used in the electronic imaging system can be used here to trigger the DAC and ADC boards and control the laser synchronization unit.

## 5.10 Results from whole system

The result for the whole imaging system are not available at this point in time since the project is running until spring 2010. All the work from the project partners on the 'THz camera' project will be joined together during the winter 2009. The final results are expected to be published during 2010.

A major challenge for the next months is seen in the interplay between the data acquisition and the 32 receivers and 32 detectors. One of the novelties of this system is a complex emitter modulation scheme where all 32 emitters are emitting simultaneously at their individual modulation frequency. The demodulation of reflected signal is then obtained in form all 32 receivers. This well known principle from radiocommunication channels has until today not been shown for THz systems.

Another major challenge is besides the data acquisition the imaging algorithm, which is inverting the scattered back-reflections from the image plane and is processing in into a real time image. This is as well a well known principle for the radar community, but a completely new approach for THz systems.

## 5.11 Summary

This chapter has presented the work on the ESA THz camera project conducted as part of the thesis work. The work has concentrated on the scientific development and research towards the implementation of a novel synthetic aperture THz camera consisting of a 32 emitters and 32 detectors placed in 2D synthetic aperture array. Some highlighted features of the design are:

- Employment of a synchronized femtosecond fiber laser system with electronic delay control.
- Development of an all-fiber pulse compression scheme for the fiber link used for distribution of ultrashort laser pulses towards the emitter and detector array.

- Characterization of the ultrashort pulses with a custom-build FROG and the validation of the fiber link by numerical simulations.
- Design of ultra-compact sensor heads featuring the strict limitations on the physical layout of the THz emitters and detectors.

A full system implementation needs still to be shown in scope of the finalization of the ESA project.

# Chapter 6

# Conclusion & Outlook

## 6.1 Conclusion

This thesis presents different contributions towards the use of fiber based multi-element imaging systems and investigated especially how fiber technology could contribute to this. Modern fiber technology can improve the flexibility, the robustness and the cost of the classical THz systems both by the application of fiber optical sources and by the employment of optical fibers as distribution medium for optical pulses. The work presented in this thesis can be summarized with the following:

**Need for improved THz imaging systems** By reviewing the field of pulsed THz imaging systems in chapter 3 one can recognize the clear need for a robust, fast and easy-to-use multi-element THz imaging system. The fundamental concepts of a vast of imaging techniques have been proposed but mostly these employ very basic imaging techniques. Time-of-flight-measurements have until today been the most successful technique finding more and more application areas, also in industrial applications. The fundamental problem of the technique is still the image acquisition time which for most industrial applications is far too long. This problem has been addressed attention and various techniques have been proposed to speed up the imaging time.

There is though today still a profound need for a faster imaging speed at e.g. video rate.

**Optical source for CW THz systems** Chapter 2 presented results on a novel fiber laser system for CW THz generation. The laser system is tuneable over more than 1 THz, and the difference frequency has a linewidth of below 25 kHz. The system is fully scalable with respect to power and can be distributed along optical fibers to a multi-element array of THz emitters and detectors. The nonlinear effect from four-wave-mixing where suppressed 50 dB and no indications of SBS was observed. The source is ready to be employed in an THz photomixing setup by having the needed photoconductive material available now.

**THz-TDS measurements of Carbon nanotubes** Chapter 4 showed two experiments using a fiber coupled THz-TDS system. Especially the scattering experiments could barely not be conducted without a fiber based system due to the enormous amount of realignment needed when using classical free-space coupled THz emitter and detector units. The acquisition of angle resolved scattering data from various objects is a very good example where a simple, hassle-free fiber-coupled measurement instruments no longer are requiring the majority of attention. The application itself is getting into focus as a result of improved technology and operator usability. The scattering of pulsed THz waves from a carbon nanotube carpets showed a unexpected significance compared to bulk metal. The mechanism for the enhanced scattering is until today not fully understood. Experiments on CNT fibers with a THz-TDS system showed the ability to measure conductivity changes possibly connected to impurities and contamination in the nanotubes fibers. These measurements could be a valuable tools for understanding and monitoring the impurities in CNT fibers.

**ESA THz Camera** This chapter has presented the work on the ESA 'THz camera project' conducted as part of the thesis work. The work has concentrated on the scientific development and research to-

wards the implementation of a novel synthetic aperture THz camera consisting of a 32 emitters and 32 detectors placed in 2D synthetic aperture array. Some highlighted features of the design are:

- Employment of a synchronized femtosecond fiber laser system with electronic delay control.
- Development and implementation of an all-fiber pulse compression scheme for a fiber link used for distribution of sub-100 fs laser pulses towards an THz emitter and detector array.
- Characterization of the ultrashort pulses with a custom-build FROG and the validation of the fiber link by numerical simulations.
- Design of ultra-compact sensor heads featuring the strict limitations on the physical layout of the THz emitters and detectors.

A full system implementation needs still to be shown in scope of the finalization of the ESA project.

## 6.2 Outlook

This thesis presents various active THz imaging techniques, concept and application areas that can be considered as state-of-the-art. The promising full implementation of the THz Camera described in chapter 5 is from our point of view a very exciting contribution towards new advanced imaging concepts and we are looking very much forward to see the performance in the near future.

Despite the vast of application areas where THz imaging is considered as highly useful, is the big breakthrough still awaited. The main reason for, that we have been talking about THz imaging for the last 10 years without major advances, can closely be related to issues in getting the technology out of the laboratories. One big problem has been addressed with the advent of the fiber-laser and the today commercially available fiber-coupled sensor heads. Another problem that needs attention is the

imaging speed, which due to the low output power of the THz emitters and the mechanical translationstages is fundamentally limited. Advanced imaging techniques as presented in this thesis will in the future show if a stable and fast imaging system can make a major breakthrough in the use of THz imaging in industrial applications. The industrial interest in non-destructive imaging techniques is enormous and many problems are looking for a new technological solution making e.g. quality control better, cheaper and faster. The potential is enormous. THz imaging might today be able to contribute in some areas, but the major issues have often been the price of a system and the imaging speed compared to other related technologies. This leaves THz technology as it is today almost exclusively to compete on the factor that the technology can do things better or do things not achievable with other well-established technologies. However, if a big application area can be identified were THz technology and THz imaging are solving major technological problems, the technology could get its big breakthrough. If a application igniting the market can not be found, will THz technologies very likely always be present in various specialized application areas, especially in the field of non-destructive testing, were the unique capabilities of terahertz technology can be extremely useful, but at a smaller market scale.

# Chapter 7

# Acknowledgements

I am highly indebted to many people who all contributed in a vast of different ways to this work and finally made *everything* possible. I will especially like to thank the following people:

- Professor **Peter Uhd Jepsen** the group leader of the Terahertz Technologies & Biophotonics Group at DTU Fotonik and one of the main supervisors of this work. When I started at the institute I was Peter's first ph.d. student in Denmark and during the last 3 years Peter has managed to build up a strong, diverse and inspiring research group. Despite the fast growth of the group, Peter always had an open door and made time for discussions and problem solving with his students. His tremendous knowledge on physics, THz technology and his lab experience in general saved us ph.d. students very frequently from wasting our time.
- **Jens Engholm Pedersen** for supervising this project and providing me with fiber laser from Koheras.
- My fellow ph.d. students **Uffe Møller** and **Rasmus K. Olsson** for many on and off-topic discussions and all the help and collaboration during the years. A special thanks to Rasmus for the big help with the FROG measurements.

- The Terahertz Technologies & Biophotonics Group at DTU and especially Master student Jonas Due Buron for the help on the new THz chips.
- DTU Fotonik's administration and the mechanical workshop at DTU Elektro.
- Project partners in the ESA project from **DTU Elektro**, **DTU Space** and **Synview GmbH**.
- The Technical University of Denmark, Photonics Academy Denmark, NKT Photonics and Danish Ministry of Science, Technology and Innovation for financing my ph.d. work.
- Special thanks goes to **Dr. Jason Deibel** who made my stay at Wright State University possible. I had a great and memorable time exploring the student life in the mid-West. I enjoyed the stay in Dr. Deibels group and wish him the very best for the future in building up a strong research group. I am further grateful to Dr. Deibel and WSU for financing my trip to the OTST 2009 in Santa Barbara to present the results on my carbon nanotube work I made during my stay at WSU.
- I would also like to acknowledge the people in the Terahertz and Ultrafast Photonics Research Group at Wright State University: **Zach Gault**, **Nick Schroeder**, **Lindsey Owens** and **Michael Moulton**. I enjoyed to be a part of your group.

Finally, I would like to thank my family and especially my girlfriend Mette for their unlimited support and patience throughout this stressful period.

# Bibliography


[1] G. P. Williams, "Filling the THz gap: high power sources and applications," *Reports on Progress in Physics*, vol. 69, no. 2, p. 301, 2006.

[2] M. Abo-Bakr, J. Feikes, K. Holldack, G. Wüstefeld, and H.-W. Hübers, "Steady-state far-infrared coherent synchrotron radiation detected at BESSY II," *Phys. Rev. Lett.*, vol. 88, p. 254801, Jun 2002.

[3] A. Bergner, U. Heugen, E. Bründermann, G. Schwaab, M. Havenith, D. R. Chamberlin, and E. E. Haller, "New p-Ge THz laser spectrometer for the study of solutions: THz absorption spectroscopy of water," *Review of Scientific Instruments*, vol. 76, no. 6, p. 063110, 2005.

[4] G. Ramian, "The new UCSB free-electron lasers," *Nuclear Instruments and Methods in Physics Research Section A: Accelerators, Spectrometers, Detectors and Associated Equipment*, vol. 318, no. 1-3, pp. 225 – 229, 1992.

[5] G. Kantorowicz and P. Palluel, *Infrared and Millimeter Waves*, vol. 1, ch. 4. Academic Press, 1979.

[6] N. Karpowicz, H. Zhong, C. Zhang, K.-I. Lin, J.-S. Hwang, J. Xu, and X.-C. Zhang, "Compact continuous-wave subterahertz system for inspection applications," *Applied Physics Letters*, vol. 86, no. 5, p. 054105, 2005.

[7] T. Fong and H. Kuno, "Millimeter-wave pulsed IMPATT sources," *Microwave Theory and Techniques,* IEEE *Transactions on*, vol. 27, pp. 492–499, May 1979.

[8] E. R. Brown, J. R. Söderström, C. D. Parker, L. J. Mahoney, K. M. Molvar, and T. C. McGill, "Oscillations up to 712 GHz in InAs/AlSb resonant-tunneling diodes," *Applied Physics Letters*, vol. 58, no. 20, pp. 2291–2293, 1991.

[9] E. Bründermann, H. P. Röser, A. V. Muravjov, S. G. Pavlov, and V. N. Shastin, "Mode fine structure of the p-Ge intervalenceband laser measured by heterodyne mixing spectroscopy with an optically pumped ring gas laser," *Infrared Physics and Technology*, vol. 36, no. 1, pp. 59 – 69, 1995. Proceedings of the Sixth International Conference on Infrared Physics.

[10] S. Barbieri, J. Alton, S. Dhillon, H. Beere, M. Evans, E. Linfield, A. Davies, D. Ritchie, R. Kohler, A. Tredicucci, and F. Beltram, "Continuous-wave operation of terahertz quantum-cascade lasers," *Quantum Electronics,* IEEE *Journal of*, vol. 39, pp. 586–591, Apr 2003.

[11] G. Scalari, C. Walther, M. Fischer, R. Terazzi, H. Beere, D. Ritchie, and J. Faist, "THz and sub-THz quantum cascade lasers," *Laser and Photonics Review*, vol. 3, no. 1-2, pp. 45–66, 2009.

[12] S. Cherednichenko, P. Khosropanah, E. Kollberg, M. Kroug, and H. Merkel, "Terahertz superconducting hot-electron bolometer mixers," *Physica C Superconductivity*, vol. 372, pp. 407–415, Aug. 2002.

[13] D. E. Prober, "Superconducting terahertz mixer using a transition-edge microbolometer," *Applied Physics Letters*, vol. 62, no. 17, pp. 2119–2121, 1993.

[14] B. Ferguson, S. Wang, D. Gray, D. Abbot, and X.-C. Zhang, "T-ray computed tomography," *Opt. Lett.*, vol. 27, no. 15, pp. 1312–1314, 2002.

[15] S. Wang and X.-C. Zhang, "Tomographic imaging with a terahertz binary lens," *Applied Physics Letters*, vol. 82, no. 12, pp. 1821–1823, 2003.

[16] J. Pearce, H. Choi, D. M. Mittleman, J. White, and D. Zimdars, "Terahertz wide aperture reflection tomography," *Opt. Lett.*, vol. 30, no. 13, pp. 1653–1655, 2005.

[17] K. McClatchey, M. T. Reiten, and R. A. Cheville, "Time resolved synthetic aperture terahertz impulse imaging," *Applied Physics Letters*, vol. 79, no. 27, pp. 4485–4487, 2001.

[18] J. O'Hara and D. Grischkowsky, "Quasi-optic synthetic phased-array terahertz imaging," *J. Opt. Soc. Am. B*, vol. 21, no. 6, pp. 1178–1191, 2004.

[19] A. Bandyopadhyay, A. Stepanov, B. Schulkin, M. D. Federici, A. Sengupta, D. Gary, J. F. Federici, R. Barat, Z.-H. Michalopoulou, and D. Zimdars, "Terahertz interferometric and synthetic aperture imaging," *J. Opt. Soc. Am. A*, vol. 23, no. 5, pp. 1168–1178, 2006.

[20] S. Hunsche, M. Koch, I. Brener, and M. C. Nuss, "THz near-field imaging," *Optics Communications*, vol. 150, no. 1-6, pp. 22 – 26, 1998.

[21] N. C. J. van der Valk and P. C. M. Planken, "Electro-optic detection of subwavelength terahertz spot sizes in the near field of a metal tip," *Applied Physics Letters*, vol. 81, no. 9, pp. 1558–1560, 2002.

[22] W. L. Chan, J. Deibel, and D. M. Mittleman, "Imaging with terahertz radiation," *REPORTS ON PROGRESS IN PHYSICS*, vol. 70, pp. 1325–1379, AUG 2007.

[23] J. V. Rudd, D. A. Zimdars, and M. W. Warmuth, "Compact fiber-pigtailed terahertz imaging system," vol. 3934, pp. 27–35, SPIE, 2000.

[24] B. Sartorius, H. Roehle, H. Künzel, J. Böttcher, M. Schlak, D. Stanze, H. Venghaus, and M. Schell, "All-fiber terahertz time-domain spectrometer operating at 1.5 $\mu$m telecom wavelengths," *Opt. Express*, vol. 16, no. 13, pp. 9565–9570, 2008.

[25] C. Jordens and M. Koch, "Detection of foreign bodies in chocolate with pulsed terahertz spectroscopy," *Optical Engineering*, vol. 47, no. 3, p. 037003, 2008.

[26] N. Karpowicz, H. Zhong, J. Xu, K.-I. Lin, J.-S. Hwang, and X.-C. Zhang, "Comparison between pulsed terahertz time-domain imaging and continuous wave terahertz imaging," *Semiconductor Science and Technology*, vol. 20, no. 7, pp. S293–S299, 2005.

[27] B. Hu and M. Nuss, "Imaging with terahertz waves," *Optics Letter*, vol. 20, pp. 1716–&, AUG 15 1995.

[28] P. Smith, D. Auston, and M. Nuss, "Subpicosecond photoconducting dipole antennas," *Quantum Electronics,* IEEE *Journal of*, vol. 24, pp. 255–260, Feb 1988.

[29] E. R. Brown, F. W. Smith, and K. A. McIntosh, "Coherent millimeter-wave generation by heterodyne conversion in low-temperature-grown GaAs photoconductors," *Journal of Applied Physics*, vol. 73, no. 3, pp. 1480–1484, 1993.

[30] K. A. McIntosh, E. R. Brown, K. B. Nichols, O. B. McMahon, W. F. DiNatale, and T. M. Lyszczarz, "Terahertz photomixing with diode lasers in low-temperature-grown GaAs," *Applied Physics Letters*, vol. 67, no. 26, pp. 3844–3846, 1995.

[31] S. Verghese, K. A. McIntosh, S. Calawa, W. F. Dinatale, E. K. Duerr, and K. A. Molvar, "Generation and detection of coherent terahertz waves using two photomixers," *Applied Physics Letters*, vol. 73, no. 26, pp. 3824–3826, 1998.

[32] T. Kleine-Ostmann, P. Knobloch, M. Koch, S. Hoffmann, M. Breede, M. Hofmann, G. Hein, K. Pierz, M. Sperling, and K. Donhuijsen, "Continuous-wave THz imaging," *Electronics Letters*, vol. 37, pp. 1461–1463, Nov 2001.

[33] K. J. Siebert, H. Quast, R. Leonhardt, T. Löffler, M. Thomson, T. Bauer, H. G. Roskos, and S. Czasch, "Continuous-wave all-optoelectronic terahertz imaging," *Applied Physics Letters*, vol. 80, no. 16, pp. 3003–3005, 2002.

[34] C. Baker, I. Gregory, M. Evans, W. Tribe, E. Linfield, and M. Missous, "All-optoelectronic terahertz system using low-temperature-grown InGaAs photomixers," *Opt. Express*, vol. 13, no. 23, pp. 9639–9644, 2005.

[35] B. Sartorius, M. Schlak, D. Stanze, H. Roehle, H. Künzel, D. Schmidt, H.-G. Bach, R. Kunkel, and M. Schell, "Continuous wave terahertz systems exploiting 1.5 $\mu m$ telecom technologies," *Opt. Express*, vol. 17, no. 17, pp. 15001–15007, 2009.

[36] B. Brown, "THz generation by photomixing in ultrafast photoconductors," *International Journal of High Speed Electronics and Systems*, vol. 13, no. 2, pp. 497 –, 2003.

[37] J. E. Bjarnason, T. L. J. Chan, A. W. M. Lee, E. R. Brown, D. C. Driscoll, M. Hanson, A. C. Gossard, and R. E. Muller, "ErAs:GaAs photomixer with two-decade tunability and 12 mu w peak output power," *Applied Physics Letters*, vol. 85, no. 18, pp. 3983–3985, 2004.

[38] H. Ito, F. Nakajima, T. Furuta, and T. Ishibashi, "Continuous THz-wave generation using antenna-integrated uni-travelling-carrier photodiodes," *Semiconductor Science and Technology*, vol. 20, no. 7, p. S191, 2005.

[39] H. Kogelnik and C. V. Shank, "Coupled-wave theory of distributed feedback lasers," *Journal of Applied Physics*, vol. 43, no. 5, pp. 2327–2335, 1972.

[40] A. Yariv, "Coupled-mode theory for guided-wave optics," *Quantum Electronics, IEEE Journal of*, vol. 9, pp. 919–933, Sep 1973.

[41] G. Ball and W. Morey, "Efficient integrated Nd3+ fiber laser," *Photonics Technology Letters, IEEE*, vol. 3, pp. 1077–1078, Dec 1991.

[42] M. Sejka, P. Varming, J. Hubner, and M. Kristensen, "Distributed feedback Er3+-doped fibre laser," *Electronics Letters*, vol. 31, pp. 1445–1446, Aug 1995.

[43] K. Yla-Jarkko and A. Grudinin, "Performance limitations of high-power DFB fiber lasers," *Photonics Technology Letters,* IEEE, vol. 15, pp. 191–193, Feb. 2003.

[44] A. L. Schawlow and C. H. Townes, "Infrared and optical masers," *Phys. Rev.*, vol. 112, pp. 1940–1949, Dec 1958.

[45] H. Ghafouri-Shiraz, *Distributed feedback laser diodes and optical tunable filters.* Wiley, 2003.

[46] R. Paschotta, J. Nilsson, A. Tropper, and D. Hanna, "Ytterbium-doped fiber amplifiers," *Quantum Electronics, IEEE Journal of*, vol. 33, pp. 1049–1056, Jul 1997.

[47] R. Mears, L. Reekie, I. Jauncey, and D. Payne, "Low-noise erbium-doped fibre amplifier operating at 1.54 $\mu m$," *Electronics Letters*, vol. 23, pp. 1026–1028, 10 1987.

[48] E. Desurvire, J. R. Simpson, and P. C. Becker, "High-gain erbium-doped traveling-wave fiber amplifier," *Opt. Lett.*, vol. 12, no. 11, pp. 888–890, 1987.

[49] R. Paschotta, J. Nilsson, A. Tropper, and D. Hanna, "Ytterbium-doped fiber amplifiers," *Quantum Electronics,* IEEE *Journal of*, vol. 33, pp. 1049–1056, Jul 1997.

[50] T. Okoshi, K. Kikuchi, and A. Nakayama, "Novel method for high resolution measurement of laser output spectrum," *Electronics Letters*, vol. 16, no. 16, pp. 630–631, 1980.

[51] P. Horak and W. H. Loh, "On the delayed self-heterodyne interferometric technique for determining the linewidth of fiber lasers," *Opt. Express*, vol. 14, no. 9, pp. 3923–3928, 2006.

[52] "Data sheet for a DFB fiber laser module from Koheras a/s." `http://www.nktphotonics.com/files/files/datasheet_koheras_basik-module.pdf`.

[53] J. Nilsson, Y. Jeong, C. Codemard, J.-N. Maran, C. Farrell, J. Ji, S. Yoo, J. Sahu, D. Richardson, and D. Payne, "High power fiber sources," in *Conference on Optoelectronics and Optical Communications (COOC) 2008*, (Busan, Korea), May 2008.

[54] G. Agrawal, *Nonlinear fiber optics*. ACADEMIC PRESS, 2001.

[55] R. G. Smith, "Optical power handling capacity of low loss optical fibers as determined by stimulated Raman and Brillouin scattering," *Appl. Opt.*, vol. 11, no. 11, pp. 2489–2494, 1972.

[56] V. I. Kovalev and R. G. Harrison, "Suppression of stimulated brillouin scattering in high-power single-frequency fiber amplifiers," *Opt. Lett.*, vol. 31, no. 2, pp. 161–163, 2006.

[57] K. Kawase, M. Mizuno, S. Sohma, H. Takahashi, T. Taniuchi, Y. Urata, S. Wada, H. Tashiro, and H. Ito, "Difference-frequency terahertz-wave generation from 4-dimethylamino-N-methyl-4-stilbazolium-tosylate by use of an electronically tuned Ti:sapphire laser.," *Opt. Lett.*, vol. 24, no. 15, pp. 1065–1067, 1999.

[58] M. Walther, K. Jensby, S. R. Keiding, H. Takahashi, and H. Ito, "Far-infrared properties of DAST," *Opt. Lett.*, vol. 25, no. 12, pp. 911–913, 2000.

[59] B. Pradarutti, G. Matthäus, S. Riehemann, G. Notni, S. Nolte, and A. Tünnermann, "Highly efficient terahertz electro-optic sampling by material optimization at 1060 nm," *Optics Communications*, vol. 281, no. 19, pp. 5031 – 5035, 2008.

[60] A. Schneider, M. Stillhart, and P. Günter, "High efficiency generation and detection of terahertz pulses using laser pulses at telecommunication wavelengths," *Opt. Express*, vol. 14, no. 12, pp. 5376–5384, 2006.

[61] H.-G. Bach, A. Beling, G. Mekonnen, R. Kunkel, D. Schmidt, W. Ebert, A. Seeger, M. Stollberg, and W. Schlaak, "InP-based waveguide-integrated photodetector with 100-GHz bandwidth," *Selected Topics in Quantum Electronics, IEEE Journal of*, vol. 10, pp. 668–672, July-Aug. 2004.

[62] D. H. Auston, "Picosecond optoelectronic switching and gating in silicon," *Applied Physics Letters*, vol. 26, pp. 101–103, 1975.

[63] D. H. Auston, K. P. Cheung, and P. R. Smith, "Picosecond photoconducting hertzian dipoles," *Applied Physics Letters*, vol. 45, pp. 284–286, 1984.

[64] D. H. Auston, K. P. Cheung, J. A. Valdmanis, and D. A. Kleinman, "Cherenkov radiation from femtosecond optical pulses in electro-optic media," *Physical Review Letters*, vol. 53, pp. 1555–1558, 1984.

[65] P. R. Smith, D. H. Auston, and M. C. Nuss, "Subpicosecond photoconducting dipole antennas," *Ieee Journal of Quantum Electronics*, vol. 24, pp. 255–260, 1988.

[66] C. Fattinger and D. Grischkowsky, "Point-source terahertz optics," *Applied Physics Letters*, vol. 53, pp. 1480–1482, 1988.

[67] C. Fattinger and D. Grischkowsky, "Terahertz beams," *Applied Physics Letters*, vol. 54, pp. 490–492, 1989.

[68] M. van Exter, C. Fattinger, and D. Grischkowsky, "High-brightness terahertz beams characterized with an ultrafast detector," *Applied Physics Letters*, vol. 55, no. 4, pp. 337–339, 1989.

[69] P. U. Jepsen, R. H. Jacobsen, and S. R. Keiding, "Generation and detection of terahertz pulses from biased semiconductor antennas," *J. Opt. Soc. Am. B*, vol. 13, no. 11, pp. 2424–2436, 1996.

[70] J. E. Pedersen, V. G. Lyssenko, J. M. Hvam, P. U. Jepsen, S. R. Keiding, C. B. S. rensen, and P. E. Lindelof, "Ultrafast local field dynamics in photoconductive THz antennas," *Applied Physics Letters*, vol. 62, no. 11, pp. 1265–1267, 1993.

[71] D. Grischkowsky, S. Keiding, M. van Exter, and C. Fattinger, "Far-infrared time-domain spectroscopy with terahertz beams of dielectrics and semiconductors," *J. Opt. Soc. Am. B*, vol. 7, no. 10, pp. 2006–2015, 1990.

[72] J. Shan, A. Nahata, and T. Heinz, "Terahertz time-domain spectroscopy based on nonlinear optics," *Journal of Nonlinear Optical Physics and Materials*, vol. 11, no. 1, pp. 31–48, 2002.

[73] M. C. Beard, G. M. Turner, and C. A. Schmuttenmaer, "Subpicosecond carrier dynamics in low-temperature grown GaAs as measured by time-resolved terahertz spectroscopy," *Journal of Applied Physics*, vol. 90, pp. 5915–5923, 2001.

[74] F. E. Doany, D. Grischkowsky, and C. C. Chi, "Carrier lifetime versus ion-implantation dose in silicon on sapphire," *Applied Physics Letters*, vol. 50, pp. 460–462, 1987.

[75] Q. Wu, M. Litz, and X. C. Zhang, "Broadband detection capability of ZnTe electro-optic field detectors," *Applied Physics Letters*, vol. 68, pp. 2924–2926, 1996.

[76] P. U. Jepsen, C. Winnewisser, M. Schall, V. Schyja, S. R. Keiding, and H. Helm, "Detection of THz pulses by phase retardation in lithium tantalate," *Physical Review E*, vol. 53, pp. R3052–R3054, 1996.

[77] A. Nahata, D. H. Auston, T. F. Heinz, and C. J. Wu, "Coherent detection of freely propagating terahertz radiation by electro-optic sampling," *Applied Physics Letters*, vol. 68, pp. 150–152, 1996.

[78] G. Gallot, J. Q. Zhang, R. W. McGowan, T. I. Jeon, and D. Grischkowsky, "Measurements of the THz absorption and dispersion of ZnTe and their relevance to the electro-optic detection of THz radiation," *Applied Physics Letters*, vol. 74, pp. 3450–3452, 1999.

[79] P. C. M. Planken, H. K. Nienhuys, H. J. Bakker, and T. Wenckebach, "Measurement and calculation of the orientation dependence of terahertz pulse detection in ZnTe," *Journal of the Optical Society of America B-Optical Physics*, vol. 18, pp. 313–317, 2001.

[80] M. van Exter, C. Fattinger, and D. Grischkowsky, "Terahertz time-domain spectroscopy of water vapor," *Opt. Lett.*, vol. 14, no. 20, pp. 1128–1130, 1989.

[81] P. N. Butcher and D. Cotter, *The Elements of Nonlinear Optics*. Cambridge University Press, 1990.

[82] D. Mittleman, R. Jacobsen, and M. Nuss, "T-ray imaging," *Selected Topics in Quantum Electronics,* IEEE *Journal of*, vol. 2, pp. 679–692, Sep 1996.

[83] C. Janke, M. Forst, M. Nagel, H. Kurz, and A. Bartels, "Asynchronous optical sampling for high-speed characterization of integrated resonant terahertz sensors," *Opt. Lett.*, vol. 30, no. 11, pp. 1405–1407, 2005.

[84] T. Yasui, E. Saneyoshi, and T. Araki, "Asynchronous optical sampling terahertz time-domain spectroscopy for ultrahigh spectral resolution and rapid data acquisition," *Applied Physics Letters*, vol. 87, no. 6, p. 061101, 2005.

[85] D. Mittleman, M. Gupta, R. Neelamani, R. Baraniuk, J. Rudd, and M. Koch, "Recent advances in terahertz imaging," *Appl. Phys. B*, vol. 68, p. 1085, 1999.

[86] D. M. Mittleman, S. Hunsche, L. Boivin, and M. C. Nuss, "T-ray tomography," *Opt. Lett.*, vol. 22, no. 12, pp. 904–906, 1997.

[87] H. Zhong, J. Xu, X. Xie, T. Yuan, R. Reightler, E. Madaras, and X.-C. Zhang, "Nondestructive defect identification with terahertz time-of-flight tomography," *Sensors Journal,* IEEE, vol. 5, pp. 203–208, April 2005.

[88] I. Maeng, C. Kang, S. J. Oh, J.-H. Son, K. H. An, and Y. H. Lee, "Terahertz electrical and optical characteristics of double-walled carbon nanotubes and their comparison with single-walled carbon nanotubes," *Applied Physics Letters*, vol. 90, no. 5, p. 051914, 2007.

[89] T.-I. Jeon, K.-J. Kim, C. Kang, S.-J. Oh, J.-H. Son, K. H. An, D. J. Bae, and Y. H. Lee, "Terahertz conductivity of anisotropic single walled carbon nanotube films," *Applied Physics Letters*, vol. 80, no. 18, pp. 3403–3405, 2002.

[90] H. Altan, F. Huang, J. F. Federici, A. Lan, and H. Grebel, "Optical and electronic characteristics of single walled carbon nanotubes and silicon nanoclusters by tetrahertz spectroscopy," *Journal of Applied Physics*, vol. 96, no. 11, pp. 6685–6689, 2004.

[91] K. Koziol, J. Vilatela, A. Moisala, M. Motta, P. Cunniff, M. Sennett, and A. Windle, "High-Performance Carbon Nanotube Fiber," *Science*, vol. 318, no. 5858, pp. 1892–1895, 2007.

[92] C. Ducati, K. Koziol, S. Friedrichs, T. Yates, , P. Midgley, and A. Windle, "Crystallographic order in multi-walled carbon nanotubes synthesized in the presence of nitrogen," *Small*, vol. 2, no. 6, pp. 774–784, 2006.

[93] L. Ren, C. L. Pint, L. G. Booshehri, W. D. Rice, X. Wang, D. J. Hilton, K. Takeya, I. Kawayama, M. Tonouchi, R. H. Hauge, and J. Kono, "Carbon nanotube terahertz polarizer," *Nano Letters*, vol. 9, no. 2610-2613, 2009.

[94] T.-I. Jeon, K.-J. Kim, C. Kang, I. H. Maeng, J.-H. Son, K. H. An, J. Y. Lee, and Y. H. Lee, "Optical and electrical properties of preferentially anisotropic single-walled carbon-nanotube films in terahertz region," *Journal of Applied Physics*, vol. 95, no. 10, pp. 5736–5740, 2004.

[95] T.-I. Jeon, K.-J. Kim, C. Kang, S.-J. Oh, J.-H. Son, K. H. An, D. J. Bae, and Y. H. Lee, "Characterization of singlewalled carbon nanotube films by terahertz spectroscopy," *Synthetic Metals*, vol. 135-136, pp. 429 – 430, 2003. Proceedings of the International Conference on Science and Technology of Synthetic Metals.

[96] T.-I. Jeon, J.-H. Son, K. H. An, Y. H. Lee, and Y. S. Lee, "Terahertz absorption and dispersion of fluorine-doped single-walled carbon nanotube," *Journal of Applied Physics*, vol. 98, no. 3, p. 034316, 2005.

[97] T.-I. Jeon, K.-J. Kim, C. Kang, S.-J. Oh, J.-H. Son, K. H. An, D. J. Bae, and Y. H. Lee, "Terahertz conductivity of anisotropic single walled carbon nanotube films," *Applied Physics Letters*, vol. 80, no. 18, pp. 3403–3405, 2002.

[98] C. Kang, I. H. Maeng, S. J. Oh, J.-H. Son, T.-I. Jeon, K. H. An, S. C. Lim, and Y. H. Lee, "Frequency-dependent optical constants and conductivities of hydrogen-functionalized single-walled carbon nanotubes," *Applied Physics Letters*, vol. 87, no. 4, p. 041908, 2005.

[99] Z. Wu, L. Wang, Y. Peng, A. Young, S. Seraphin, and H. Xin, "Terahertz characterization of multi-walled carbon nanotube films," *Journal of Applied Physics*, vol. 103, no. 9, p. 094324, 2008.

[100] Z. H. Zhong, N. M. Gabor, J. E. Sharping, A. L. Gaeta, and P. L. McEuen, "Terahertz time-domain measurement of ballistic electron resonance in a single-walled carbon nanotube," *Nature Nanotechnology*, vol. 3, pp. 201–205, 2008.

[101] P. Parkinson, J. Lloyd-Hughes, Q. Gao, H. H. Tan, C. Jagadish, M. B. Johnston, and L. M. Herz, "Transient terahertz conductivity of GaAs nanowires," *Nano Letters*, vol. 7, no. 7, pp. 2162–2165, 2007.

[102] M. C. Beard, G. M. Turner, and C. A. Schmuttenmaer, "Size-dependent photoconductivity in cdse nanoparticles as measured by time-resolved terahertz spectroscopy," *Nano Letters*, vol. 2, no. 9, pp. 983–987, 2002.

[103] E. Hendry, M. Koeberg, B. O'Regan, and M. Bonn, "Local field effects on electron transport in nanostructured TiO2 revealed by terahertz spectroscopy," *Nano Letters*, vol. 6, no. 4, pp. 755–759, 2006.

[104] K. Koziol, M. Shaffer, and A. Windle, "Three-dimensional internal order in multiwalled carbon nanotubes grown by chemical vapor deposition," *Advanced Materials*, vol. 17, no. 6, pp. 760–763, 2005.

[105] Y. Dikmelik, J. B. Spicer, M. J. Fitch, and R. Osiander, "Effects of surface roughness on reflection spectra obtained by terahertz time-domain spectroscopy," *Opt. Lett.*, vol. 31, no. 24, pp. 3653–3655, 2006.

[106] M. Ortolani, J. S. Lee, U. Schade, and H.-W. Hübers, "Surface roughness effects on the terahertz reflectance of pure explosive materials," *Applied Physics Letters*, vol. 93, no. 8, p. 081906, 2008.

[107] R. Piesiewicz, C. Jansen, D. Mittleman, T. Kleine-Ostmann, M. Koch, and T. Kurner, "Scattering analysis for the modeling of thz

communication systems," *Antennas and Propagation,* IEEE *Transactions on*, vol. 55, pp. 3002–3009, Nov. 2007.

[108] Z. Jian and D. M. Mittleman, "Broadband group-velocity anomaly in transmission through a terahertz photonic crystal slab," *Physical Review B (Condensed Matter and Materials Physics)*, vol. 73, no. 11, p. 115118, 2006.

[109] J. R. Fletcher, G. P. Swift, D. C. Dai, J. A. Levitt, and J. M. Chamberlain, "Propagation of terahertz radiation through random structures: An alternative theoretical approach and experimental validation," *Journal of Applied Physics*, vol. 101, no. 1, p. 013102, 2007.

[110] K. J. Chau and A. Y. Elezzabi, "Terahertz transmission through ensembles of subwavelength-size metallic particles," *Phys. Rev. B*, vol. 72, p. 075110, Aug 2005.

[111] J. Pearce, K. Doyle, Z. Jian, J. Deibel, and D. M. Mittleman, "Nonstationary time-domain statistics of multiply scattered broadband terahertz pulses," *J. Opt. Soc. Am. B*, vol. 23, no. 8, pp. 1506–1510, 2006.

[112] J. Pearce, Z. Jian, and D. M. Mittleman, "Propagation of terahertz pulses in random media," *Philosophical Transactions: Mathematical, Physical and Engineering Sciences*, vol. 362, no. 1815, pp. 301–314, 2004.

[113] P.-E. Wolf and G. Maret, "Weak localization and coherent backscattering of photons in disordered media," *Phys. Rev. Lett.*, vol. 55, pp. 2696–2699, Dec 1985.

[114] E. Akkermans, P. E. Wolf, and R. Maynard, "Coherent backscattering of light by disordered media: Analysis of the peak line shape," *Phys. Rev. Lett.*, vol. 56, pp. 1471–1474, Apr 1986.

[115] A. R. McGurn and A. A. Maradudin, "Weak transverse localization of light scattered incoherently from a one-dimensional random metal surface," *J. Opt. Soc. Am. B*, vol. 10, no. 3, pp. 539–545, 1993.

[116] U. of Maryland, "SSPROP MatLab source code." Can be downloaded on: `http:\\www.photonics.umd.edu\software\ssprop\`.

[117] D. Kane and R. Trebino, "Characterization of arbitrary femtosecond pulses using frequency-resolved optical gating," *Quantum Electronics, IEEE Journal of*, vol. 29, pp. 571–579, Feb 1993.

[118] R. Trebino, K. W. DeLong, D. N. Fittinghoff, J. N. Sweetser, M. A. Krumbugel, B. A. Richman, and D. J. Kane, "Measuring ultrashort laser pulses in the time-frequency domain using frequency-resolved optical gating," *Review of Scientific Instruments*, vol. 68, no. 9, pp. 3277–3295, 1997.

[119] R. Trebino, *Frequency-Resolved Optical Gating: The Measurement of Ultrashort Laser Pulses*. Kluwer, 2002.

[120] L. G. Nielsen and Y. Qian, *Dispersion-compensating Fibers for Raman applications*, vol. 90 of *Springer Series in Optical Sciences*, ch. 6. Springer, 2004.

[121] P. U. Jepsen and S. R. Keiding, "Radiation patterns from lens-coupled terahertz antennas," *Opt. Lett.*, vol. 20, no. 8, pp. 807–809, 1995.

# Appendix A

# List of Publications

The author contributed the following publications:

**Journal publications**

1. Viktor Krozer, Torsten Löffler, Peter Uhd Jepsen, Finn Eichhorn, Rasmus K. Olsson, Jonas D. Buron, Jørgen Dall, Anders Kusk, Vitaliy Zhurbenko, Thomas Jensen, "*THz Imaging Systems with Aperture Synthesis Techniques*", submitted to MICROWAVE THEORY AND TECHNIQUES, IEEE Transactions on, Special Issue: THz Technology: Bridging the Microwave-to-Photonics Gap, to be published in 2010. (**invited Review**).

2. Finn Eichhorn, Rasmus K. Olsson,Jonas D. Buron, Lars Grüner-Nielsen,Jens E. Pedersen, and Peter U. Jepsen, "*Optical fiber link for transmission of 1-nJ femtosecond laser pulses at 1550 nm*". **Submitted Optics Express**.

3. Finn Eichhorn, Peter U. Jepsen, Krzysztof K. K. Koziol, Nicholas Schroeder, Satya R. Ganti, Gregory Kozlowski, and Jason A. Deibel, "*The Scattering of Terahertz Radiation from Oriented Carbon Nanotube Films*". IEEE Trans. Nanotech. **Close to submission**.

**Conference contributions**

4. Finn Eichhorn, Peter U. Jepsen, Nicholas Schroeder, Gregory Kozlowski, Jason A. Deibel, and Krzysztof K.K. Koziol, "*Scattering of Terahertz Radiation from Oriented Carbon Nanotube Films*", CLEO/IQEC Conference on Lasers and Electro-Optics and the International Quantum Electronics Conference. Baltimore, USA, (2009) (**talk**).

5. Finn Eichhorn, Rasmus K. Olsson, Jonas D. Buron, and Peter U. Jepsen, "*Low dispersion fiber link for distribution of femtosecond pulses to photonicly-driven terahertz emitter and detector units*", 1st Nordic Meeting in Physics, Danish Physical Society (DFS), Kongens Lyngby, Denmark (2009), (**talk**)

6. Viktor Krozer, Torsten Löffler, Peter U. Jepsen, Jørgen Dall, Vitaliy Zhurbenko, Finn Eichhorn, and Anders Kusk, "*Terahertz Camera for Remote Detection of Material Defects and Biological and Chemical Substances: Design Study*", 5th ESA Workshop on Millimetre Wave Technology and Applications & 31st ESA Antenna Workshop. Noordwijk, The Netherlands, (2009) (**talk**).

7. Finn Eichhorn, Peter U. Jepsen, Nicholas Schroeder, Gregory Kozlowski, Jason Deibel, and Krzysztof K.K. Koziol, "*Investigation of Scattering and Doping in Carbon Nanotubes with THz Time-Domain Spectroscopy*", Optical Terahertz Science and Technology 2009 Meeting. Santa Brabara, California, (2009) (**talk**).

8. Nicholas Schroeder, Finn Eichhorn, and Jason Deibel, "*Combustion Diagnostics with Terahertz Tomography*", Joint Meeting of the APS Ohio-Region Section, the AAPT Southern Ohio Section, and the ACS Dayton-Section. Dayton, Ohio, USA, (2008) (**talk**).

9. Finn Eichhorn, Jens E. Pedersen, and Peter U. Jepsen, "*Power-scalable, polarization-stable, dual-colour DFB fibre laser system for CW terahertz imaging*", Joint Meeting of the APS Ohio-Region Section, the AAPT

Southern Ohio Section, and the ACS Dayton-Section. Dayton, Ohio, USA, (2008). (**poster**)

10. Finn Eichhorn, Jens E. Pedersen, and Peter U. Jepsen, "*Polarization-stable dual-colour DFB fibre laser system for CW terahertz generation*", European Optical Society Annual Meeting. Paris-Nord Villepinte, Parc d'expositions et Centre de Convention, (2008) (**poster**).

11. Uffe Møller, Jens Kristian Jensen, Finn Eichhorn, Jacob Riis Folkenberg, and Peter Uhd Jepsen, "*Determination of alcohol concentration in plastic bottles with THz reflection spectroscopy*", FoodDTU Conference, Technical University of Denmark, Kgs. Lyngby, Denmark (2008) (**poster**).

12. Finn Eichhorn, Jens Engholm Pedersen, and Peter U. Jepsen, "P*olarization-stable dual-color DFB fibre laser system for CW terahertz generation*" Danish Physical Society Annual Meeting, Nyborg, Denmark (2008) (**poster**).

13. Peter Uhd Jepsen, Uffe Møller, Finn Eichhorn, Hannes Merbold, Jacob Riis Folkenberg, and Steward Clark, "*Terahertz Time-domain Spectroscopy of Crystalline and Aqueous Systems*", CLEO/QELS, Baltimore, Maryland, USA (2007) (**invited talk**).

14. Peter Uhd Jepsen, Uffe Møller, Finn Eichhorn, Hannes Merbold, Jacob Riis Folkenberg, and Steward Clark, "*Terahertz Time-domain Spectroscopy and Modelling of Crystalline and Aqueous Systems*", Presented at: Royal Netherlands Academy of Arts and Sciences: Colloquium on Terahertz Science, Amsterdam, The Netherlands (2007) (**invited talk**).

15. Finn Eichhorn, Uffe Møller, Jens E. Pedersen, Claus F. Pedersen, and Peter Uhd Jepsen, "*Tunable Dual-wavelength DFB Fibre Laser System for kHz-linewidth Terahertz Generation by Photo-mixing*", Danish Physical Society Annual Meeting, Nyborg, Denmark (2007) (**poster**).

16. Finn Eichhorn, Jens E. Pedersen, Claus F. Pedersen, and Peter Uhd Jepsen, "*Dual-color, power-scalable DFB fibre laser system for kHz-*

*linewidth terahertz generation*", Optical Terahertz Science and Technology Topical Meeting. Orlando, Florida, USA, (2007) (**post-deadline talk**)

**Book chapters**

17. David Cooke, Dmitry Turchinovich, Uffe Møller, Finn Eichhorn, and Peter Uhd Jepsen, "*Nyt lys på ukendt land: Terahertz teknologi*", Chapter 4 in: "*Optiske Horisonter: en rejse på kommunikationsteknologiens vinger*", pp. 67-91, one2one, Odense, COM DTU, Denmark (2007) (**Danish high school book**).